TOPICS IN COLLIDER PHYSICS

A DISSERTATION
SUBMITTED TO THE DEPARTMENT OF PHYSICS
AND THE COMMITTEE ON GRADUATE STUDIES
OF STANFORD UNIVERSITY
IN PARTIAL FULFILLMENT OF THE REQUIREMENTS
FOR THE DEGREE OF
DOCTOR OF PHILOSOPHY

Francis John Petriello
August 2003
SLAC-R-644
Work supported in part by U.S. Department of Energy contract
DE-AC03-76SF00515

I certify that I have read this dissertation and that, in my opinion, it is fully adequate in scope and quality as a dissertation for the degree of Doctor of Philosophy.

JoAnne Hewett
(Principal Adviser)

I certify that I have read this dissertation and that, in my opinion, it is fully adequate in scope and quality as a dissertation for the degree of Doctor of Philosophy.

Lance Dixon

I certify that I have read this dissertation and that, in my opinion, it is fully adequate in scope and quality as a dissertation for the degree of Doctor of Philosophy.

Michael Peskin

Approved for the University Committee on Graduate Studies.

Abstract

It is an exciting time for high energy physics. Several experiments are currently exploring uncharted terrain; the next generation of colliders will begin operation in the coming decade. These experiments will together help us understand some of the most puzzling issues in particle physics: the mechanism of electroweak symmetry breaking and the generation of flavor physics. It is clear that the primary goal of theoretical particle physics in the near future is to support and guide this experimental program. These tasks can be accomplished in two ways: by developing experimental signatures for new models which address outstanding problems, and by improving Standard Model predictions for precision observables. We present here several results which advance both of these goals.

We begin with a study of non-commutative field theories. It has been suggested that TeV-scale non-commutativity could explain the origin of CP violation in the SM. We identify several distinct signatures of non-commutativity in high energy processes. We also demonstrate the one-loop quantum consistency of a simple spontaneously broken non-commutative U(1) theory; this result is an important preface to any attempt to embed the SM within a non-commutative framework.

We then investigate the phenomenology of extra-dimensional theories, which have been suggested recently as solutions to the hierarchy problem of particle physics. We first examine the implications of allowing SM fields to propagate in the full five-dimensional spacetime of the Randall-Sundrum model, which solves the hierarchy problem via an exponential "warping" of the Planck scale induced by a five-dimensional anti de-Sitter geometry. In an alternative exra-dimensional theory, in which all SM fields are permitted to propagate in flat extra dimensions, we show that properties of the Higgs boson are significantly modified.

Finally, we discuss the next-to-next-to leading order QCD corrections to the dilepton rapidity distribution in the Drell-Yan process, an important discovery channel for new physics at hadron colliders. We introduce a powerful new method for calculating differential distributions in hard scattering processes. We apply our results to the analysis of fixed target experiments, which provide important constraints on the parton distribution functions of the proton.

Acknowledgements

I thank my advisor, JoAnne Hewett, for her help and especially her patience during my time at SLAC.

I thank Hooman Davoudiasl, Lance Dixon, Michael Peskin, Darius Sadri, and the remaining students, postdocs, and professors at SLAC for sharing their knowledge of particle physics with me.

Most importantly, I acknowledge my great indebtedness to Babis Anastasiou, Kirill Melnikov, and Tom Rizzo, for their willingness to answer my endless stream of naive questions, for teaching me the proper way of looking at both high energy physics and physicists, and for their friendship. Without them the past four years would have been a much less enjoyable experience.

Finally, I thank my family for putting up with me before, during, and hopefully after the completion of this thesis.

Chapters 2-5 of this thesis are based upon material that has appeared previously in the following publications:

- J. L. Hewett, F. J. Petriello and T. G. Rizzo, "Signals for non-commutative interactions at linear colliders," Phys. Rev. D **64**, 075012 (2001);
- F. J. Petriello, "The Higgs mechanism in non-commutative gauge theories," Nucl. Phys. B **601**, 169 (2001);
- J. L. Hewett, F. J. Petriello and T. G. Rizzo, "Precision measurements and fermion geography in the Randall-Sundrum model revisited," JHEP **0209**, 030 (2002);
- F. J. Petriello, "Kaluza-Klein effects on Higgs physics in universal extra dimensions," JHEP **0205**, 003 (2002).

These have been reprinted with the permission of the respective publishers. The work in Chapter 6 is based upon the preprint "Dilepton rapidity distribution in the Drell-Yan process at NNLO in QCD," to appear, written in collaboration with Charalampos Anastasiou, Lance Dixon, and Kirill Melnikov.

Contents

List of Tables

List of Figures

Chapter 1

Introduction

It is an exciting time for high energy physics. Several experiments are currently exploring previously uncharted terrain. BABAR and BELLE are acquiring an unprecedented amount of data studying CP violation in the B meson system, while the Tevatron is providing our first glimpse of TeV-scale physics. In the coming decade, the Large Hadron Collider (LHC) at CERN will start taking data, and construction of a high energy e^+e^- linear collider will hopefully begin. These experiments will together help us understand some of the most puzzling issues in particle physics: the mechanism of electroweak symmetry breaking, the origin of CP violation, and the generation of flavor physics and the fermion mass hierarchy.

With such great advances expected in experimental particle physics, it is clear that the primary goal of theoretical particle physics in the near future is to guide this program. This guidance can take two forms: the development of experimental signatures for new models which address outstanding problems in particle physics, and the improvement of the Standard Model (SM) predictions for precision observables. Both of these efforts are vital to the success of the experimental program. We present here results which advance both of these goals.

A promising candidate for the "theory of everything" is string theory; it is therefore important to determine its physical predictions. Although far from complete and incapable of making precise statements, string theory provides qualitative guidance regarding how physics might be modified at short distances. We explore in

Chapters 2 and 3 the experimental implications of formulating field theories in non-commutative (NC) geometries, which appear naturally in compactifications of string theory in the presence of background gauge fields [57, 76, 156]. It has been suggested that TeV-scale non-commutativity could explain the origin of CP violation in the SM [107, 159]. We study in Chapter 2 the phenomenology of NC theories, and show that they lead to distinct signatures in high energy processes. In Chapter 3 we demonstrate the one-loop quantum consistency of a simple spontaneously broken NC U(1) theory; this result is an important preface to any attempt to embed the SM within a NC framework [27, 39, 44, 45], and has been useful in other investigations of the structure of NC theories [122, 153, 154].

The most vexing puzzle in high energy physics today is the origin of electroweak (EW) symmetry breaking. The simple mechanism utilized in the SM, where a single scalar Higgs boson acquires a TeV-scale vacuum expectation value, is almost certainly incomplete. Quantum corrections tend to push the Higgs boson mass to the Planck scale; although not yet discovered, fits to the precision Z-pole data obtained in the LEP and SLC experiments indicate that a Higgs boson with a mass $m_H <$ 200 GeV is indeed present in nature [1]. In the past few years a new solution to this "hierarchy problem" has been suggested. This novel approach postulates the existence of extra spacetime dimensions in which gravity propagates [13, 22, 146, 147]. We study in Chapters 4 and 5 several phenomenological aspects of this class of theories. In Chapter 4, we examine the implications of allowing SM fields to propagate in the full five-dimensional spacetime of the Randall-Sundrum model [146, 147]; this is a particularly attractive theory which solves the hierarchy problem via an exponential "warping" of the Planck scale induced by a five-dimensional anti de-Sitter geometry. We demonstrate that the observed m_c/m_t and m_s/m_b mass hierarchies can be naturally reproduced in this model. We also show that this scenario permits a Higgs boson with a mass of 500 GeV in a fit to the precision EW data, and remains otherwise invisible at the LHC; the entire parameter space is testable only at future e^+e^- linear colliders. In an alternative extra-dimensional theory, known as the universal extra dimensions model [15], all SM fields are permitted to propagate in flat, TeV^{-1} extra dimensions for various model-building purposes [17, 18]. We show in Chapter 5 that this scenario significantly modifies properties of the Higgs boson which will be measured at future colliders; deviations from Standard Model predictions as large as $\approx 85\%$ occur for typical parameter choices.

Many searches for new physics, including those described above, rely upon observing deviations from SM predictions for lepton pair production in the Drell-Yan process [77]. This process is also important for several other reasons: (i) it is used in global analyses of scattering data used to fit the parton distribution functions of the proton [120, 126, 127]; (ii) it is one of the processes through which the W mass, needed in fits to the precision Z-pole data, is measured (see [31] for a review); (iii) it will be used as a partonic luminosity monitor at the LHC [73]. These applications require that the differential distributions of the produced lepton pair, and not only its inclusive production rate, are known to high precision. We present in Chapter 6 a calculation of the next-to-next-to leading order QCD corrections to the Drell-Yan rapidity distribution; a computation to this order in perturbation theory is needed for percent level predictions. We apply our results to the analysis of low-energy fixed target experiments, which are used in the extraction of parton distribution functions [162, 165].

In Chapter 7 we summarize the results obtained in this thesis, and present our conclusions.

Chapter 2

Experimental Signatures for Non-commutative Interactions at Linear Colliders

2.1 Introduction and Background

Although the full details of string/M-theory have yet to be unraveled, this theoretical effort has inspired a number of ideas over the years which have had significant impact on the phenomenology of particle physics. Two such examples are given by the string-inspired E_6 models of the late 1980's [106] and the ongoing endeavor in building realistic and testable models from theories which have additional space-time dimensions [12, 13, 22, 23, 124, 146, 147, 166]. Most recently, a resurgence of interest in non-commutative quantum field theory (NCQFT) and its applications [89, 91, 123, 137] has developed within the context of string theory. Of course non-commutative theories are also interesting in their own right. However, it has yet to be explored whether they have any connection with the physics of the Standard Model (SM) or whether their effects could be observable in laboratory experiments. In this chapter we begin to address these questions by examining the implications of non-commutativity for future collider experiments.

An exhaustive introduction to NCQFT is beyond the scope of the present treatment, hence we will simply outline some of the basics of the theory as well as some results which are relevant to the phenomenological analysis that follows. We will see that NCQFT results in modifications to QED which can be probed in $2 \to 2$ processes in e^+e^- collisions.

The essential idea of NCQFT is a generalization of the usual d-dimensional space, R^d, associated with commuting space-time coordinates to one which does not commute, R^d_θ. In such a space the conventional coordinates are represented by operators which no longer commute, *i.e.*,

$$[\hat{X}_\mu, \hat{X}_\nu] = i\theta_{\mu\nu} \equiv \frac{i}{\Lambda^2_{NC}} c_{\mu\nu} \, . \tag{2.1}$$

In the last equality we have parameterized the effect in terms of an overall scale Λ_{NC}, which characterizes the threshold where non-commutative (NC) effects become relevant, and a real antisymmetric matrix $c_{\mu\nu}$, whose dimensionless elements are presumably of order unity. From our point of view the role of the NC scale Λ_{NC} can be compared to that of $\hbar$ in conventional Quantum Mechanics which represents the level of non-commutativity between coordinates and momenta. *A priori* the scale Λ_{NC} can take any value, perhaps the most likely being of order the Planck scale $\overline{M}_{Pl}$. However, given the possibility of the onset of stringy effects at the TeV scale, and that values of the scale where gravity becomes strong in models with large extra dimensions can be of order a TeV, it is feasible that NC effects could also set in at a TeV. Here, we adopt this spirit and consider the possibility that Λ_{NC} may not lie far above the TeV scale.

Note that the matrix $c_{\mu\nu}$ is *not* a tensor since its elements are identical in all reference frames. This leads immediately to a violation of Lorentz invariance which is quite different than that discussed most often in the literature [54, 113, 114, 115, 116, 117, 118] since it sets in only at energies of order Λ_{NC}. As we will see below, this violation will take the form of dimension-8 operators for the processes we consider and is thus highly suppressed at low energies. In addition, there exists a more than superficial relation between the anti-symmetric matrix $c_{\mu\nu}$ and the Maxwell field strength tensor $F_{\mu\nu}$ as NCQFT arises in string theory [33, 57, 76, 92, 155, 156, 157] through the quantization of strings, described by the low energy excitations of D-branes in the presence of background electromagnetic fields. The space-time components, c_{0i}, thus define the direction of a background **E** field, while the space-space components, c_{ij}, describe the direction of a background magnetic or string **B** field. Geometrically, we can then think of c_{0i} and c_{ij} as two 3-vectors that point in a specific pair of preferred directions in the laboratory frame. Theories with $c_{0i}(c_{ij}) \neq 0$ are usually referred to as space-time(space-space) non-commutative.

NCQFT can be phrased in terms of conventional commuting QFT through the application of the Weyl-Moyal correspondence [148]

$$\hat{A}(\hat{X}) \longleftrightarrow A(x)\,, \tag{2.2}$$

where A represents a quantum field with $\hat{X}$ being the set of non-commuting coordinates and x corresponding to the commuting set. However, in formulating NCQFT, one must be careful to preserve orderings in expressions such as $\hat{A}(\hat{X})\hat{B}(\hat{X})$. This is accomplished with the introduction of a star product, $\hat{A}(\hat{X})\hat{B}(\hat{X}) = A(x) * B(x)$, where the effect of the commutation relation is absorbed into the star. Making the Fourier transform pair

$$\begin{aligned} \hat{A}(\hat{X}) &= \frac{1}{(2\pi)^{d/2}} \int d\alpha e^{i\alpha\hat{X}}\; a(\alpha) \\ a(\alpha) &= \frac{1}{(2\pi)^{d/2}} \int dx e^{-i\alpha x}\; A(x)\,, \end{aligned} \tag{2.3}$$

with x and α being real n-dimensional variables, allows us to write the product of two fields as

$$\begin{aligned} \hat{A}(\hat{X})\hat{B}(\hat{X}) &= \frac{1}{(2\pi)^{d}} \int d\alpha d\beta e^{i\alpha\hat{X}}\; a(\alpha) e^{i\beta\hat{X}}\; b(\beta) \\ &= \frac{1}{(2\pi)^{d}} \int d\alpha d\beta\; e^{i(\alpha+\beta)\hat{X} - \frac{1}{2}\alpha^{\mu}\beta^{\nu}[\hat{X}_{\mu},\hat{X}_{\nu}]} a(\alpha) b(\beta)\,. \end{aligned} \tag{2.4}$$

We thus have the correspondence

$$\hat{A}(\hat{X})\hat{B}(\hat{X}) \longleftrightarrow A(x) * B(x)\,, \tag{2.5}$$

provided we identify

$$A(x) * B(x) \equiv \left[e^{\frac{i}{2}\theta_{\mu\nu}\partial_{\zeta_\mu}\partial_{\eta_\nu}} A(x+\zeta)B(z+\eta) \right]_{\zeta=\eta=0} . \tag{2.6}$$

Note that to leading order in θ the $*$ product is given by

$$A(x) * B(x) = AB + \frac{i}{2}\theta^{\mu\nu}\partial_\mu A \partial_\nu B + \mathcal{O}(\theta^2) . \tag{2.7}$$

Hence the non-commutative version of an action for a quantum field theory can be obtained from the ordinary one by replacing the products of fields by star products. In doing so it is useful to define a generalized commutator, known as the Moyal bracket, for two quantities S, T as

$$[S, T]_{MB} = S * T - T * S , \tag{2.8}$$

so that the Moyal bracket of any quantity with itself vanishes. Note that the integration of a Moyal bracket of two quantities over all space-time vanishes, *i.e.*,

$$\int d^4x \; [S(x), T(x)]_{MB} = 0 , \tag{2.9}$$

which means they commute inside the integral. This can be generalized to show that the integral of a $*$ product of an arbitrary number of quantities is invariant under cyclic permutations in a manner similar to the trace of ordinary matrices. We also note that the Moyal bracket of two coordinates

$$[x_\mu, x_\nu]_{MB} = x_\mu * x_\nu - x_\nu * x_\mu , \tag{2.10}$$

mimics the operator commutation relation in Eq. 2.1.

Once the products of fields are replaced by $*$ products, infinite numbers of derivatives of fields can now appear in an action, implying that all such theories are non-local. This is not surprising since, in analogy with ordinary Quantum Mechanics, one now has a spacetime uncertainty relation

$$\Delta\hat{X}^\mu \Delta\hat{X}^\nu \geq \frac{1}{2}|\theta^{\mu\nu}| . \tag{2.11}$$

Theories with $c_{0i} \neq 0$ have an additional problematic feature in that they generally do not have a unitary S-matrix [6, 43, 90, 155], at least in perturbation theory, since an infinite number of time derivatives are involved in $*$ products. However, it has recently been shown [38] that it may be possible to unitarize the space-time case by combining the spatial NC Super Yang Mills limit with a Lorentz transformation with finite boost velocity. On the other hand, theories with only space-space non-commutativity, $c_{ij} \neq 0$, are unitary.

There are a number of important results in NCQFT which we now state without proof, referring the interested reader to the original papers for detailed explanations. (i) It has been shown that only the $U(n)$ matrix Lie algebra is closed under the Moyal bracket [35, 130], thus non-commutative gauge theories can be constructed only if they are based upon these gauge groups. Hence in order to embed the full SM in NCQFT, the usual Standard Model $SU(n)$ group factors must be extended to $U(n)$ groups. However, due to the effective non-abelian nature of the Moyal brackets, these $U(n)$ groups cannot be simply decomposed into products of $SU(n)$ and $U(1)$ factors. (ii) There are indications that conventional renormalizable, gauge invariant field theories remain renormalizable and gauge invariant when generalized to non-commutative spacetimes [19, 34, 51, 79, 119, 128, 131, 133, 134, 158], although a proof does not yet exist for theories which are spontaneously broken [40, 144]. (iii) Non-commutative QED, based on the group $U(1)$, has been studied by several groups [102, 148]; due to the presence of $*$ products and Moyal brackets, the theory takes on a non-abelian nature in that both 3-point and 4-point photon couplings are generated. The photonic part of the action is now

$$S_{NCQED} = \frac{-1}{4} \int d^4x \; F_{\mu\nu} * F^{\mu\nu} = \frac{-1}{4} \int d^4x \; F_{\mu\nu} F^{\mu\nu} \,, \tag{2.12}$$

where the second equality follows from the commutativity of Moyal brackets under integration, shown in Eq. 2.9. This action is gauge invariant under a local transformation $U(x)$ with $F_{\mu\nu}$ defined as

$$F_{\mu\nu} = \partial_\mu A_\nu - \partial_\nu A_\mu - i[A_\mu, A_\nu]_{MB} \,. \tag{2.13}$$

The origin of the 3- and 4-point functions is now readily transparent. Note that the photon's 2-point function is identical in commutative and NC spaces because quadratic forms remain unchanged. When performing the Fourier transformation of these new interactions into momentum space, the vertices pick up additional phase factors which are dependent upon the momenta flowing through the vertices. We will see below that these kinematic phases will play an important role in the collider tests of NCQFT. (*iv*) When fermions are added to the theory, covariant derivatives can only be constructed for fields of charge $0, \pm 1$. The structure of those derivatives for the $Q = \pm 1$ case is similar to that for fundamental and anti-fundamental representations in non-abelian theories. The covariant derivatives for neutral fields are either trivial (as in the case of abelian commutative $U(1)$ theory) or correspond to what would ordinarily be called the adjoint representation in the case of a commutative non-abelian theory. As before, the three-point function picks up an additional kinematic phase from the Fourier transformation of the interaction term into momentum space. This is shown explicitly in Fig. 2.1. The general form of the Feynman rules for NCQED can be found in Ref. [26]; the ones of relevance to the processes considered in this chapter are displayed in Fig. 2.1. (*v*) NCQED with fermions and space-space non-commutativity has been shown [159] to be CP violating yet CPT conserving.

Having now presented the basic formalism of NCQFT and subsequent modifications to QED, in the following sections we examine the effects in several $2 \to 2$ processes in e^+e^- collisions, including pair annihilation, Møller and Bhabha scattering, as well as in $\gamma\gamma \to \gamma\gamma$ scattering. We will see that the lowest order correction to the SM results for these transitions is given by dimension-8 operators. In addition, we find that an oscillatory azimuthal dependence is induced in these processes due to the preferred direction in the laboratory frame defined by the NC matrix $c_{\mu\nu}$. In summary, we will see that high energy linear colliders can probe non-commutative scales of order a TeV.

Before discussing our analysis for the specific processes considered here, a few additional comments are in order regarding the observation of these non-commutative effects. First, as discussed above, the vectors $c_i^E = [c_{0i}]$ and $c_i^B = [\epsilon_{ijk} c_{jk}]$ point in fixed specific directions which are the same in all reference frames. In our analysis below we define the z-axis as that corresponding to the direction of the incoming

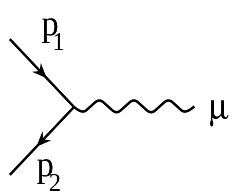

$$= ig\gamma^{\mu}\exp(ip_1\theta p_2/2)$$

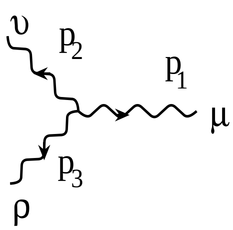

$$= 2g\sin(p_1\theta p_2/2)\,[(p_1 - p_2)^{\rho}g^{\mu\nu} + (p_2 - p_3)^{\mu}g^{\nu\rho} + (p_3 - p_1)^{\nu}g^{\mu\rho}]$$

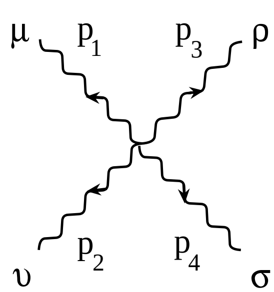

$$\begin{aligned} = 4ig^2[&(g^{\mu\sigma}g^{\nu\rho} - g^{\mu\rho}g^{\nu\sigma})\sin(p_1\theta p_2/2)\sin(p_3\theta p_4/2) \\ &+ (g^{\mu\rho}g^{\nu\sigma} - g^{\mu\nu}g^{\rho\sigma})\sin(p_3\theta p_1/2)\sin(p_2\theta p_4/2) \\ &+ (g^{\mu\nu}g^{\rho\sigma} - g^{\mu\sigma}g^{\nu\rho})\sin(p_1\theta p_4/2)\sin(p_2\theta p_3/2)] \end{aligned}$$

Figure 2.1: Feynman rules of NCQED.

particles in a fixed laboratory frame with the vectors **c** having arbitrary components in that frame. Now, imagine a second laboratory at a different point on the surface of the Earth performing the same experiment. Clearly the co-ordinate systems of the two laboratories will be different, *i.e.*, the beam directions and hence the z-axis will not be the same in the two locations. This implies that the experimentally determined values for the components of the **c** vectors will differ at the two laboratory sites due to their locally chosen set of co-ordinates. Hence *both* laboratories must convert their local co-ordinates to a common frame, *e.g.*, with respect to the rest frame of the 3 degree K blackbody radiation or some other slowly varying astronomical co-ordinate system, so that they would measure equivalent directions and magnitudes for **c**. This translation of co-ordinates to a common frame will be necessary if we are to compare the results of multiple experiments for signals of non-commutativity.

In addition, even for a single experiment, the apparent directions of the **c** vectors will vary with time due to the rotation of the Earth and its revolution about the Sun. While the actual **c** vectors will always point to the same position on the sky, the co-ordinates of this position will vary continuously in the laboratory frame due to the Earth's motion. (The effects of galactic motion should be small during the life-span of any given experiment.) Collider experiments will thus have to make use of astronometric techniques to continuously translate their laboratory co-ordinates to astronomical ones such that when events are recorded the relative orientation of the two frames would be accounted for. This should be a rather straightforward procedure for any future collider experiment to implement given that many non-accelerator based experiments already make use of these ideas.

Taking the Earth's motion into account is particularly important for experiments which measure observable quantities that are odd in **c**, including for example, the $g-2$ of the muon [102], the Lamb shift [46], as well as other processes which are linear [136] in the NC parameter. If only the laboratory co-ordinates were employed, at least some of the components of **c** would average to zero over a sidereal day. In the cases we discuss below, the observables are even functions of **c**, and while we would not obtain a null effect, time averaging would result in a diminished sensitivity to Λ_{NC}.

2.2 Møller Scattering

For all of the scattering processes considered in this chapter, except for $\gamma\gamma \to \gamma\gamma$, we can define the momenta of the incoming, represented by $p_{1,2}$, and outgoing, corresponding to $k_{1,2}$, particles in terms of the coordinates fixed in the laboratory as

$$\begin{aligned} p_1^\mu &= \tfrac{\sqrt{s}}{2}(1,-1,0,0) & p_2^\mu &= \tfrac{\sqrt{s}}{2}(1,1,0,0) \\ k_1^\mu &= \tfrac{\sqrt{s}}{2}(1,-c_\theta,-s_\theta c_\phi,-s_\theta s_\phi) & k_2^\mu &= \tfrac{\sqrt{s}}{2}(1,c_\theta,s_\theta c_\phi,s_\theta s_\phi)\,. \end{aligned} \tag{2.14}$$

Note that the ordering of the co-ordinates used in these definitions is given by (t,z,x,y), so that the z-axis is along the beam direction as usual. Using these definitions, the bilinear products of these momenta with the matrix $c_{\mu\nu}$, which appear in the Feynman rules of Fig. 2.1, can be calculated to be

$$\begin{aligned} p_1\cdot c\cdot p_2 &= \frac{s}{2}c_{01} \\ k_1\cdot c\cdot k_2 &= \frac{s}{2}[c_{01}c_\theta + c_{02}s_\theta c_\phi + c_{03}s_\theta s_\phi] \\ p_1\cdot c\cdot k_1 &= \frac{s}{4}[c_{01}(1-c_\theta) + (c_{12}-c_{02})s_\theta c_\phi - (c_{03}+c_{31})s_\theta s_\phi] \\ p_1\cdot c\cdot k_2 &= \frac{s}{4}[c_{01}(1+c_\theta) - (c_{12}-c_{02})s_\theta c_\phi + (c_{03}+c_{31})s_\theta s_\phi] \\ p_2\cdot c\cdot k_1 &= \frac{s}{4}[-c_{01}(1+c_\theta) - (c_{12}+c_{02})s_\theta c_\phi - (c_{03}-c_{31})s_\theta s_\phi] \\ p_2\cdot c\cdot k_2 &= \frac{s}{4}[-c_{01}(1-c_\theta) + (c_{12}+c_{02})s_\theta c_\phi + (c_{03}-c_{31})s_\theta s_\phi]\,. \end{aligned} \tag{2.15}$$

We remind the reader of the fact that $a\cdot c\cdot a = 0$ for all vectors a due to the antisymmetry of the matrix c. Note that c_{23} does not appear in any of the above expressions since we have defined the z-axis to be along the direction of the initial beams and there is no **B** field associated non-commutative asymmetry relative to this direction.

The Feynman diagrams which mediate Møller scattering are displayed in Fig. 2.2. In this case, the NC modifications correspond to the kinematic phase which appears in each vertex. The question here is how to treat the Z-boson exchange contribution. While NCQED is a well defined theory, it is not immediately clear how to extend it to the full SM in a naive way even if we are only interested in tree-level fermionic interactions. Without such guidelines we see that there exist three possibilities: (i) the simplest case is if the Z and photon have the same vertex structure as shown in Fig. 2.1, (ii) the full theory and appropriate $Zf\bar{f}$ kinematic phase are more complex, or (iii) only $\gamma f\bar{f}$ vertices pick up kinematic phases. Clearly, as far as signatures of non-commutativity are concerned, cases one and three will be qualitatively similar. Hence, for simplicity, we assume that the first possibility is realized.

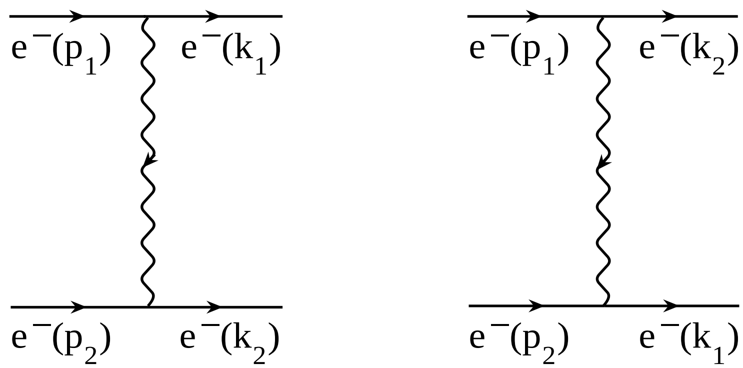

Figure 2.2: Feynman graphs contributing to Møller scattering, with the exchanged particle corresponding to a photon and Z=boson.

Following the Feynman rules of Fig. 2.1 and the momentum labeling given in Fig. 2.2 we see that the t- and u-channel exchange graphs now pick up kinematic phases given by

$$\begin{aligned} \phi_t &= \frac{1}{2}[p_1 \cdot \theta \cdot k_1 + p_2 \cdot \theta \cdot k_2] \\ \phi_u &= \frac{1}{2}[p_1 \cdot \theta \cdot k_2 + p_2 \cdot \theta \cdot k_1]\,. \end{aligned} \tag{2.16}$$

Clearly, only the interference terms between the t- and u-channel diagrams pick up a relative phase when the full amplitude is squared. We define this phase as Δ_{Moller} and find it to be given by

$$\Delta_{Moller} = \phi_u - \phi_t = \frac{-\sqrt{ut}}{\Lambda_{NC}^2}[c_{12}c_\phi - c_{31}s_\phi]\,, \tag{2.17}$$

with the second equality following from Eq. 2.16. (We define the Mandelstam variables as usual: $t, u = -s(1 \mp \cos\theta)/2$.) Hence the resulting differential distributions for this process appear exactly as in the SM except that the t, u-channel interference terms should be multiplied by $\cos\Delta_{Moller}$. Note that all of the terms involving time-space non-commutativity have dropped out of the expression for Δ_{Moller}. In addition, as we take the limit $\Lambda_{NC} \to \infty$, $\cos\Delta \to 1$ so that the SM is recovered. In the limit of small s/Λ_{NC}^2, $\cos\Delta_{Moller}$ can be expanded where it is seen that the lowest order correction to the SM occurs at dimension-8. Perhaps the most important thing to notice, as discussed above, is that $\Delta_{Moller} \neq 0$ induces a ϕ dependence in a $2 \to 2$ scattering process since there now exists a preferred direction in the laboratory frame.

For simplicity in our numerical results presented below, we will only consider the case $c_{12} \neq 0$. If instead c_{31} is non-zero, the results will be similar except for the phase of the ϕ dependence. When both terms are present, the situation is in general somewhat more complex, yet will be qualitatively comparable to the case analysed below. Since we only consider one non-vanishing value of c_{ij} at a time, we set its magnitude to unity when obtaining our results.

The differential cross section for Møller scattering in the laboratory center of mass frame can be written as

$$\frac{d\sigma}{dz\, d\phi} = \frac{\alpha^2}{4s}\Big[(e_{ij}+f_{ij})(P_{ij}^{uu}+P_{ij}^{tt}+2P_{ij}^{ut}\cos\Delta_{Moller}) + (e_{ij}-f_{ij})(\frac{t^2}{s^2}P_{ij}^{uu}+\frac{u^2}{s^2}P_{ij}^{tt})\Big], \tag{2.18}$$

where $z = \cos\theta$, a sum over the gauge boson indices is implied, $e_{ij} = (v_i v_j + a_i a_j)^2$ and $f_{ij} = (v_i a_j + a_i v_j)^2$ are combinations of the electron's vector and axial vector couplings and

$$P_{ij}^{qr} = s^2 \frac{(q-m_i^2)(r-m_j^2)+\Gamma_i\Gamma_j m_i m_j}{[(q-m_i^2)^2+(\Gamma_i m_i)^2][(r-m_j^2)^2+(\Gamma_j m_j)^2]}, \tag{2.19}$$

with $m_i(\Gamma_i)$ being the mass (width) of the i^{th} gauge boson, where i=1(2) corresponds to the photon(Z). The expression for the differential Left-Right Polarization asymmetry, $A_{LR}(z,\phi)$, can be easily obtained from the above by forming the ratio

$$A_{LR}(z,\phi) = N(z,\phi)/D(z,\phi)\,, \tag{2.20}$$

where $D(z,\phi)$ is the differential cross section expression above and $N(z,\phi)$ can be obtained from $D(z,\phi)$ by the redefinition of the coupling combinations e_{ij} and f_{ij} as

$$e_{ij} = f_{ij} = (v_i v_j + a_i a_j)(v_i a_j + a_i v_j)\,. \tag{2.21}$$

Although we have expressed the cross section in an apparently covariant form using Mandelstam variables, it is not actually invariant due to the presence of Δ_{Moller} which is highly frame dependent.

Figure 2.3 displays the effect of a finite value of $\Lambda_{NC} = \sqrt{s}$ on the shape of the conventional bin-integrated, z-dependent event rate and A_{LR} for a 500 GeV linear collider assuming an integrated luminosity of 300 fb^{-1}. In presenting these results we have neglected initial state radiation and beamstrahlung effects, assumed both beams are 90% polarized with $\delta P/P = 0.003$, and taken an overall luminosity error of 1%. Angular cuts of $\theta = 10^o$ have also been applied but the entire ϕ range has been integrated over. As we can see from this figure, the influence of $\Lambda_{NC}^{-1} \neq 0$ appears to cause a small downward shift in the $\cos\theta$ distribution which is most noticeable at large scattering angles away from the forward and backward t- and u-channel poles from the photon exchange graph. The effect of a finite value of Δ_{Moller} is thus seen to increase the amount of destructive interference between the u- and t-channel graphs. Although the shift is apparently small it occurs over many bins and is statistically quite significant given the size of the errors at this integrated luminosity. For A_{LR} there is hardly any shift from the SM values in this case.

Figure 2.4 presents the z-integrated, ϕ dependent distribution for both the rate and A_{LR}. Note that as we perform more restrictive cuts on $|z|$, the central region, which is the most sensitive to Λ_{NC}, is becoming more isolated. As can be seen from the figures, this approach enhances the ϕ dependence for the differential cross section. Though the ϕ dependence also appears to be rather weak, it is again statistically significant at this large integrated luminosity. As in the case of the ϕ-integrated A_{LR}, the z-integrated A_{LR} shows hardly any sensitivity to finite Λ_{NC} even when a strong $|z|$ cut is applied.

In order to obtain a 95% CL lower bound on Λ_{NC} from Møller scattering we

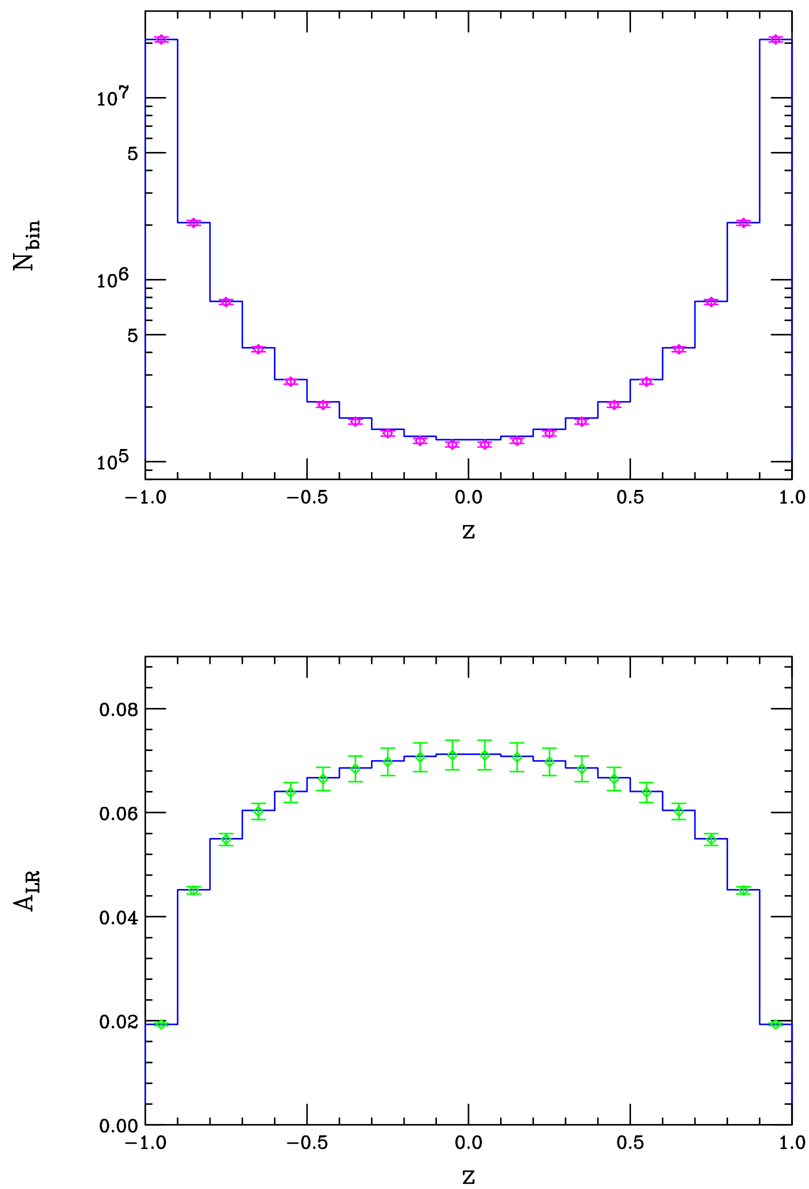

Figure 2.3: Binned cross section (top) and polarized asymmetry (bottom) as a function of $z = \cos\theta$ for Møller scattering at a 500 GeV linear collider assuming an integrated luminosity of 300 fb^{-1}. The histogram is the SM expectation while the data corresponds to $\Lambda_{NC} = \sqrt{s}$.

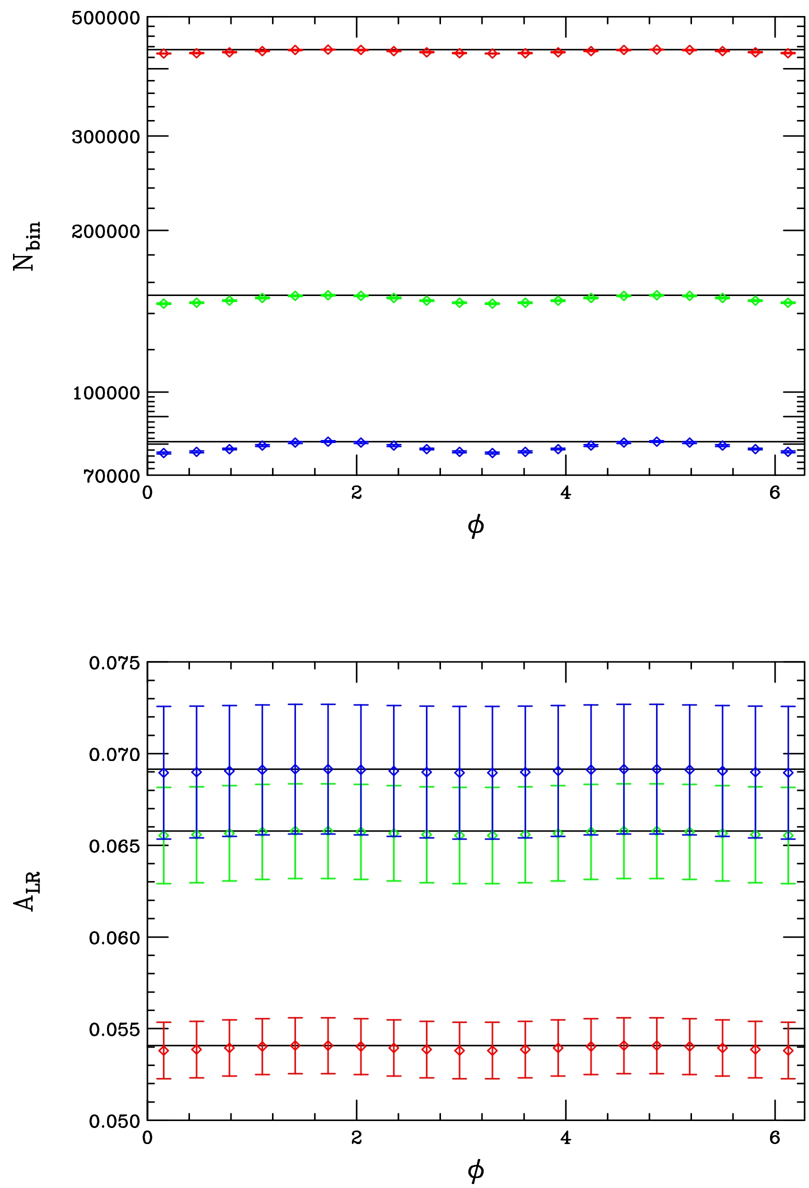

Figure 2.4: ϕ dependence of the Møller cross section (top) and left-right asymmetry (bottom) for the SM (straight lines) and for the case $\Lambda_{NC} = \sqrt{s}$ (shown as data) at a 500 GeV linear collider with a luminosity of 300 fb^{-1}. From top to bottom in the top panel a z cut of 0.9(0.7, 0.5) has been applied with the order reversed in the lower panel.

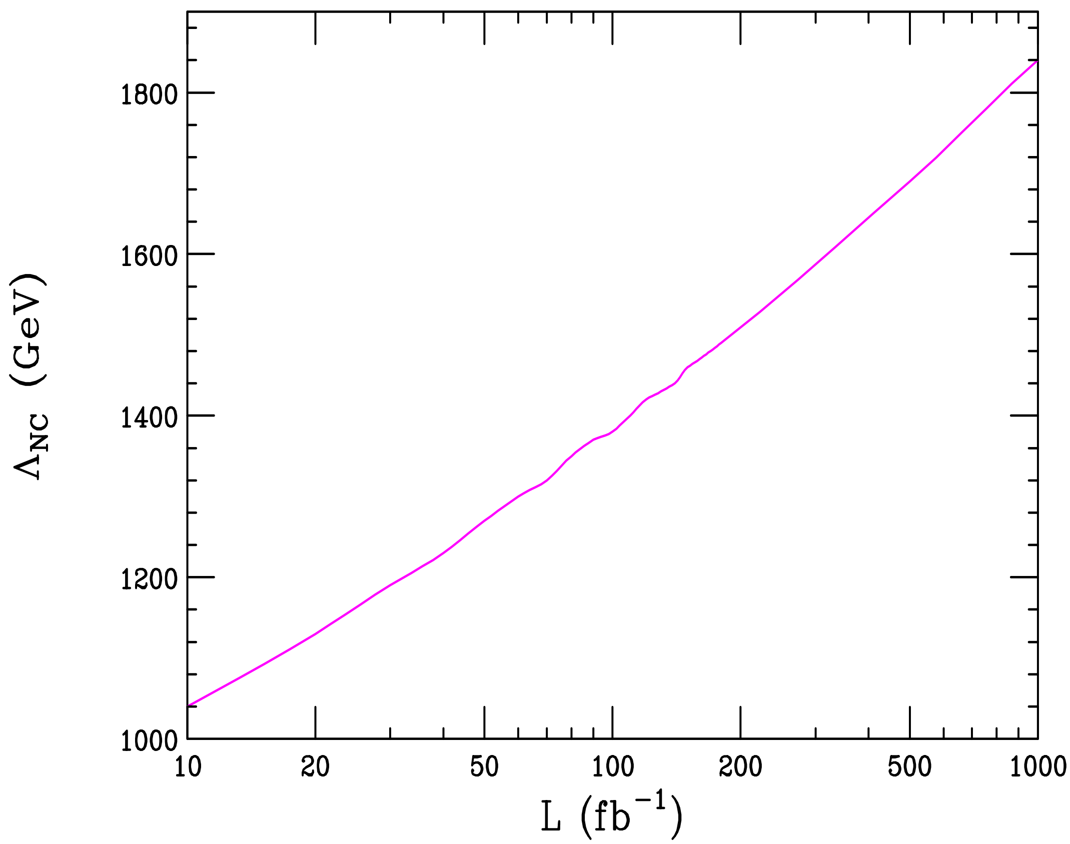

Figure 2.5: 95% CL lower bound on Λ_{NC} at a 500 GeV linear collider as a function of the integrated luminosity from Møller scattering via the fit described in the text.

perform a combined fit to the total cross section, the shape of the doubly differential $z-\phi$ angular distribution and $A_{LR}(z,\phi)$. In the latter two cases we bin the NC results in a 20×20 array of z,ϕ values and employ only statistical errors apart from the polarization uncertainty. In the case of the total rate we also include the luminosity uncertainty in the error. For a fixed value of luminosity we then compare the predictions of the SM with the case where Λ_{NC} is finite and repeat this procedure by varying Λ_{NC} until we obtain a 95% CL bound by using a χ^2 fit. From this procedure we obtain the search reach on Λ_{NC} as a function of the integrated luminosity as displayed in Fig. 2.5. As we can see from this figure, bounds on Λ_{NC} of order $(3-3.5)\sqrt{s}$ are obtained for reasonable luminosities.

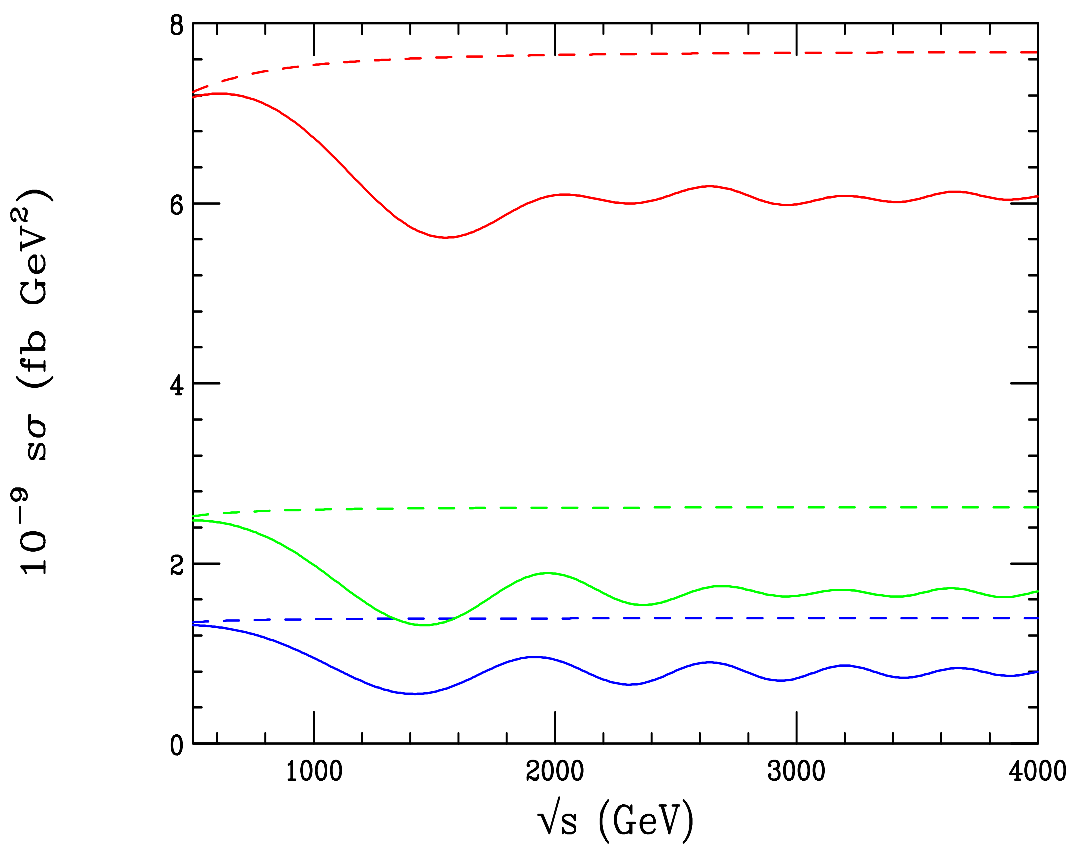

Figure 2.6: Scaled dependence of the Møller total cross section, subject to a angular cut (from top to bottom) of $|z|\leq 0.9(0.7,\ 0.5)$ assuming the SM (dashed curves) or Λ_{NC} =500 GeV (solid curves).

We now examine how the Møller cross section behaves as $\sqrt{s}$ grows beyond Λ_{NC}. In the SM for large s we expect the scaled cross section, *i.e.*, the product $s \cdot \sigma_{Moll}$, to be roughly constant after a cut on $|\cos\theta|$ cut is performed. Ordinarily when new operators are introduced, the modified scaled cross section is expected to grow rapidly near the appropriate scale beyond which the contact interaction limit no longer applies. However, in the present case, the theory above the scale Λ_{NC} *is* a well-defined theory since it is not a low energy limit. We would thus anticipate that the $\cos\Delta_{Moller}$ factor leads to a modulation of the scaled cross section that averages out rapidly with a period that depends on the hardness of the $|\cos\theta|$ cut as the value of $\sqrt{s}$ increases. This effect is displayed in Fig. 2.6 and behaves exactly as expected.

2.3 Bhabha Scattering

The Feynman graphs which mediate Bhabha scattering in NCQED are given in Fig. 2.7. In this case, the t-and s-channel kinematic phases are now given by

$$\begin{aligned} \phi_t &= \frac{-1}{2}[p_1 \cdot \theta \cdot k_1 - p_2 \cdot \theta \cdot k_2] \\ \phi_s &= \frac{-1}{2}[p_1 \cdot \theta \cdot p_2 - k_1 \cdot \theta \cdot k_2], \end{aligned} \tag{2.22}$$

which implies that the interference term between the two amplitudes is sensitive to $\cos\Delta_{Bhabha}$ which is given by

$$\Delta_{Bhabha} = \phi_s - \phi_t = \frac{-1}{\Lambda_{NC}^2}[c_{01}t + \sqrt{ut}(c_{02}c_\phi + c_{03}s_\phi)]\,. \tag{2.23}$$

Note that whereas Møller scattering was sensitive to space-space non-commutativity we see that Bhabha scattering is instead sensitive to time-space non-commutativity. Here we see that there are two distinct cases depending whether or not Δ_{Bhabha} has a ϕ dependence. If c_{01} is non-zero then the ϕ dependence will be absent, whereas the two cases $c_{02}, c_{03} \neq 0$ are essentially identical except for the phase of the ϕ dependence. We thus only consider the cases $c_{01} = 1$ or $c_{02} = 1$.

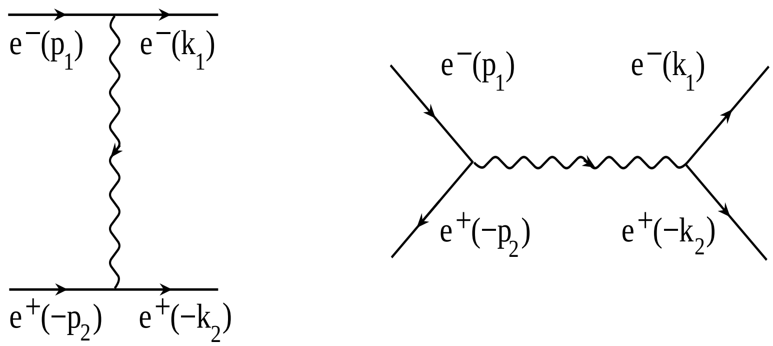

Figure 2.7: Feynman graphs contributing to Bhabha scattering with the exchanged particle corresponding to a photon and Z-boson.

Using the notation above, the differential cross section in the laboratory center of mass frame for Bhabha scattering can then be written as

$$\frac{d\sigma}{dz\;d\phi} = \frac{\alpha^2}{2s}\left[(e_{ij}+f_{ij})(P_{ij}^{ss}+P_{ij}^{tt}+2P_{ij}^{st}\cos\Delta_{Bhabha})\frac{u^2}{s^2}+(e_{ij}-f_{ij})(P_{ij}^{ss}\frac{t^2}{s^2}+P_{ij}^{tt})\right], \tag{2.24}$$

with $A_{LR}(z,\phi)$ defined in a manner similar to that for Møller scattering by forming the ratio $N(z,\phi)/D(z,\phi)$.

We first consider the case where c_{01} is taken to be non-zero. Figure 2.8 displays the (in this case trivial) ϕ integrated angular distribution and A_{LR} for the SM with $\Lambda_{NC} = \sqrt{s} = 500$ GeV. Here one sees that a finite value of Λ_{NC}^{-1} leads to a slight increase in the cross section at large angles and a moderate change in A_{LR} in the same z range. In the case where c_{02} is non-zero, Fig. 2.9 shows the corresponding distributions. Note that the shift in the cross section looks almost identical in the two cases but the deviation in A_{LR} is more shallow in the latter case. Figure 2.10 shows the ϕ dependence of the z-integrated distributions for the same three cuts on $\cos\theta$ discussed above in the case of Møller scattering. As before we see that the effect in the cross section is most visible for stiffer cuts which isolate the central region. In the case of A_{LR} the ϕ dependence is too small at these integrated luminosities to be visible. In order to obtain a 95% CL lower bound on Λ_{NC} from Bhabha scattering we

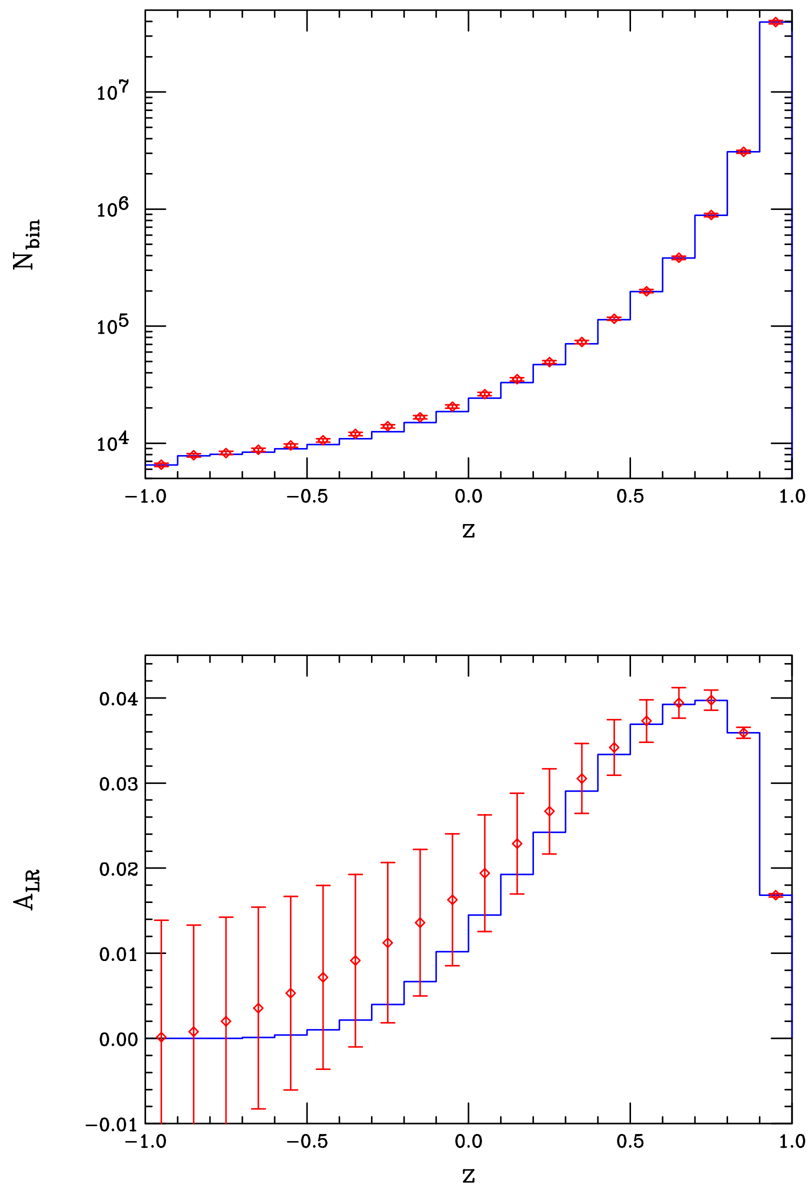

Figure 2.8: Same as Fig. 2.3 but now for Bhabha scattering assuming that c_{01} is non-zero.

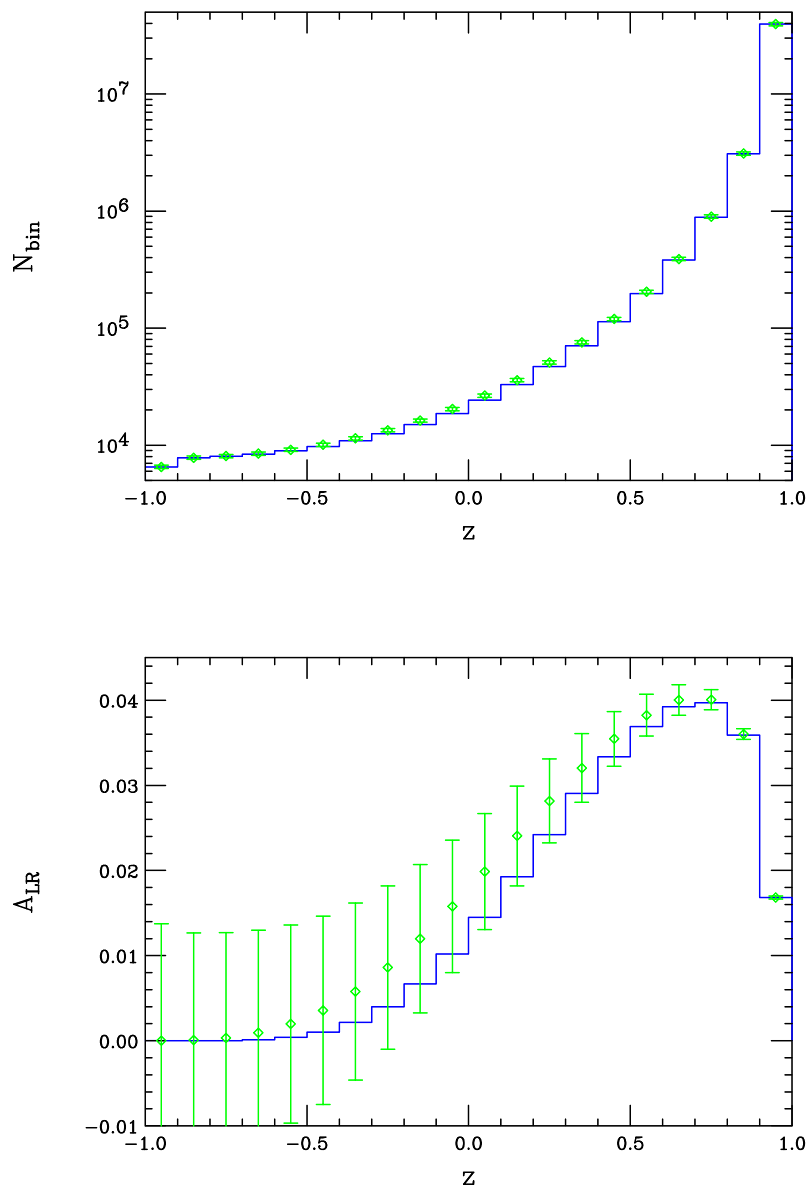

Figure 2.9: Same as in Fig. 2.8 but now assuming that c_{02} is non-zero.

follow the same procedure as that discussed above for Møller scattering and obtain the results presented in Fig. 2.11. Here we see that the reach for Λ_{NC} via Bhabha scattering is not quite as good as what we had found earlier for the case of Møller scattering, given only by $\simeq 2\sqrt{s}$, for both of the cases considered.

Figures 2.12 and 2.13 show the scaled cross sections for Bhabha scattering after the z cuts are employed for values of $\sqrt{s} > \Lambda_{NC}$. Here we see that for both cases, the presence of a finite value for Δ_{Bhabha} leads to an increase in the constructive interference between the s- and t-channel exchanges with two very different periods. Again for values of $\sqrt{s}$ much larger than Λ_{NC} we see that the oscillations average out to approximately half of their original amplitude.

2.4 Pair Annihilation

The Feynman diagrams which contribute to pair annihilation in NCQED are shown in Fig. 2.14. Note that in this case, there is a novel s-channel contribution in NC field theories from the 3γ self-coupling, in addition to the kinematical phase factor which appears at each vertex. Due to the presence of the non-abelian like coupling, one must exercise caution in calculating the cross section to ensure that the Ward identities are satisfied and to guarantee that unphysical polarization states are not produced. Hence one must either extend the polarization sum to incorporate transverse photon polarization states or include the contribution from the production of a ghost-antighost pair to cancel the contribution of the unphysical gauge boson polarizations. This procedure is similar in manner to that performed for the parton-level scattering of $q\bar{q} \to gg$ in QCD. We find that the differential cross section in the laboratory center of mass frame for pair annihilation in NCQED is then given by

$$\frac{d\sigma}{dz\,d\phi} = \frac{\alpha^2}{4s}\left[\frac{u}{t} + \frac{t}{u} - 4\,\frac{t^2+u^2}{s^2}\sin^2(\frac{1}{2}k_1 \wedge k_2)\right], \tag{2.25}$$

where we have introduced the wedge product defined as $p \wedge k = p_\mu k_\nu \theta^{\mu\nu}$. Note that in this case, the contribution from the relative phases from the interference terms cancels. We also note that the sign of the modification due to NCQED does not vary

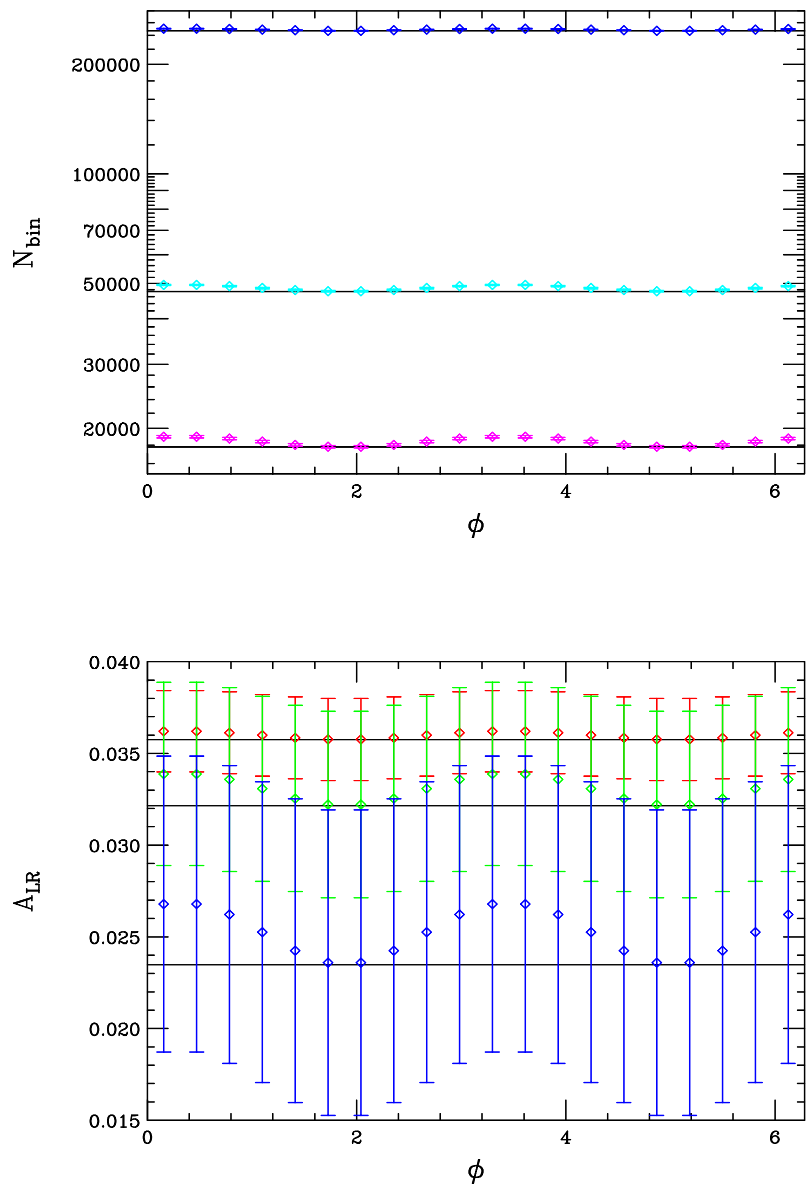

Figure 2.10: Same as Fig. 2.4 but now for Bhabha scattering with c_{02} taken to be non-zero. The order for the cuts on $|\cos\theta|$ is reversed in the lower plot.

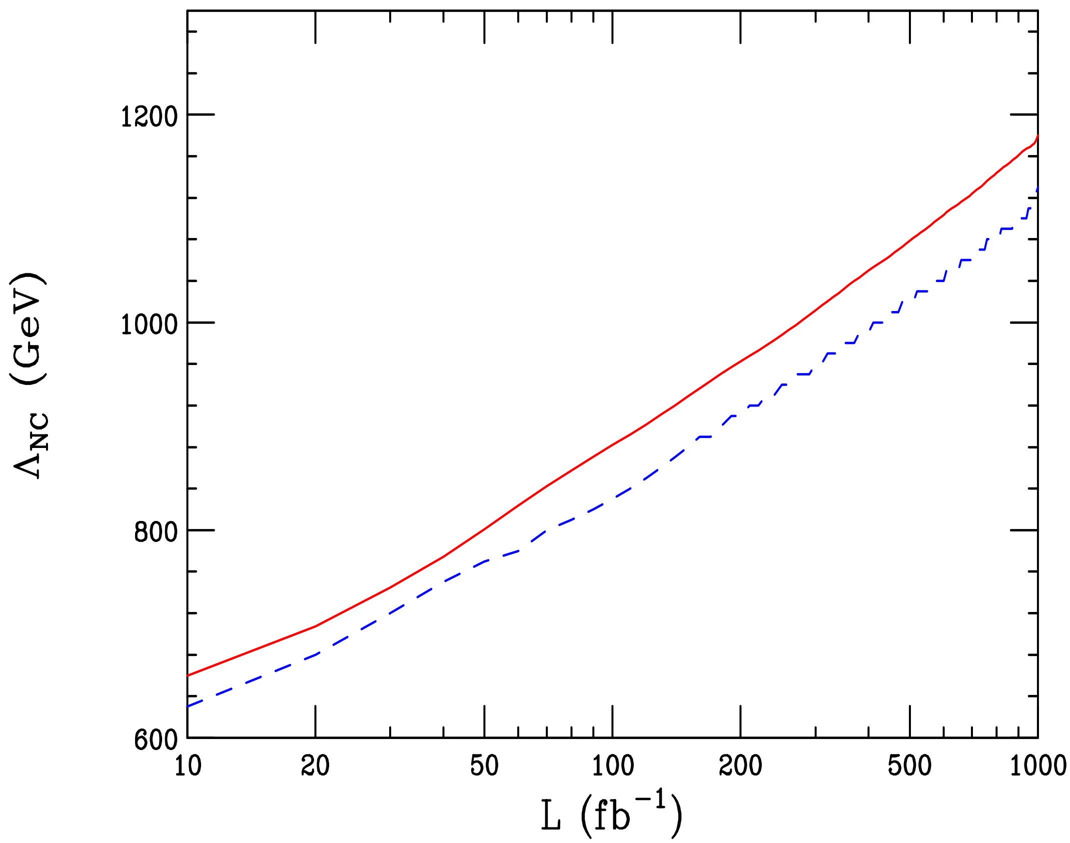

Figure 2.11: 95% CL bounds on Λ_{NC} as a function of luminosity from Bhabha scattering assuming either c_{01} (solid) or c_{02} (dashed) is non-zero.

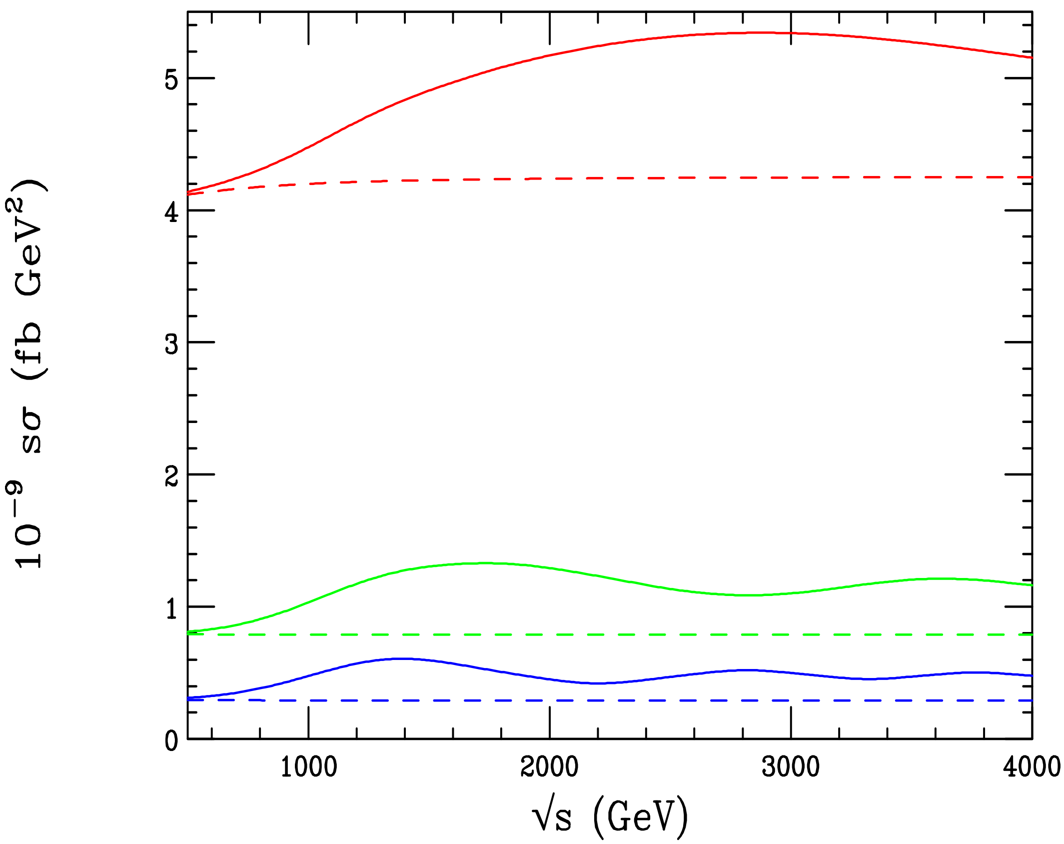

Figure 2.12: The scaled cross section for Bhabha scattering with c_{01} non-zero.

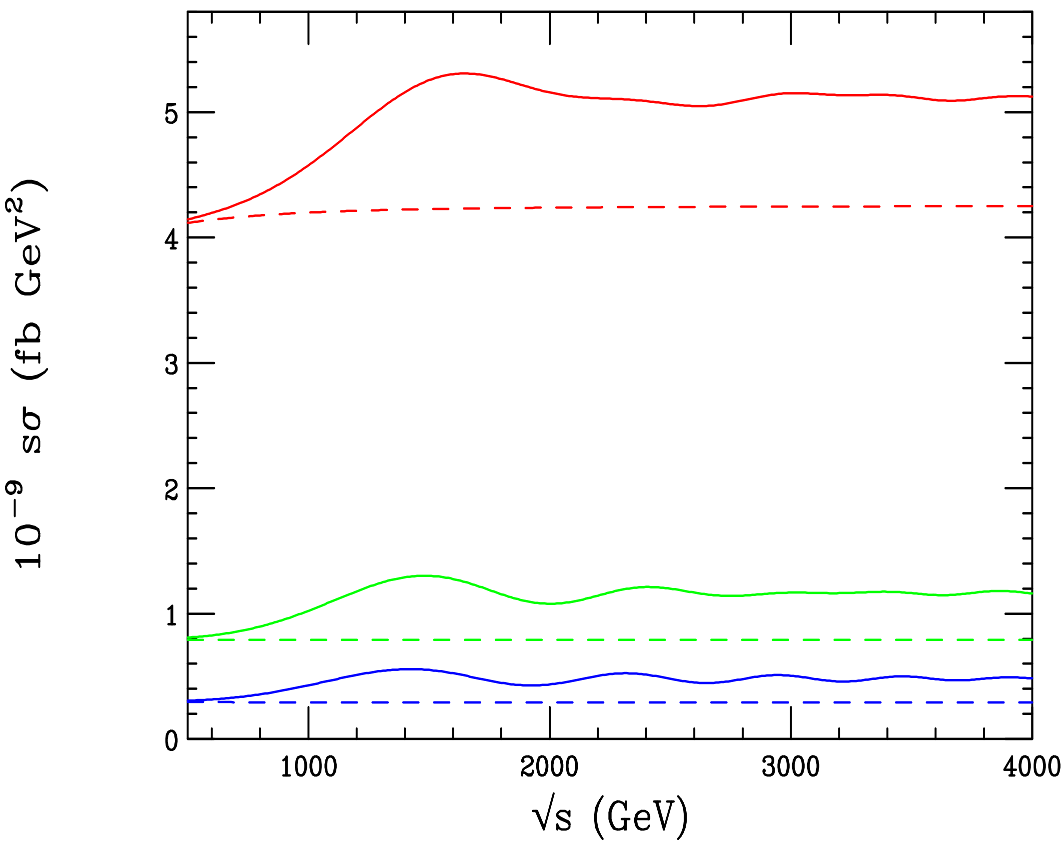

Figure 2.13: Same as in the previous figure but now with c_{02} non-zero.

since it is an even function and hence the effect does not wash out over time due to the rotation of the Earth.

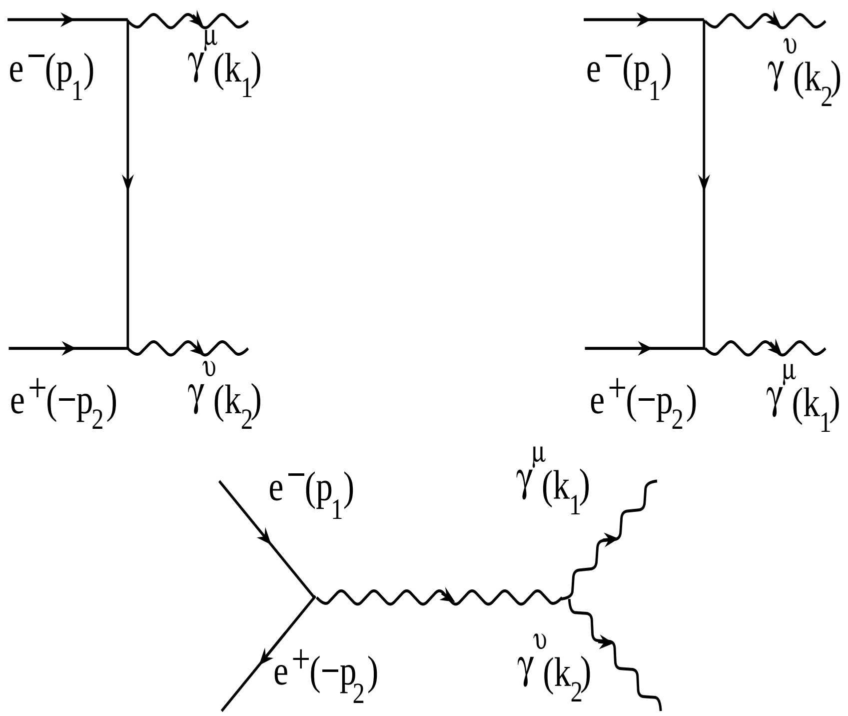

Figure 2.14: The three tree level contributions to $e^+e^- \to \gamma\gamma$ in NCQED.

Evaluating the wedge product yields

$$\Delta_{PA} \equiv \frac{1}{2} k_1 \wedge k_2 = \frac{-s}{2\Lambda_{NC}^2}\left[c_{01}c_\theta + c_{02}s_\theta c_\phi + c_{03}s_\theta s_\phi\right]. \tag{2.26}$$

Note that this process is sensitive only to space-time non-commutativity. We again stress that this is only true in the CM frame; due to the violation of Lorentz invariance this will not hold in all reference frames. As discussed above, it is important to remember that although we have expressed the cross section in terms of the Lorentz invariant Mandelstam variables, $s\,, t\,, u$, the phase Δ_{PA} is not Lorentz invariant. For this reaction, we parameterize the c_{0i} by introducing the angles characterizing the background **E** field of the theory:

$$\begin{aligned} c_{01} &= \cos\alpha \\ c_{02} &= \sin\alpha\cos\beta \\ c_{03} &= \sin\alpha\sin\beta\,, \end{aligned} \tag{2.27}$$

so that

$$\begin{aligned} \Delta_{PA} &= \frac{-s}{2\Lambda_{NC}^2}\Big[\cos\theta\cos\alpha+\sin\theta\sin\alpha\cos(\phi-\beta)\Big] \\ &= \frac{-s}{2\Lambda_{NC}^2}\cos\theta_{NC}\,, \end{aligned} \tag{2.28}$$

where θ_{NC} is the angle between the **E** field and the direction of the outgoing photon denoted with momenta k_1. Note that β simply defines the origin of the ϕ axis; we will hereafter set $\beta = \pi/2$. This parameterization provides a good physical interpretation of the NC effects. (Note that the c_{0i} are not independent; in pulling out the overall scale Λ_{NC} we can always impose the constraint $|c_{01}|^2 + |c_{02}|^2 + |c_{03}|^2 = 1$.) Here, we consider three physical cases: $\alpha = 0$, $\alpha = \pi/2$, and $\alpha = \pi/4$, which correspond to the background **E** fields being at an angle α from the beam axis. The correction term Δ_{PA} then takes the following forms in each of these cases:

$$\begin{aligned} \Delta_{PA}(\alpha=0) &= \frac{-s}{2\Lambda_{NC}^2}\cos\theta \\ \Delta_{PA}(\alpha=\pi/2) &= \frac{-s}{2\Lambda_{NC}^2}\sin\theta\sin\phi \\ \Delta_{PA}(\alpha=\pi/4) &= \frac{-s}{2\sqrt{2}\Lambda_{NC}^2}\Big[\cos\theta+\sin\theta\sin\phi\Big]. \end{aligned} \tag{2.29}$$

As in the previous processes we considered, a striking feature of these correction terms are their ϕ dependence, arising from a preferred direction which is not parallel to the beam axis.

In Figs. 2.15 and 2.16 we present the bin-integrated event rates, taking $\Lambda_{NC} = \sqrt{s}$ for purposes of demonstration, which show the angular dependences of the NC deviations for the two cases $\alpha = \pi/2$ and $\alpha = 0$, taking $\Lambda_{NC} = \sqrt{s} = 500$ GeV

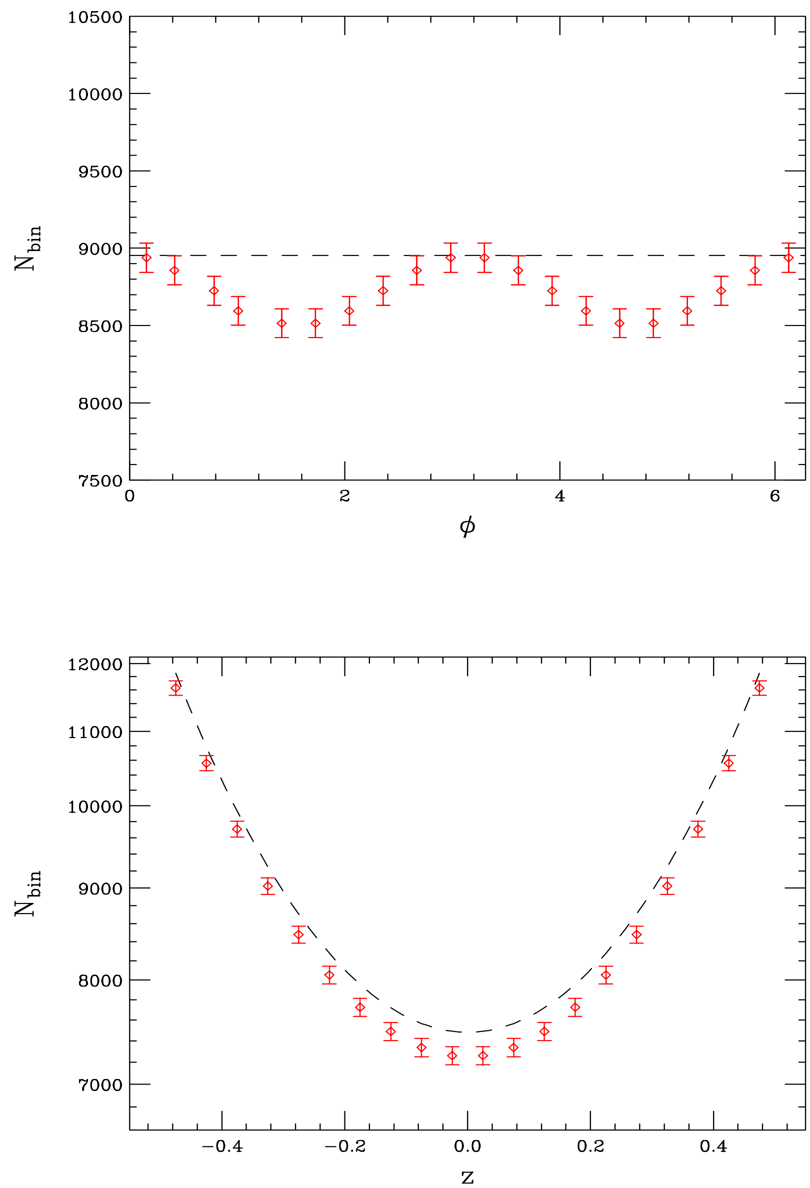

Figure 2.15: ϕ dependence (top) and θ dependence (bottom) of the $e^+e^- \to \gamma\gamma$ cross section for the case $\alpha = \pi/2$. We take $\Lambda_{NC} = \sqrt{s} = 500$ GeV, and assume a luminosity of $500\,\mathrm{fb}^{-1}$. In the top panel a cut of $|z| < 0.5$ has been employed. The dashed line corresponds to the SM expectations and the 'data' points represent the NCQED results.

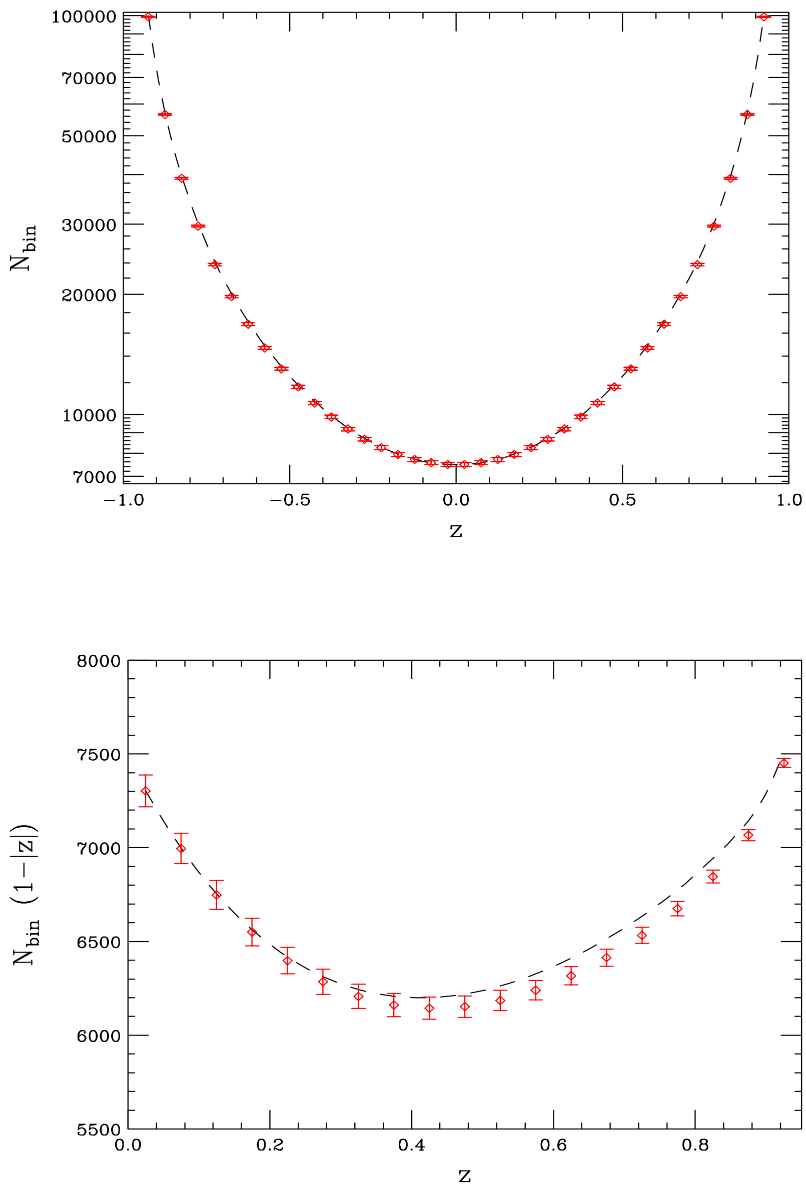

Figure 2.16: θ dependence of the $e^+e^- \to \gamma\gamma$ cross section for the case $\alpha = 0$. We again use $\Lambda_{NC} = \sqrt{s} = 500$ GeV, and a luminosity of $500\,\mathrm{fb}^{-1}$. In the bottom panel, note that the number of events in each bin is scaled by $1 - |z|$.

and a luminosity of $500\,\mathrm{fb}^{-1}$. For the case of $\alpha = 0$ we have also scaled the angular distribution by the factor $1-|z|$ in order to emphasize the deviation from the Standard Model in the peaking region. Note that the NC contributions lower the event rate from that expected in the SM in the central region. As expected, the $\alpha = 0$ case shows no ϕ dependence since the preferred direction is parallel to the beam axis, while the ϕ distribution for $\alpha = \pi/2$ exhibits a strong oscillatory behavior. The case $\alpha = \pi/4$, as well as more general choices of α, simply extrapolates between these two extremes.

To obtain a 95% CL lower bound on Λ_{NC}, we perform a fit to the total cross section and the angular distributions employing the procedure discussed above. Our results are presented in Fig. 2.17 for three values of α, where we see that the NC search reach from pair annihilation is approximately given by $1.5\sqrt{s}$. This is inferior in comparison to that obtained in the case of Møller and Bhabha scattering, due, in part, to the large available statistics in the latter cases. The scaled cross sections, after employing identical z cuts as in the previous two sections, are presented in Fig. 2.18. Here, we see again that the anticipated high energy behavior is realized.

2.5 $\gamma\gamma \to \gamma\gamma$ at Linear Colliders

Future linear colliders have the option of running in a $\gamma\gamma$ collision mode [82, 83], in which laser photons are Compton back-scattered off the incoming fermion beams. The lowest order SM contributions arise at the 1-loop level with fermions and W bosons propagating in the loop. Since the exact SM calculation of this box diagram mediated process is rather tedious [111], there exist various approximations in the literature [93, 94] which are valid in the regime where the center of mass energy is large compared to the W mass. Since this process only occurs at loop-level in the SM, it has been proposed as a useful test of new physics which contributes to the amplitude at the tree level in, for example, supersymmetry[93, 94] or quantum gravity models with large extra dimensions [65]. In the present case, NCQED also predicts new contributions to $\gamma\gamma \to \gamma\gamma$ at tree-level, and hence we examine how well this process can bound Λ_{NC}.

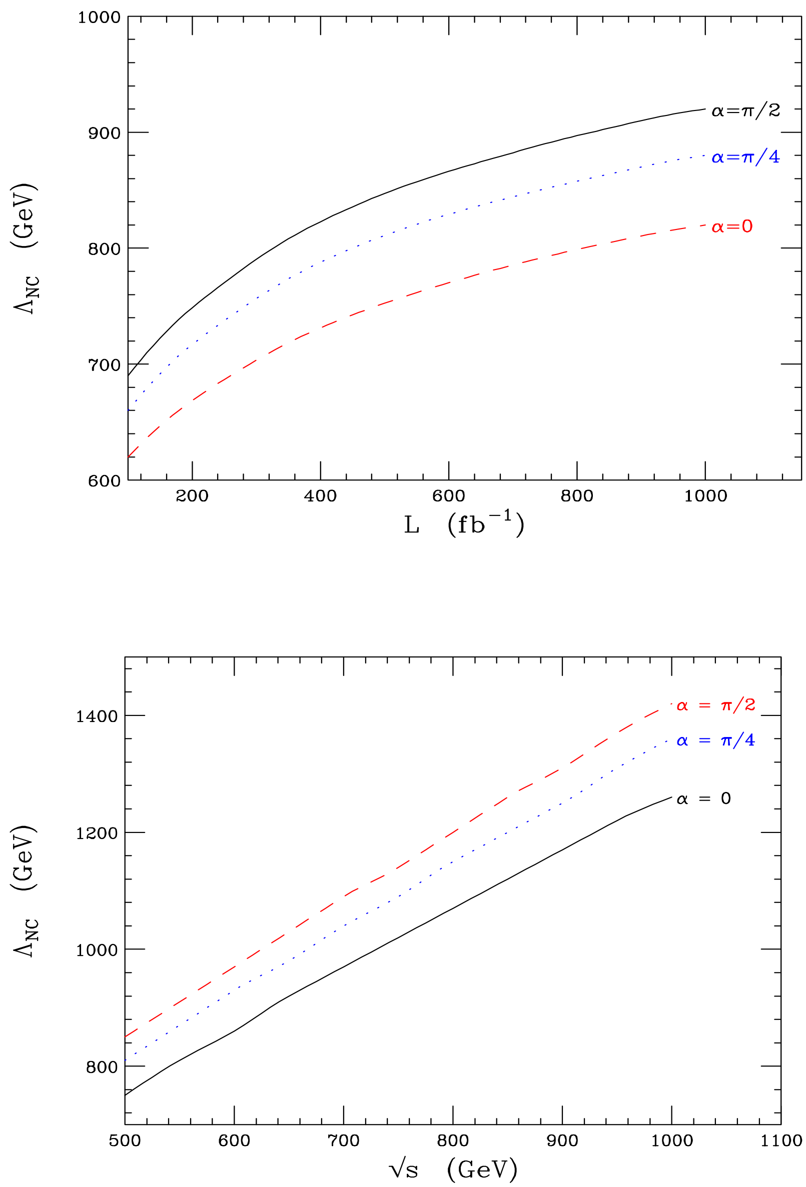

Figure 2.17: 95% CL bound on Λ_{NC} from pair annihilation as a function of luminosity (top) and $\sqrt{s}$ (bottom). In the top panel we set $\sqrt{s} = 500$ GeV, while in the bottom panel we assume a luminosity of $500\,\mathrm{fb}^{-1}$.

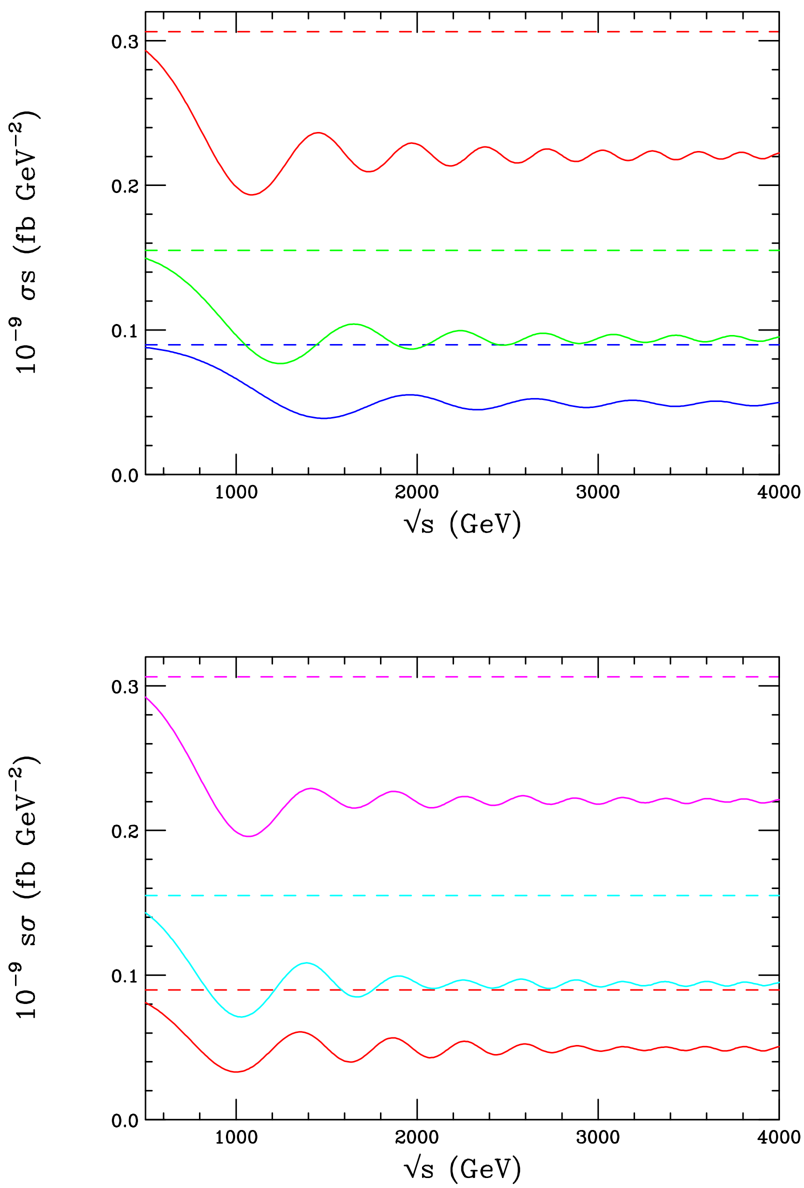

Figure 2.18: The scaled cross section for pair annihilation for $\alpha = 0, \pi/2$ corresponding to the (top, bottom) panels, respectively.

We will consider only tree-level NC contributions since the NC generalization of the full electroweak SM is unknown and coupling constant suppressed. There are four diagrammatic contributions in this case: three from the s, t, and u channels of photon exchange and one from the four-point photon coupling. These are presented in Fig. 2.19. Denoting the incoming photon momenta by p_1 and p_2, and the outgoing photon momenta by k_1 and k_2 as before, we find six non-vanishing NC helicity amplitudes:

$$\begin{aligned}
\mathcal{M}^{NC}_{+--+} &= -32\pi\alpha\,\frac{\hat{t}}{\hat{s}}\left[\sin(\frac{1}{2}p_1\wedge k_1)\sin(\frac{1}{2}p_2\wedge k_2)+\frac{\hat{t}}{\hat{u}}\sin(\frac{1}{2}p_1\wedge k_2)\sin(\frac{1}{2}p_2\wedge k_1)\right]\\
\mathcal{M}^{NC}_{++++} &= 32\pi\alpha\left[\frac{\hat{u}-\hat{t}}{\hat{s}}\sin(\frac{1}{2}p_1\wedge p_2)\sin(\frac{1}{2}k_1\wedge k_2)\;+\;\left(\frac{\hat{u}}{\hat{t}}-\frac{2\hat{u}}{\hat{s}}\right)\sin(\frac{1}{2}p_1\wedge k_1)\right.\\
&\quad\left.\times\sin(\frac{1}{2}p_2\wedge k_2)+\left(\frac{\hat{t}}{\hat{u}}-\frac{2\hat{t}}{\hat{s}}\right)\sin(\frac{1}{2}p_1\wedge k_2)\sin(\frac{1}{2}p_2\wedge k_1)\right], \qquad (2.30)
\end{aligned}$$

where we have made use of the relation $\hat{s}+\hat{t}+\hat{u}=0$ and the $\hat{s}$ denotes the parton-level center-of-mass frame. The other four amplitudes are related to these by $\mathcal{M}^{NC}_{----} = \mathcal{M}^{NC}_{++++}$; $\mathcal{M}^{NC}_{+--+}(k_1,k_2) = \mathcal{M}^{NC}_{-++-}(k_1,k_2) = \mathcal{M}^{NC}_{+-+-}(k_2,k_1) = \mathcal{M}^{NC}_{-+-+}(k_2,k_1)$. The corresponding SM amplitudes can be found in Refs. [93, 94] and will be given in Appendix A.

The kinematics of this process are more complicated than those of the previous cases. The backscattered photons have a broad energy distribution, and the collision no longer occurs in the center of mass frame, *i.e.*, the CM and laboratory frames no longer coincide. As NC theories violate Lorentz invariance, the differential cross section is no longer invariant under boosts along the z-axis and we are thus forced to consider this process in the laboratory frame. Letting x_1 and x_2 denote the fraction of the fermion energy carried by each of the backscattered photons, the photon momenta become

$$\begin{aligned}
p_1^\mu &= \frac{x_1\sqrt{s}}{2}(1,1,0,0)\\
p_2^\mu &= \frac{x_2\sqrt{s}}{2}(1,-1,0,0)\\
k_1^\mu &= E_1(1,c_\theta,s_\theta c_\phi,s_\theta s_\phi)\\
k_2^\mu &= ((x_1+x_2)\frac{\sqrt{s}}{2}-E_1,(x_1-x_2)\frac{\sqrt{s}}{2}-E_1c_\theta,-E_1s_\theta c_\phi,-E_1s_\theta s_\phi)\,, \qquad (2.31)
\end{aligned}$$

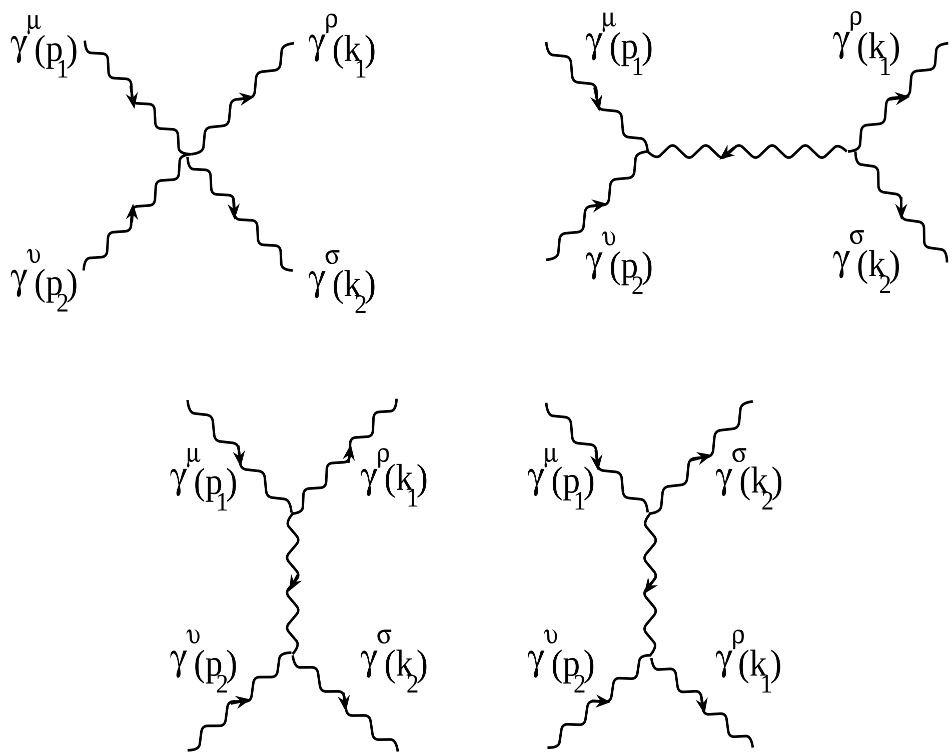

Figure 2.19: The tree level contributions to $\gamma\gamma \to \gamma\gamma$ in NCQED.

where E_1 is given by

$$E_1 = \frac{x_1 x_2 \sqrt{s}}{x_1 + x_2 - (x_1 - x_2)\cos\theta} \,. \tag{2.32}$$

Note that the Mandelstam invariants appearing in the amplitudes are now those for the photon-photon center of mass frame, with, *e.g.*, $\sqrt{\hat{s}} = x_1 x_2 \sqrt{s}$.

We define the observable amplitudes by summing over the helicities of the outgoing photons:

$$\begin{aligned} |\mathcal{M}_{++}|^2 &= \sum_{ij} |\mathcal{M}_{++ij}|^2 \,, \\ |\mathcal{M}_{+-}|^2 &= \sum_{ij} |\mathcal{M}_{+-ij}|^2 \,, \end{aligned} \tag{2.33}$$

which also include the SM contributions. The lab frame differential cross section for this process is

$$\begin{aligned} \frac{d\sigma}{d\Omega} &= \frac{1}{128\pi^2 s} \int\int dx_1\, dx_2\, \frac{E_1}{E_2}\, \frac{f(x_1) f(x_2)}{x_1 x_2} \left[\left(\frac{1 + \xi(x_1)\xi(x_2)}{2} \right) |M_{++}|^2 \right. \\ &\quad \left. + \left(\frac{1 - \xi(x_1)\xi(x_2)}{2} \right) |M_{+-}|^2 \right] , \end{aligned} \tag{2.34}$$

where E_1, E_2 denote the outgoing photon energies, $f(x)$ is the photon number density function, and $\xi(x)$ the helicity distribution function, which is presented in the appendix. The distribution functions depend upon the variable set $(P_{e1},\, P_{l1},\, P_{e2},\, P_{l2})$, which represent the polarizations of the initial fermion and laser beams. In this chapter we set $|P_e| = 0.9$ and $|P_l| = 1.0$, leaving six independent combinations: $(+,+,+,+)$, $(+,+,+,-)$, $(+,+,-,-)$, $(+,-,+,-)$, $(-,+,+,-)$, and, finally, $(+,-,-,-)$, where, for example, $(+,-,+,-)$ means $P_{e1} = 0.9$, $P_{l1} = -1.0$, $P_{e2} = 0.9$, and $P_{l2} = -1.0$. We use the approximate SM amplitudes found in [93, 94], valid for $m_W^2/x_p < 1$, where x_p represents any of the photonic Mandelstam invariants. To validate this approximation we employ the cuts

$$|\cos(\theta)| \,\leq\, 0.8 \,, \qquad \sqrt{0.4} \,<\, x_i \,<\, x_{max} \,. \tag{2.35}$$

x_{max} is the maximum fraction of the fermion beam energy that a backscattered photon can carry away; numerically, $x_{max} \approx 0.83$. Evaluating the wedge products in the NC amplitudes in the lab frame yields

$$
\begin{aligned}
p_1 \wedge p_2 &= \frac{-c_{01} x_1 x_2 s}{2\Lambda_{NC}^2} \\
p_1 \wedge k_1 &= \frac{-x_1 E_1 \sqrt{s}}{2\Lambda_{NC}^2} \Big[c_{01}\,(1 - c_\theta) - c_{02} s_\theta c_\phi - c_{03} s_\theta s_\phi - c_{12} s_\theta c_\phi + c_{31} s_\theta s_\phi \Big] \\
p_2 \wedge k_1 &= \frac{x_2 E_1 \sqrt{s}}{2\Lambda_{NC}^2} \Big[c_{01}\,(1 + c_\theta) + c_{02} s_\theta c_\phi + c_{03} s_\theta s_\phi - c_{12} s_\theta c_\phi + c_{31} s_\theta s_\phi \Big] \\
p_1 \wedge k_2 &= \frac{-x_1 E_1 \sqrt{s}}{2\Lambda_{NC}^2} \Big[\frac{c_{01} x_2 \sqrt{s}}{E_1} - c_{01}(1 - c_\theta) + c_{02} s_\theta c_\phi + \\
&\quad c_{03} s_\theta s_\phi + c_{12} s_\theta c_\phi - c_{31} s_\theta s_\phi \Big] \\
p_2 \wedge k_2 &= \frac{-x_2 E_1 \sqrt{s}}{2\Lambda_{NC}^2} \Big[\frac{-c_{01} x_1 \sqrt{s}}{E_1} + c_{01}(1 + c_\theta) + c_{02} s_\theta c_\phi + \\
&\quad c_{03} s_\theta s_\phi - c_{12} s_\theta c_\phi + c_{31} s_\theta s_\phi \Big] \\
k_1 \wedge k_2 &= \frac{-E_1 \sqrt{s}}{2\Lambda_{NC}^2} \Big[(x_1 + x_2)\{c_{02} s_\theta c_\phi + c_{03} s_\theta s_\phi + c_{01} c_\theta\} \\
&\quad -(x_1 - x_2)\{c_{01} - c_{12} s_\theta c_\phi + c_{31} s_\theta s_\phi\} \Big],
\end{aligned} \tag{2.36}
$$

where, as before, we can interpret the $c_{\mu\nu}$ in terms of the directions of the background E and B fields, with, the z-axis has being defined to be along the direction of the initial beams. Note that in this case, however, we have defined p_1 to be in the positive z-direction. Two important properties of these expressions are that the presence of both c_{0i} and c_{ij} indicates that $\gamma\gamma \to \gamma\gamma$ is sensitive to *both* space-time and space-space non-commutativity, unlike the previously examined processes, and the disappearance of c_{23} indicates that **B** fields parallel to the beam axis are unobservable as in the case of Møller scattering. We consider three different possibilities: (*i*) $c_{01} = 1$, with all others vanishing; (*ii*) $c_{03} = 1$, with all others vanishing; and (*iii*) $c_{12} = -1$, with all others vanishing. In terms of the angular parameterization, case (*i*) corresponds to an **E** field parallel to the beam axis (denoted by $\alpha = 0$ in our discussion of $e^+e^- \to \gamma\gamma$), case (*ii*) to an **E** field perpendicular to the beam axis ($\alpha = \pi/2$ in $e^+e^- \to \gamma\gamma$), and case (*iii*) to a **B** field perpendicular to the beam axis. As noted earlier for $e^+e^- \to \gamma\gamma$, c_{02} and c_{03} are equivalent up to a redefinition of ϕ, as are c_{12} and c_{31}. Note, however, that despite their apparent similarity, the space-time and space-space components are *not* equivalent up to a redefinition of ϕ. Redefining ϕ in an attempt to relate c_{03} and c_{12} inflicts a sign change in the amplitudes, which affects the interference between the SM and NC amplitudes.

In Figs. 2.20, 2.21, and 2.22 we display the bin-integrated angular distributions assuming a 500 GeV e^+e^- linear collider with an integrated luminosity of $500\,\mathrm{fb}^{-1}$ and employing the cuts discussed above. We also take $\Lambda_{NC} = \sqrt{s}$ for purposes of demonstration. As can be seen from the figures, the effects of NC space-time yield marked increases in both the z and ϕ distributions over the SM expectations, whereas this process is seen to be rather insensitive to space-space non-commutativity. The NC space-space corrections also do not strictly increase the SM result, unlike the other two cases, due to an interference effect between the SM and space-space NC contributions, and from the small magnitude of the NC effect in this case.

Figure 2.23 displays the 95% CL search reach for the NC scale Λ_{NC} as a function of luminosity for the three cases with the polarization state $(+,-,+,-)$ as well as for the case c_{01} with all polarization configurations. As expected, $\gamma\gamma$ scattering is relatively insensitive to space-space non-commutativity yielding bounds that are essentially just below $\sqrt{s}$. However, in the case of space-time NC, we see that the potential limits are comparable to that obtainable from pair annihilation and are of order $1.5\sqrt{s}$. 2 photon scattering also nicely complements $e^+e^- \to \gamma\gamma$ as one is sensitive to c_{01} with the other depending on c_{02} and c_{03}.

2.6 Summary

In summary, we have examined the testable nature of non-commutative quantum field theory by analyzing various $2 \to 2$ processes at high energy e^+e^- linear colliders. We have parameterized the non-commutative relationship in terms of an overall NC scale, Λ_{NC}, and an anti-symmetric matrix $c_{\mu\nu}$ which is related to the direction of the background electromagnetic field present in these theories. We have seen that these theories give rise to modifications to QED, resulting in a non-abelian like nature with 3- and 4-point photon self-couplings, as well as momentum dependent phase factors

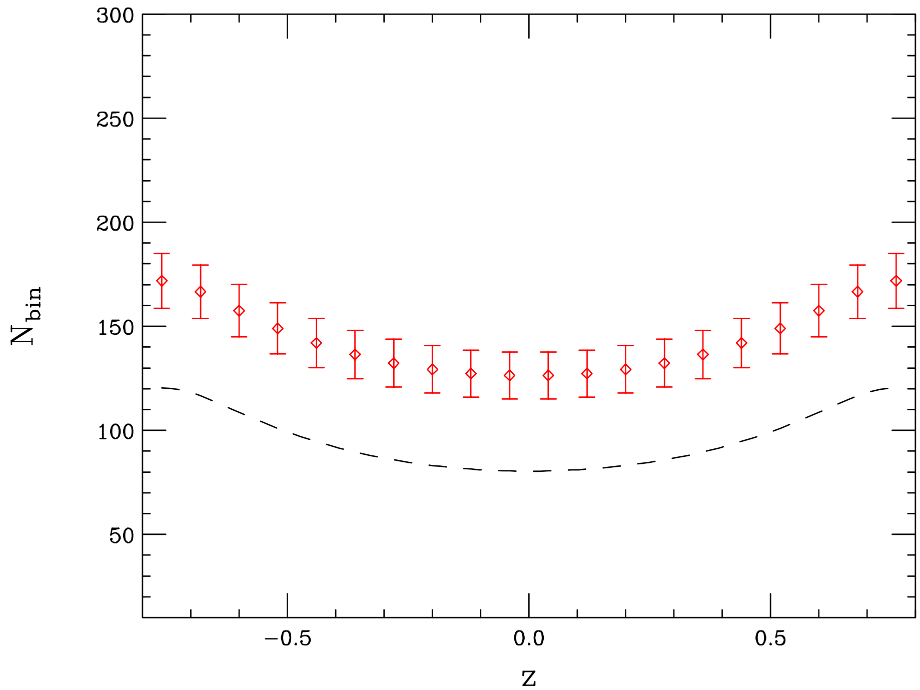

Figure 2.20: Angular dependence of the $\gamma\gamma \to \gamma\gamma$ cross section for the case $c_{01} = 1$. We take $\Lambda_{NC} = \sqrt{s} = 500$ GeV, and a luminosity of $500\,\mathrm{fb}^{-1}$ and employ the cuts discussed in the text.

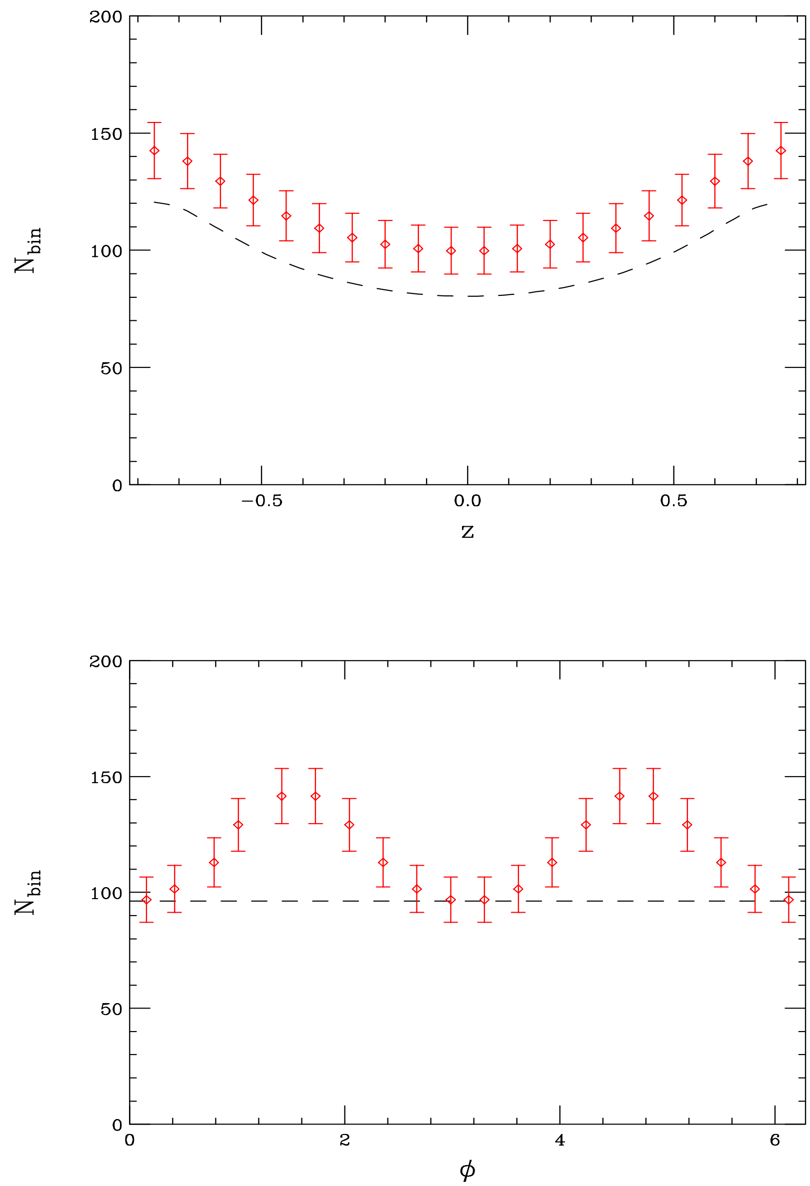

Figure 2.21: θ (top) and ϕ dependence (bottom) of the $\gamma\gamma \to \gamma\gamma$ cross section for the case $c_{03} = 1$. We again take $\Lambda_{NC} = \sqrt{s} = 500$ GeV, with a luminosity of $500\,\mathrm{fb}^{-1}$.

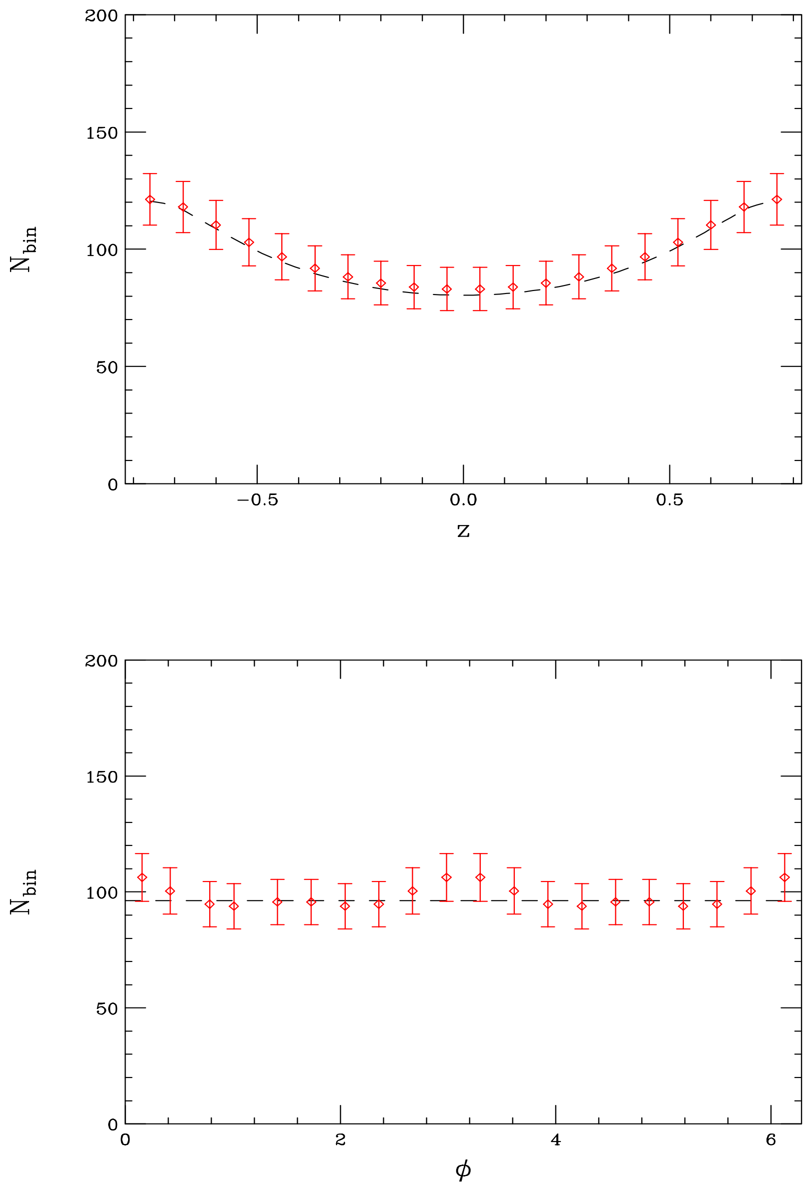

Figure 2.22: Same as the previous figure, only for $c_{12} = -1$.

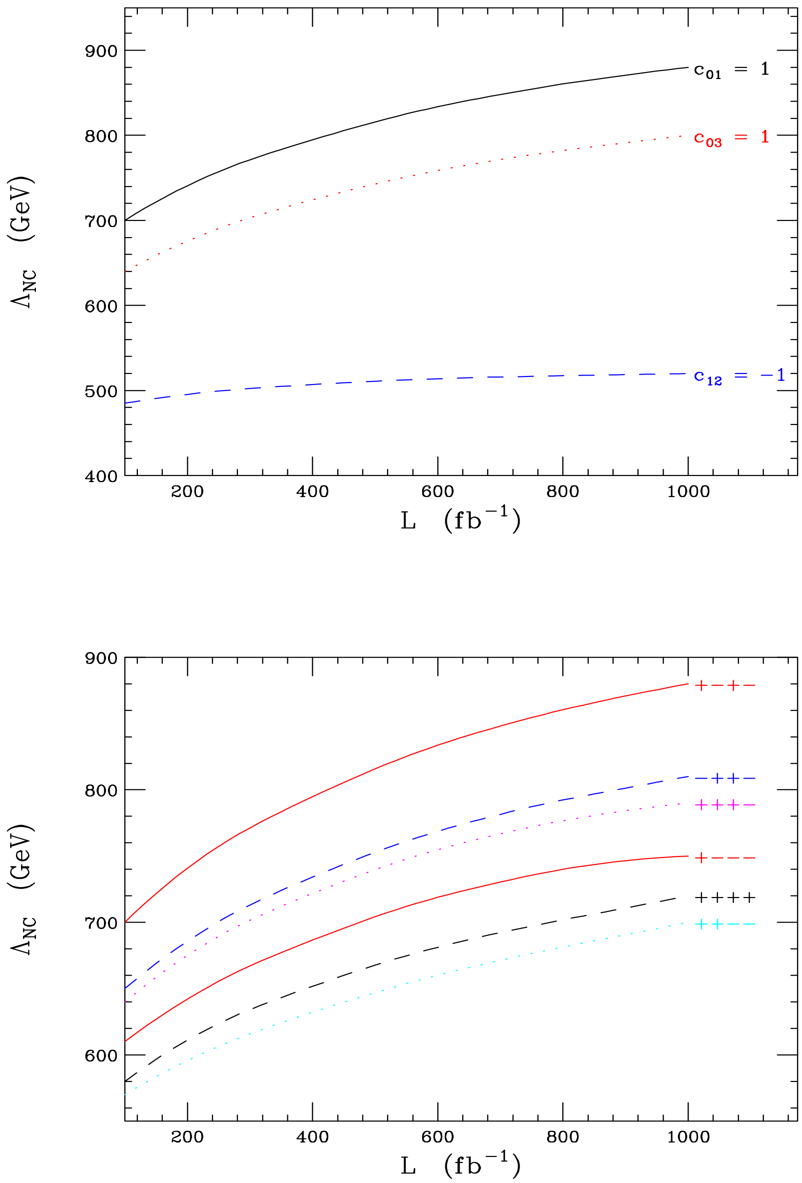

Figure 2.23: 95% CL bound on Λ_{NC} from $\gamma\gamma \to \gamma\gamma$ as a function of luminosity for $\sqrt{s} = 500$ GeV. Top panel: the three cases of $c_{\mu\nu}$ discussed in the text with the polarization state $(+,-,+,-)$, and bottom panel: all polarization states with $c_{01} = 1$.

Process	Structure Probed	Bound on Λ_{NC}
$e^+e^- \to \gamma\gamma$	Space-Time	$740 - 840$ GeV
Møller Scattering	Space-Space	1700 GeV
Bhabha Scattering	Space-Time	1050 GeV
$\gamma\gamma \to \gamma\gamma$	Space-Time	$700 - 800$ GeV
	Space-Space	500 GeV

Table 2.1: Summary of the 95% CL search limits on the NC scale Λ_{NC} from the various processes considered above at a 500 GeV e^+e^- linear collider with an integrated luminosity of 500 fb^{-1}.

appearing at each possible vertex in NCQED. We have seen that both Bhabha and Møller scattering are affected by the interference momentum dependent phase factors, whereas pair annihilation also receives contributions from the 3-point function. We have also examined $\gamma\gamma \to \gamma\gamma$, which is sensitive to both the 3- and 4-photon self-couplings.

In all the processes considered in the text, the NC affects arise at lowest order from dimension-8 operators. In addition, they generate an azimuthal dependence, which is not present in the SM, due to the NC preferred direction in space-time. These effects are not Lorentz invariant, and caution must be exercised in evaluating them, both theoretically and experimentally.

The above four processes are complementary in terms of probing the NC parameter space. Pair annihilation and Bhabha scattering, together, explore the full parameter space for Space-Time non-commutativity, whereas Møller scattering is sensitive to 2 of the parameters in the case of Space-Space NC. Two photon scattering simultaneously probes Space-Space and Space-Time NC, but is found to be rather insensitive numerically to the Space-Space case. In all of these transitions, the effects of **B** fields parallel to the beam axis are unobservable. We summarize our results for the 95% CL search reach for the NC scale in Table 2.1. We see that NCQED can be probed to scales of order a TeV, which is where one would expect NCQFT to become important, if stringy effects or if the fundamental Planck scale are also at the TeV scale.

Chapter 3

The Higgs Mechanism in Non-commutative Gauge Theories

3.1 Introduction

We studied the experimental consequences of a non-commutative modification of QED in the previous chapter. It is of course desirable to construct a full, renormalizable non-commutative Standard Model, and study its phenomenology. In this chapter we take a first step towards this goal and study the Higgs mechanism in non-commutative gauge theories.

A hallmark of non-commutative theories is the mixing of UV and IR divergences [134]; UV divergences in the commutative theory can become IR divergences in the noncommutative theory. This calls into question the renormalizability of non-commutative field theories. Several papers have explicitly shown that such theories as ϕ^4 and U(N) gauge theories, when formulated on a non-commutative space, are one loop renormalizable [19, 20, 26, 102, 128]. However, results in the literature [40] have shown that non-commutativity renders impossible the continuum renormalization of the spontaneously broken linear sigma model. They find that Goldstone's theorem is violated at the one loop level, and the Goldstone mode obtains a mass dependent upon the theory's UV cutoff. The situation in spontaneously broken gauge theories seems to also merit investigation, as both an interesting question and as a preface to any attempts to embed the Standard Model within a non-commutative framework. In particular, the gauge dependence of the spontaneously broken theory should be checked, as the analog of the problem seen in [40] would be a gauge dependent shift of one of the masses in the theory. In this chapter we examine the non-commutative Abelian Higgs model at the one-loop level. We work in an arbitrary R_ξ gauge, and show that the resulting BRST invariance of the action holds when one loop corrections are calculated by finding a counterterm set capable of removing the divergences from the 1PI functions. We find that the physical couplings and masses are gauge-independent. Upon taking the gauge coupling to zero, we obtain a continuum renormalization of the broken O(2) linear sigma model. We show that the proper ordering of the NC generalization of $|\phi|^4$ term in the globally symmetric theory is that consistent with the local realization of the symmetry. We then summarize some of the properties of the theory, such as the beta functions for the various couplings and violations of the discrete symmetries P, C, and T for certain types of non-commutativity.

This chapter is organized as follows. In Section 2 we review the commutative Abelian Higgs model, concentrating upon setting up the counterterm structure and upon defining gauge independent physical parameters. We discuss this in detail as similar definitions will be used when discussing the NC model. In Section 3 we construct the NC Abelian Higgs model, and show by explicit calculation that the theory is renormalizable. We summarize our results in Section 4.

3.2 Commutative Abelian Higgs Model

Here we review the commutative Abelian Higgs model in some detail, as much of our construction will carry over into the non-commutative case. The commutative Abelian Higgs model begins with the Lagrangian

$$\mathcal{L}_{AH} = \frac{-1}{4}(F_{\mu\nu})^2 + |\partial_\mu + igA_\mu|^2 + \mu^2 |\phi|^2 - \frac{\lambda}{6} |\phi|^4 , \tag{3.1}$$

where $F_{\mu\nu} = \partial_\mu A_\nu - \partial_\nu A_\mu$. This Lagrangian is invariant under the gauge transformation

$$\phi \to e^{ie\alpha(x)}\phi,$$

$$A_\mu \to A_\mu - \partial_\mu \alpha. \tag{3.2}$$

The potential

$$V[\phi] = \mu^2 |\phi|^2 - \frac{\lambda}{6} |\phi|^4$$

has minima at

$$|\phi_{min}|^2 = \nu^2 = \frac{3\mu^2}{\lambda}. \tag{3.3}$$

Expanding

$$\phi = \nu + \frac{h}{\sqrt{2}} + \frac{i\sigma}{\sqrt{2}}, \tag{3.4}$$

we arrive at the Lagrangian

$$\begin{aligned}\mathcal{L}_{AH} \quad = \quad & \frac{-1}{4}(F_{\mu\nu})^2 + \frac{1}{2}M^2A^2 + \frac{1}{2}(\partial_\mu\sigma)^2 + \frac{1}{2}(\partial_\mu h)^2 - \frac{1}{2}m^2h^2 \\ & + MA^\mu\partial_\mu\sigma - \frac{\sqrt{2}\lambda\nu}{6}h^3 - \frac{\sqrt{2}\lambda\nu}{6}h\sigma^2 - \frac{\lambda}{12}h^2\sigma^2 - \frac{\lambda}{24}h^4 \\ & - \frac{\lambda}{24}\sigma^4 + \frac{g^2}{2}\sigma^2A^2 + \frac{g^2}{2}h^2A^2 + ghA^\mu\partial_\mu\sigma - g\sigma A^\mu\partial_\mu h \\ & + \sqrt{2}g^2\nu hA^2. \end{aligned} \tag{3.5}$$

The Higgs field has acquired a mass $m^2 = 2\lambda\nu^2/3$, while the gauge boson has acquired a mass $M^2 = 2g^2\nu^2$. We will work in an R_ξ gauge, so to this we add the gauge fixing and ghost Lagrangians

$$\mathcal{L}_{gf} + \mathcal{L}_{gh} = \frac{-1}{2\xi}(\partial_\mu A^\mu - \xi M\sigma)^2 - \bar{c}\left(\partial^2 + \xi M^2 + \xi gMh\right)c, \tag{3.6}$$

which cancels the $A - \sigma$ cross term. The Feynman rules can be found in [14]. The total Lagrangian $\mathcal{L}_{AH} + \mathcal{L}_{gf} + \mathcal{L}_{gh}$ is invariant under the BRST transformation

$$\begin{aligned}\delta h \quad &= \quad -g\sigma c\,\Theta \\ \delta\sigma \quad &= \quad Mc\,\Theta + ghc\,\Theta \\ \delta A_\mu \quad &= \quad -(\partial_\mu c)\,\Theta \\ \delta\bar{c} \quad &= \quad -\frac{1}{\xi}(\partial_\mu A^\mu - \xi M\sigma)\,\Theta \\ \delta c \quad &= \quad 0\,. \end{aligned} \tag{3.7}$$

To study the renormalizability of the theory we define the following counterterms relating the bare and physical quantities:

$$\begin{aligned} A_B^\mu = Z_A^{1/2} A^\mu, \quad \phi_B = Z_\phi^{1/2}\phi, \quad \mu_B^2 = Z_\phi^{-1} Z_\mu \mu^2, \\ \lambda_B = Z_\phi^{-2} Z_\lambda \lambda m_D^{4-d}, \quad g_B = Z_A^{-1/2} Z_g g m_D^{2-d/2}, \end{aligned} \tag{3.8}$$

where m_D is a constant with dimensions of mass used to account for units in dimensional regularization. Note that if we expand

$$\phi = \nu + \frac{h}{\sqrt{2}} + \frac{i\sigma}{\sqrt{2}}, \qquad \nu^2 = \frac{3\mu^2}{\lambda}$$

as before, we will no longer be expanding around the minimum of the potential; the higgs tadpole will acquire a nonzero value. It is convenient, though unnecessary, to introduce a new counterterm Z_ν, expand

$$\phi = Z_\nu \nu + \frac{h}{\sqrt{2}} + \frac{i\sigma}{\sqrt{2}}, \tag{3.9}$$

and fix Z_ν by requiring the higgs tadpole to vanish. We could, if desired, refrain from introducing Z_ν, and include the Higgs tadpole in the calculation of other Green's functions. Depending upon the gauge in which we work, Z_ν will be UV divergent. Although it may seem strange to be expanding the scalar field around an infinite gauge-dependent vev, the expansion point is not a physical obervable, so no contradiction arises. This procedure is discussed in [56]. We now take the Lagrangian in Eq. 3.1, written in terms of bare quantities, and insert the physical quantities and counterterms, while expanding the field ϕ as in Eq. 3.9. Our new Lagrangian contains two pieces: the Lagrangian of Eq. 3.5 written in terms of the physical parameters, and the counterterm Lagrangian, which is used to subtract the divergences in the physical Green's functions. The counterterm Lagrangian generated from the original Lagrangian plus $\mathcal{L}_{gf}$ is

$$\begin{aligned} \mathcal{L}_{AH+gf}^{cnt} &= \frac{1}{\sqrt{2}}\nu m^2 \left(Z_\nu Z_\mu - Z_\nu^3 Z_\lambda\right) h - \frac{1}{2} m^2 \left(\frac{3}{2} Z_\nu^2 Z_\lambda - \frac{1}{2} Z_\mu - 1\right) h^2 \\ &\quad - \frac{1}{4} m^2 \left(Z_\nu^2 Z_\lambda - Z_\mu\right)\sigma^2 + \frac{1}{2}\left(Z_\phi - 1\right)\left(\partial_\mu h\right)^2 + \frac{1}{2}\left(Z_\phi - 1\right)\left(\partial_\mu \sigma\right)^2 \end{aligned}$$

$$
\begin{aligned}
&-\frac{1}{24}\left(Z_\lambda-1\right)\lambda h^4-\frac{1}{24}\left(Z_\lambda-1\right)\lambda\sigma^4-\frac{1}{12}\left(Z_\lambda-1\right)\lambda h^2\sigma^2\\
&-\frac{\sqrt{2}}{6}\left(Z_\nu Z_\lambda-1\right)\lambda\nu h^3-\frac{\sqrt{2}}{6}\left(Z_\nu Z_\lambda-1\right)\lambda\nu h\sigma^2\\
&-\frac{Z_A}{4}\left(F_{\mu\nu}\right)^2+\sqrt{2}\left(Z_g Z_\phi Z_\nu-1\right)g\nu A^\mu\partial_\mu\sigma+\left(Z_\phi Z_g^2 Z_\nu^2-1\right)g^2\nu^2A^2\\
&+\left(Z_\phi Z_\nu Z_g^2-1\right)g^2\nu hA^2+\frac{1}{2}\left(Z_\phi Z_g^2-1\right)g^2\sigma^2A^2\\
&+\frac{1}{2}\left(Z_\phi Z_g^2-1\right)g^2h^2A^2+\left(Z_\phi Z_g-1\right)gA^\mu\left[h\partial_\mu\sigma-\sigma\partial_\mu h\right]\ . \qquad (3.10)
\end{aligned}
$$

This expression uses the fact that $\mathcal{L}_{gf}$ is already written in terms of the physical parameters and fields. To determine the counterterms for $\mathcal{L}_{gh}$, we first note that the Higgs-ghost interaction is super-renormalizable, and therefore doesn't need a counterterm. Returning to the gauge transformation of Eq. 3.2 written in terms of the unbroken fields, and expanding as in Eq. 3.9, we arrive at the counterterm Lagrangian

$$\mathcal{L}_{gh}^{cnt}=-\left(Z_\nu-1\right)\xi M^2\bar{c}c. \qquad (3.11)$$

The super-renormalizability of the Higgs-ghost interaction means that we do not need to introduce a wave-function renormalization constant for the ghost field. The new Lagrangian is invariant under a "renormalized" BRST symmetry, which is identical to Eq. 3.7 with $M\to Z_\nu M$ in the $\delta\sigma$ transformation.

The terms listed above illustrate the subtlety involved with the renormalization of spontaneously broken theories; a limited number of counterterms are needed to subtract a large number of divergences. The above theory is renormalizable in spite of these difficulties. An explicit one loop calculation reveals the counterterms

$$
\begin{aligned}
Z_g=1,\ Z_A=1-\frac{g^2}{24\pi^2\epsilon},\quad Z_\phi=1+\frac{3g^2}{8\pi^2\epsilon}-\frac{\xi g^2}{8\pi^2\epsilon},\quad Z_\nu=1+\frac{\xi g^2}{8\pi^2\epsilon},\\
Z_\lambda=1+\frac{5\lambda}{24\pi^2\epsilon}+\frac{9g^4}{4\pi^2\lambda\epsilon}-\frac{\xi g^2}{4\pi^2\epsilon},\quad Z_\mu=1+\frac{\lambda}{12\pi^2\epsilon}-\frac{\xi g^2}{8\pi^2\epsilon}, \qquad (3.12)
\end{aligned}
$$

where $\epsilon=4-d$ can account for the one loop divergences in this theory, and we have used the minimal subtraction prescription.

In preparation for our discussion of the NC case, let us discuss how to obtain gauge-independent couplings and masses. Eq. 3.8 gives the relations between the bare couplings and physical couplings; solving the equations for the physical couplings in terms of the bare couplings and renormalization constants, and inserting the expressions of Eq. 3.12 for the renormalization constants, gives ξ independent expressions for the physical couplings. The calculation of the physical couplings at various renormalization points is facilitated by finding their beta functions. We find the following values:

$$\begin{aligned}\beta(\lambda) &= m_D \frac{\partial \lambda}{\partial m_D} = \frac{5\lambda^2}{24\pi^2} - \frac{3\lambda g^2}{4\pi^2} + \frac{9g^4}{4\pi^2} \\ \beta(g^2) &= m_D \frac{\partial g^2}{\partial m_D} = \frac{g^4}{24\pi^2}.\end{aligned} \tag{3.13}$$

These quantities are in agreement with those found in [55]. We can solve these differential equations to find the relations between physical couplings at various renormalization points; for example, we find

$$g^2 = \frac{g_0^2}{1 - \frac{g_0^2}{24\pi^2} \ln\left(\frac{m_D}{m_{D0}}\right)}, \tag{3.14}$$

where g_0 is the coupling at the renormalization point m_{D0}. Similarly for the masses, we have the following relations between bare and physical masses:

$$\begin{aligned} m_B^2 &= \frac{2}{3}\lambda_B \nu_B^2 = Z_\mu Z_\phi^{-1}\, m^2 \\ M_B^2 &= 2g_B^2 \nu_B^2 = Z_g^2 Z_A^{-1} Z_\mu Z_\phi Z_\lambda^{-1}\, M^2 \end{aligned} \tag{3.15}$$

Note that $\nu_B = 3\mu_B^2/\lambda_B$; Z_ν just defines the shift of the expansion point, and does not enter this expression. We can check that these lead to gauge independent definitions of the physical masses; calculation yields

$$\begin{aligned} m^2 &= m_B^2 \left[1 - \frac{\lambda}{12\pi^2\epsilon} + \frac{3g^2}{8\pi^2\epsilon}\right] \\ M^2 &= M_B^2 \left[1 + \frac{\lambda}{8\pi^2\epsilon} - \frac{5g^2}{12\pi^2\epsilon} + \frac{9g^4}{4\pi^2\lambda\epsilon}\right], \end{aligned} \tag{3.16}$$

where the bare masses are infinite in order to cancel the $1/\epsilon$ poles. The important point is the gauge independence of these results; we will find that the same definitions of the physical parameters give gauge independent results in the NC theory.

3.3 Non-commutative Abelian Higgs Model

3.3.1 Setup of NC Symmetry Breaking in U(1)

We now examine the non-commutative extension of the Abelian Higgs model, following the procedure introduced in the previous section. Non-commutative U(1) gauge theory coupled to a complex scalar field is defined by the Lagrangian

$$\mathcal{L}_{AH} = \frac{-1}{4} F_{\mu\nu} \times F^{\mu\nu} + D_\mu\phi \times (D^\mu\phi)^* + \mu^2 |\phi|^2 - \frac{\lambda}{6}\phi^* \times \phi \times \phi^* \times \phi, \qquad (3.17)$$

where $D_\mu\phi = \partial_\mu\phi + igA_\mu \times \phi$ and $F_{\mu\nu} = \partial_\mu A_\nu - \partial_\nu A_\mu + ig\left(A_\mu \times A_\nu - A_\nu \times A_\mu\right)$. With $U(x) = e^{ig\alpha(x)}$, the action is invariant under the gauge transformation

$$\phi \to U \times \phi,\ \phi^* \to \phi^* \times U^{-1},\ A_\mu \to U \times A_\mu \times U^{-1} + \frac{i}{g}(\partial_\mu U) \times U^{-1}. \qquad (3.18)$$

Note that of the two possible noncommutative generalizations of $|\phi|^4$, $\phi^* \times \phi \times \phi^* \times \phi$ and $\phi^* \times \phi^* \times \phi \times \phi$, only the first is consistent with local gauge invariance as defined by the transformation of Eq. 3.18. We examined the theory with the potential $f\,\phi^* \times \phi \times \phi^* \times \phi + (1-f)\,\phi^* \times \phi^* \times \phi \times \phi$ and found that the theory is one-loop renormalizable only if $f = 1$. The minimum of the potential $V[\phi]$ is the same as in the commutative theory, and as quadratic forms are unchanged by the noncommutativity, the Higgs particle and gauge boson acquire the same masses as in the commutative theory. Expanding around the minimum ν, we arrive at the Lagrangian

$$\begin{aligned}
\mathcal{L}_{AH} \;=\; & \frac{-1}{4} F_{\mu\nu} \times F^{\mu\nu} + \frac{1}{2}(\partial_\mu h)^2 + \frac{1}{2}(\partial_\mu \sigma)^2 - M\sigma\partial_\mu A^\mu + \frac{1}{2}M^2 A^2 \\
& -\frac{1}{2}m^2 h^2 - \frac{\sqrt{2}\nu}{6} h \times h \times h - \frac{\sqrt{2}\nu}{6} h \times \sigma \times \sigma \\
& -\frac{\lambda}{24} h \times h \times h \times h - \frac{\lambda}{24}\sigma \times \sigma \times \sigma \times \sigma - \frac{\lambda}{6} h \times h \times \sigma \times \sigma \\
& +\frac{\lambda}{12} h \times \sigma \times h \times \sigma + gMh \times A_\mu \times A^\mu + \frac{1}{2}g^2 h \times h \times A_\mu \times A^\mu \\
& +\frac{1}{2}g^2 \sigma \times \sigma \times A_\mu \times A^\mu + \frac{i}{2}g^2[h,\sigma] \times A_\mu \times A^\mu + \frac{i}{2}gA_\mu \times [h, \partial^\mu h]
\end{aligned}$$

$$+\frac{i}{2}gA_\mu \times [\sigma, \partial^\mu \sigma] + \frac{1}{2}gA_\mu \times \{h, \partial^\mu \sigma\} - \frac{1}{2}gA_\mu \times \{\sigma, \partial^\mu h\}\,, \qquad (3.19)$$

where we have used the notation $[x, y] = x \times y - y \times x$ and $\{x, y\} = x \times y + y \times x$. To this we add the gauge-fixing and ghost Lagrangians

$$\begin{aligned} \mathcal{L}_{gf} + \mathcal{L}_{gh} &= -\frac{1}{2\xi}(\partial_\mu A^\mu - \xi M\sigma)^2 - \bar{c}\left(\partial^2 + \xi M^2\right)c - \frac{\xi g M}{2}\bar{c}\,\{c, h\} \\ &\quad -\frac{i\xi g M}{2}\bar{c}\,[c, \sigma] + ig\bar{c}\partial^\mu\,[c, A_\mu]\ ; \end{aligned} \qquad (3.20)$$

to obtain the ghost Lagrangian we simply insert the BRST transformation of Eq. 3.21 into the gauge- fixing condition

$$F[A, \sigma] = \partial_\mu A^\mu - \xi M\sigma\ .$$

The full Lagrangian $\mathcal{L}_{AH} + \mathcal{L}_{gf} + \mathcal{L}_{gh}$ is found to be invariant under the BRST transformation

$$\begin{aligned} \delta h &= -\frac{g}{2}\{c, \sigma\}\Theta + \frac{ig}{2}[c, h]\Theta \\ \delta\sigma &= Mc\,\Theta + \frac{g}{2}\{c, h\}\Theta + \frac{ig}{2}[c, \sigma]\Theta \\ \delta A_\mu &= -(\partial_\mu c)\Theta + ig\,[c, A_\mu]\Theta \\ \delta\bar{c} &= -\frac{1}{\xi}(\partial_\mu A^\mu - \xi M\sigma)\Theta \\ \delta c &= -igc \times c\,\Theta. \end{aligned} \qquad (3.21)$$

Note that upon replacing $c\,\Theta \to \alpha$ in the transformation laws for h, σ, and A_μ, the above reduce to the infinitesimal transformations found in Eq. 3.18. Let us carefully show how to obtain the transformations of h and σ. The infinitesimal form of Eq. 3.18 is

$$\begin{aligned} \phi &\to \phi' = \phi + ig\,\alpha \times \phi \\ \phi^* &\to \phi^{*\prime} = \phi^* - ig\,\phi^* \times \alpha, \end{aligned} \qquad (3.22)$$

where the prime indicates the transformed field. Written in terms of h and σ, these become

$$\begin{aligned}
\nu + \frac{1}{\sqrt{2}}\left(h' + i\sigma'\right) &= \nu + \frac{1}{\sqrt{2}}(h + i\sigma) + ig\nu\alpha + \frac{ig}{\sqrt{2}}\alpha \times (h + i\sigma) \\
\nu + \frac{1}{\sqrt{2}}\left(h' - i\sigma'\right) &= \nu + \frac{1}{\sqrt{2}}(h - i\sigma) - ig\nu\alpha - \frac{ig}{\sqrt{2}}(h - i\sigma) \times \alpha. \quad (3.23)
\end{aligned}$$

Adding and subtracting these give the transformations of h and σ, respectively.

Given the Lagrangians of Eqs. 3.19, 3.20, we can derive the Feynman rules for this theory. New interactions appear, such as $A - 2h$ and $2A - h - \sigma$ vertices, which arise from commutators that vanish in the commutative limit. These occur because of the violation of charge conjugation symmetry, as will be shown in the next several paragraphs.

Let us now briefly discuss the role of the discrete symmetries P, C, and T in this theory; the presentation will very closely follow that in [159]. The transformations of the fields under the various symmetries can be derived from the requirement that the commutative Lagrangian of Eq. 3.5 be invariant under any of the symmetries; the results are

$$\begin{aligned}
P\,h\,P^{-1} = h \qquad & C\,h\,C^{-1} = h \qquad & T\,h\,T^{-1} = h \\
P\,\sigma\,P^{-1} = -\sigma \qquad & C\,\sigma\,C^{-1} = -\sigma \qquad & T\,\sigma\,T^{-1} = -\sigma \\
P\,A^{\mu}\,P^{-1} = A_{\mu} \qquad & C\,A_{\mu}\,C^{-1} = -A_{\mu} \qquad & T\,A^{\mu}\,T^{-1} = A_{\mu}. \quad (3.24)
\end{aligned}$$

We must now determine whether the interactions introduced by the non-commutativity respect these symmetries. Although the matrix $\theta_{\mu\nu}$ is just a set of real parameters and is not affected by any of the transformations, it will be useful to indicate the transformations of the various θ parameters that would lead to an invariant NC Lagrangian, as in [159].

Parity: The net effect of parity on the NC Lagrangian is to change the Moyal product as follows:

$$\exp\left(\frac{i\theta_{0i}}{2}\overleftarrow{\partial_0}\overrightarrow{\partial_i} + \frac{i\theta_{ij}}{2}\overleftarrow{\partial_i}\overrightarrow{\partial_j}\right) \rightarrow \exp\left(-\frac{i\theta_{0i}}{2}\overleftarrow{\partial_0}\overrightarrow{\partial_i} + \frac{i\theta_{ij}}{2}\overleftarrow{\partial_i}\overrightarrow{\partial_j}\right). \quad (3.25)$$

Hence, the NC theory is P invariant only if $\theta_{0i} = 0$. The theory would be parity invariant if we also took $\theta_{0i} \to -\theta_{0i}$.

Charge Conjugation: Charge conjugation leaves all but four terms of the Lagrangian invariant: the terms in Eq. 3.19 containing commutators and the term leading to the triple gauge photon vertex, which also contains a single commutator. These acquire a minus sign under C. Charge conjugation invariance is therefore violated for any non-zero value of θ; the $A-2h$, $A-2\sigma$, $3A$, and $2A-h-\sigma$ vertices arising from the commutator terms in the Lagrangian explicitly show this violation. We could maintin C invariance by requiring $C\,\theta_{\mu\nu}\,C^{-1} = -\theta_{\mu\nu}$.

Time Reversal: The net effect of the time reversal invariance on the NC Lagrangian is to change the Moyal product,

$$\exp\left(\frac{i\theta_{0i}}{2}\,\overleftarrow{\partial}_0\overrightarrow{\partial}_i + \frac{i\theta_{ij}}{2}\,\overleftarrow{\partial}_i\overrightarrow{\partial}_j\right) \to \exp\left(\frac{i\theta_{0i}}{2}\,\overleftarrow{\partial}_0\overrightarrow{\partial}_i - \frac{i\theta_{ij}}{2}\,\overleftarrow{\partial}_i\overrightarrow{\partial}_j\right). \qquad (3.26)$$

The theory is time reversal invariant only if $\theta_{ij} = 0$. T invariance could be maintained by requiring $T\,\theta_{ij}\,T^{-1} = -\theta_{ij}$.

We can see from these transformations that the theory is CPT invariant for all $\theta_{\mu\nu}$, and CP invariant only if $\theta_{ij} = 0$. This leads to the question of whether theories with $\theta_{ij} \neq 0$ might be used as models of CP violation in particle physics, a point raised in [159]. We make no attempt to address this question, as it would require the non-commutative extension of the electroweak theory, but do provide a rough estimate of the size of such effects, obtained by considering the C violating process $A \to hh$. A short calculation reveals a partial width of the form

$$\Gamma \sim M\,\frac{M^4}{\Lambda^4}, \qquad (3.27)$$

where Λ is the energy scale associated with the non-commutativity. We will not attempt to study further the phenomonology of NC theories; preliminary discussions can be found in [42, 46, 53, 105, 132, 136].

To study the renormalization of the theory we introduce the same wave-function and coupling constant rescalings as in Eq. 3.8. As the ghost-gauge boson vertex contains factors of momenta, we must also introduce the ghost wave-function renormalization

$$c_B = Z_c c. \tag{3.28}$$

The counterterm Lagrangian $\mathcal{L}_{AH}^{cnt}$ obtained from Eq. 3.19 is the same as that of Eq. 3.10 with multiplication replaced by the Moyal product and the anti-commutators of Eq. 3.19 accounted for appropriately. In addition, there are new counterterms for the three and four-point gauge boson vertices, and for the new interactions represented by commutators of Eq. 3.19. As the counterterm Lagrangian is rather long we will not write it explicitly; it is apparent how to obtain it, and the counterterms for each vertex are presented in the next section. The ghost counterterm Lagrangian, $\mathcal{L}_{gh}^{cnt}$, is

$$\begin{aligned} \mathcal{L}_{gh}^{cnt} &= -\left(Z_c-1\right)\partial^2 c - \xi\left(Z_c Z_g Z_\nu - 1\right) M^2 \bar{c} c + i\left(Z_c Z_g - 1\right) g \bar{c}\, \partial^\mu \left[c, A_\mu\right] \\ &\quad -\frac{\xi g M}{2}\left(Z_c Z_g - 1\right)\bar{c}\left\{c, h\right\} - \frac{i\xi g M}{2}\left(Z_c Z_g - 1\right)\bar{c}\left\{c,\sigma\right\}. \end{aligned} \tag{3.29}$$

The entire Lagrangian, $\mathcal{L}_{gh} + \mathcal{L}_{gh}^{cnt} + \mathcal{L}_{AH} + \mathcal{L}_{AH}^{cnt} + \mathcal{L}_{gf}$, is now invariant under the renormalized BRST transformation

$$\begin{aligned} \delta_R h &= -\frac{Z_c Z_g g}{2}\left\{c,\sigma\right\}\Theta + \frac{i Z_c Z_g g}{2}\left[c, h\right]\Theta \\ \delta_R \sigma &= Z_c Z_g Z_\nu M c\,\Theta + \frac{Z_c Z_g g}{2}\left\{c, h\right\}\Theta + \frac{i Z_c Z_g g}{2}\left[c,\sigma\right]\Theta \\ \delta_R A_\mu &= -Z_c\left(\partial_\mu c\right)\Theta + i Z_c Z_g g\left[c, A_\mu\right]\Theta \\ \delta_R \bar{c} &= -\frac{1}{\xi}\left(\partial_\mu A^\mu - \xi M \sigma\right)\Theta \\ \delta_R c &= -i Z_c Z_g g c \times c\,\Theta, \end{aligned} \tag{3.30}$$

which arises from the BRST invariance of the Lagrangian written in terms of bare fields. To demonstrate that this BRST invariance holds at the one-loop level, we must find a set of renormalization constants that can simultaneously remove the divergences from every 1PI function; we do this below.

3.3.2 Calculation of NC divergences

Below we present the somewhat lengthy list of the UV divergent parts of the 1PI functions. We use dimensional regularization with $d = 4-\epsilon$, and the MS prescription. We have adopted here the notation $p \wedge q = p^\mu q^\nu \Theta_{\mu\nu}/2$. As we are interested only in the UV divergences any loop integral containing $\exp(ip \wedge k)$, where k is the loop momentum, will be ignored, as it is damped for large k when a convergence factor is included. We include the counterterms that must account for each divergence. Only the distinct vertices are listed; for example, the $4-h$ and $4-\sigma$ UV divergences, Γ^{4h} and $\Gamma^{4\sigma}$, are identical, and only Γ^{4h} is given. Similarly, the following pairs of vertices are identical: the $2A-2\sigma$ and the $2A-2h$, and the $2h-A$ and the $2\sigma-A$. We have also checked that 1PI functions for which no counterterms appear, such as Γ^{hA}, are UV finite.

$$
\begin{aligned}
\Gamma^{h} &= \frac{i\lambda\nu m^2}{8\sqrt{2}\pi^2\epsilon} + \frac{i\xi\lambda\nu M^2}{24\sqrt{2}\pi^2\epsilon} + \frac{3igM^3}{8\pi^2\epsilon} + \frac{i\nu m^2}{\sqrt{2}}\left[Z_\nu Z_\mu - Z_\nu^3 Z_\lambda\right] \\
\Gamma^{2h} &= \frac{-3ig^2p^2}{8\pi^2\epsilon} + \frac{i\xi g^2p^2}{8\pi^2\epsilon} + \frac{7i\lambda m^2}{48\pi^2\epsilon} + \frac{3ig^2M^2}{4\pi^2\epsilon} + \frac{i\xi\lambda M^2}{24\pi^2\epsilon} - \frac{i\xi g^2m^2}{16\pi^2\epsilon} \\
&\quad - im^2\left[\frac{3}{2}Z_\nu^2 Z_\lambda - \frac{1}{2}Z_\mu - 1\right] + ip^2\left(Z_\phi - 1\right) \\
\Gamma^{3h} &= \Big(\cos(p_1\wedge p_2) \,+\, \cos(p_1\wedge p_3) \,+\, \cos(p_3\wedge p_2)\Big)\left[\frac{i\nu\lambda^2}{18\sqrt{2}\pi^2\epsilon} + \frac{3ig^3M}{8\pi^2\epsilon}\right. \\
&\quad \left. -\frac{i\sqrt{2}\xi\nu\lambda g^2}{24\pi^2\epsilon} - \frac{i\sqrt{2}\nu\lambda}{3}\left(Z_\nu Z_\lambda - 1\right)\right] \\
\Gamma^{4h} &= \Big(\cos(p_1\wedge p_2)\cos(p_3\wedge p_4) \,+\, \cos(p_1\wedge p_3)\cos(p_2\wedge p_4) \\
&\quad + \cos(p_1\wedge p_4)\cos(p_3\wedge p_2)\Big) \times \left[\frac{i\lambda^2}{36\pi^2\epsilon} + \frac{3ig^4}{8\pi^2\epsilon} - \frac{i\xi\lambda g^2}{12\pi^2\epsilon}\right. \\
&\quad \left. -\frac{i\lambda(Z_\lambda - 1)}{3}\right] \\
\Gamma^{2\sigma} &= \frac{-3ig^2p^2}{8\pi^2\epsilon} + \frac{i\xi g^2p^2}{8\pi^2\epsilon} + \frac{i\lambda m^2}{16\pi^2\epsilon} + \frac{3ig^2M^2}{8\pi^2\epsilon} + \frac{i\xi g^2m^2}{16\pi^2\epsilon} \\
&\quad - \frac{im^2}{2}\left[Z_\nu^2 Z_\lambda - Z_\mu\right] + ip^2\left(Z_\phi - 1\right) \\
\Gamma^{h-2\sigma} &= \cos(p_1\wedge p_2)\left[\frac{i\lambda^2\nu\sqrt{2}}{36\pi^2\epsilon} + \frac{3ig^3M}{8\pi^2\epsilon} - \frac{i\xi\lambda g\nu\sqrt{2}}{24\pi^2\epsilon} - \frac{i\lambda\nu\sqrt{2}}{3}\left(Z_\lambda Z_\nu - 1\right)\right]
\end{aligned}
$$

$$
\begin{aligned}
\Gamma^{2h-2\sigma} &= \left(2\cos(p_1\wedge p_2)\cos(p_3\wedge p_4)-\cos(p_1\wedge p_3+p_2\wedge p_4)\right)\Bigg[\frac{i\lambda^2}{36\pi^2\epsilon} \\
&\quad +\frac{3ig^4}{8\pi^2\epsilon}-\frac{i\xi\lambda g^2}{12\pi^2\epsilon}-\frac{i\lambda}{3}\left(Z_\lambda-1\right)\Bigg] \\
\Gamma^{2h-A} &= [p_1-p_2]_\mu \sin(p_1\wedge p_2)\left[-\frac{3g^3}{16\pi^2\epsilon}\left(1-\xi\right)+g\left(Z_g Z_\phi-1\right)\right] \\
\Gamma^{2h-2A} &= \cos(p_1\wedge p_2)\cos(p_3\wedge p_4)\, g_{\mu\nu}\, \left[\frac{i\xi g^4}{2\pi^2\epsilon}+2ig^2\left(Z_\phi Z_g^2-1\right)\right] \\
\Gamma^{h-\sigma-2A} &= \cos(p_1\wedge p_2)\sin(p_3\wedge p_4)\, g_{\mu\nu}\, \left[\frac{i\xi g^4}{2\pi^2\epsilon}+2ig^2\left(Z_\phi Z_g^2-1\right)\right] \\
\Gamma^{h-\sigma-A} &= [p_1-p_2]_\mu \cos(p_1\wedge p_2)\left[-\frac{3g^3}{16\pi^2\epsilon}\left(1-\xi\right)+g\left(Z_g Z_\phi-1\right)\right] \\
\Gamma^{h-2A} &= \cos(p_1\wedge p_2)\, g_{\mu\nu}\, \left[\frac{i\xi g^3 M}{4\pi^2\epsilon}+2igM\left(Z_\phi Z_g^2 Z_\nu-1\right)\right] \\
\Gamma^{\sigma-A} &= p_\mu\, \left[-\frac{3g^2M}{16\pi^2\epsilon}+\frac{\xi g^2 M}{16\pi^2\epsilon}+M\left(Z_\phi Z_g Z_\nu-1\right)\right] \\
\Gamma^{c-\bar{c}} &= -\frac{3ig^2p^2}{16\pi^2\epsilon}+\frac{i\xi g^2p^2}{16\pi^2\epsilon}+ip^2\left(Z_c-1\right)-i\left(Z_c Z_g Z_\nu-1\right)\xi M^2 \\
\Gamma^{c-\bar{c}-A} &= p_2^\mu \sin(p_1\wedge p_2)\left[\frac{\xi g^3}{4\pi^2\epsilon}+2g\left(Z_c Z_g-1\right)\right] \\
\Gamma^{c-\bar{c}-h} &= \cos(p_1\wedge p_2)\left[-\frac{i\xi^2 g^3 M}{8\pi^2\epsilon}-i\xi gM\left(Z_c Z_g-1\right)\right] \\
\Gamma^{c-\bar{c}-\sigma} &= \sin(p_1\wedge p_2)\left[-\frac{i\xi^2 g^3 M}{8\pi^2\epsilon}-i\xi gM\left(Z_c Z_g-1\right)\right] \\
\Gamma^{2A} &= \left(g_{\mu\nu}p^2-p_\mu p_\nu\right)\left[\frac{ig^2}{2\pi^2\epsilon}-\frac{i\xi g^2}{8\pi^2\epsilon}\right]+ig_{\mu\nu}\,\left(Z_\phi Z_g^2 Z_\nu^2-1\right)M^2 \\
&\quad -i\left(Z_A-1\right)\left[g_{\mu\nu}p^2-p_\mu p_\nu\right] \\
\Gamma^{3A} &= \sin(p_1\wedge p_2)\Big\{(p_1-p_2)_\rho\, g_{\mu\nu}+(p_2-p_3)_\mu\, g_{\nu\rho}+(p_3-p_1)_\nu\, g_{\mu\rho}\Big\} \\
&\quad \times\left[-\frac{5g^3}{8\pi^2\epsilon}+\frac{3\xi g^3}{8\pi^2\epsilon}+2g\left(Z_A Z_g-1\right)\right] \\
\Gamma^{4A} &= \Big\{\sin(p_1\wedge p_2)\sin(p_3\wedge p_4)\,\left[g_{\mu\rho}g_{\nu\sigma}-g_{\mu\sigma}g_{\nu\rho}\right]+\sin(p_3\wedge p_1)\sin(p_2\wedge p_4) \\
&\quad \times\left[g_{\mu\nu}g_{\rho\sigma}-g_{\mu\rho}g_{\nu\sigma}\right]+\sin(p_1\wedge p_4)\sin(p_2\wedge p_3)\,\left[g_{\mu\sigma}g_{\nu\rho}-g_{\mu\nu}g_{\rho\sigma}\right]\Big\} \\
&\quad \times\left[\frac{ig^4}{2\pi^2\epsilon}-\frac{i\xi g^4}{\pi^2\epsilon}-4ig^2\left(Z_A Z_g^2-1\right)\right] \qquad (3.31)
\end{aligned}
$$

We remind the reader of the relations $m^2 = 2\lambda\nu^2/3$, $M^2 = 2g^2\nu^2$, and $M^2/m^2 = 3g^2/\lambda$, which are used in showing that the renormalization constants listed below can remove these divergences. We would also like to point out that our expressions for individual diagrams agree with [128] when applicable. An interesting feature of these results is that individual diagrams were not necessarily proportional to the momentum dependent phase present in the vertices. This is particularly striking in the $4A$ vertex; it contains a very non-trivial Lorentz index and phase factor structure, and receives contributions from a very large number of diagrams, none of which are proportional to the necessary factor. This point was also emphasized in [128], who found the same behavior in pure NC U(N) gauge theories in arbitrary Lorentz gauges.

There are a very limited number of renormalization constants that must account for a large number of divergences; we find, however, that the following set suffices:

$$\begin{aligned}
Z_\lambda &= 1 + \frac{\lambda}{12\pi^2\epsilon} + \frac{9g^4}{8\pi^2\lambda\epsilon} - \frac{\xi g^2}{4\pi^2\epsilon} \\
Z_\mu &= 1 - \frac{\lambda}{24\pi^2\epsilon} - \frac{9g^4}{8\pi^2\lambda\epsilon} - \frac{\xi g^2}{8\pi^2\epsilon} \\
Z_\phi &= 1 + \frac{3g^2}{8\pi^2\epsilon} - \frac{\xi g^2}{8\pi^2\epsilon} \\
Z_\nu &= 1 + \frac{\xi g^2}{8\pi^2\epsilon} \\
Z_A &= 1 + \frac{g^2}{2\pi^2\epsilon} - \frac{\xi g^2}{8\pi^2\epsilon} \\
Z_g &= 1 - \frac{3g^2}{16\pi^2\epsilon} - \frac{\xi g^2}{16\pi^2\epsilon} \\
Z_c &= 1 + \frac{3g^2}{16\pi^2\epsilon} - \frac{\xi g^2}{16\pi^2\epsilon}.
\end{aligned} \tag{3.32}$$

The relations between the divergent pieces of the 1PI functions established by the BRST symmetry of Eq. 3.30 account for the renormalizability. The same definitions as in the commutative theory give the following beta functions and physical masses:

$$\begin{aligned}
\beta(\lambda) &= m_D\frac{\partial\lambda}{\partial m_D} = \frac{\lambda^2}{12\pi^2} - \frac{3\lambda g^2}{4\pi^2} + \frac{9g^4}{8\pi^2} \\
\beta(g^2) &= m_D\frac{\partial g^2}{\partial m_D} = \frac{-7g^4}{8\pi^2}
\end{aligned}$$

$$
\begin{aligned}
m^2 &= m_B^2\left[1+\frac{\lambda}{24\pi^2\epsilon}+\frac{3g^2}{8\pi^2\epsilon}+\frac{9g^4}{8\pi^2\lambda\epsilon}\right] \\
M^2 &= M_B^2\left[1+\frac{\lambda}{8\pi^2\epsilon}+\frac{g^2}{2\pi^2\epsilon}+\frac{9g^4}{4\pi^2\lambda\epsilon}\right].
\end{aligned}
\tag{3.33}
$$

The U(1) coupling remains asymptotically free, as in the free NC U(1) theory. As in the commutative case, we are able to define gauge independent couplings and masses.

We can also use these results to discuss spontaneously broken global symmetries in NC field theories. Upon removing the gauge field and gauge-scalar couplings from our Lagrangian, and making the gauge transformation global, we are left with the broken O(2) linear sigma model. The remaining renormalization constants are Z_ϕ, Z_μ, and Z_λ (with $\xi = g = 0$). Our results show that the continuum renormalization of this model is possible. While in the case of global symmetries both NC generalizations of $|\phi|^4$ discussed below Eq. 3.18 are consistent with the symmetry, our result indicates that the proper ordering is the one also consistent with a local realization of the symmetry. This is the only choice that leads to a one-loop renormalizable theory. We imagine that such considerations in choosing non-commutative extensions of commutative interactions hold generally.

3.4 Summary

We have found that the relations between counterterms which are necessary to renormalize spontaneously broken U(1) gauge theory occur in the noncommutative version of the theory; the BRST symmetry of the Lagrangian holds at the one-loop level. Upon taking the gauge field couplings to zero we obtain a consistent continuum renormalization of the broken O(2) linear sigma model. In the O(2) linear sigma model, both NC generalizations of the $|\phi|^4$ preserves the symmetry; however, renormalization requires us to pick the one also consistent with the local symmetry. We are not familiar with any discussions in the literature regarding how to choose NC extensions of commutative actions when some symmetry does not dictate a choice. However, we believe that the problem of ordering ambiguities arising from NC extensions of global symmetries can be solved by demanding that the local symmetry also hold. Note that this wouldn't have dictated a choice of scalar potential in [20], as either

$|\phi|^4$ generalization is consistent when working in the adjoint representation.

We have only discussed a single simple case in this chapter, that of a U(1) NC gauge theory coupled to a complex scalar field in the fundamental representation. Important generalizations are to consider different scalar representations, fermion contributions, and arbitrary U(N) groups. While we have nothing to say about the first two, we believe that the generalization to U(N) will be successful. The remarkable interplay between diagrams required to renormalize the $4A$ vertex, seen here in the scalar sector and in the gauge sector for general U(N) in [128] seems to indicate the consistency of these models.

The work in this chapter should be regarded as a "proof of principle" that spontaneously broken NC gauge theories are consistent. The non-commutativity of space-time at small scales is an exciting possible modification of fundamental physics. Our result provides a step towards a NC version of the Standard Model; the work in [42, 46, 53, 105, 132, 136], and the presence of tree level CP violation noted here and in [159], indicates that it might lead to interesting physics.

Chapter 4

Precision Measurements and Fermion Geography in the Randall-Sundrum Model

4.1 Introduction

We begin our discussion of theories with extra space-time dimensions in this chapter with a study of the Randall-Sundrum model.

The Randall-Sundrum (RS) model [146, 147] offers a new approach to the hierarchy problem. This scheme proposes that our four-dimensional world is embedded in a five-dimensional spacetime described by the metric

$$ds^2 = e^{-2\sigma(y)}\eta_{\mu\nu}dx^\mu dx^\nu - dy^2\,, \tag{4.1}$$

where $\sigma(y) = k|y|$, and with the 5^{th} dimensional coordinate $y = r_c\phi$ being compactified on an S^1/Z_2 orbifold bounded by branes of opposite tension at the fixed points $y = 0$ (known as the Planck brane) and $y = \pi r_c$ (TeV-brane). The parameter k describes the curvature of the space (with the five-dimensional curvature invariant being given by $\mathcal{R} = -20k^2$) and is of order the five-dimensional Planck scale, M_5, so that no additional hierarchy exists. Self-consistency of the classical theory requires [146, 147] that $|\mathcal{R}| \leq M_5^2$ so that quantum gravitational effects can be neglected. The space between the two branes is AdS_5 and their separation, πr_c, can be naturally stabilized [59, 87, 88, 160] with $kr_c \simeq 11-12$; we employ $kr_c = 11.27$ in the numerical results that follow. For such values of kr_c any mass of order the Planck scale on the $y=0$ brane appears to be suppressed by an amount $e^{-\pi kr_c} \sim 10^{-15}$ on the TeV brane. The presence of the exponential warp factor $e^{-\sigma(y)}$ thus naturally generates the hierarchy between the Planck and electroweak (EW) scales. The scale of physics on the TeV-brane is given by $\Lambda_\pi = \overline{M}_{Pl} e^{-kr_c\pi} \sim TeV$, where $\overline{M}_{Pl}$ is the reduced Planck scale. Integration over the extra dimension of the five dimensional RS action yields the relationship between the 4-dimensional Planck scale and the scales k and M_5:

$$\overline{M}_{Pl}^2 = M_5^3/k\,. \tag{4.2}$$

Together, this relation and the inequality $|\mathcal{R}| \leq M_5^2$ imply that the ratio $k/\overline{M}_{Pl}$ cannot be too large, and suggests that $k/\overline{M}_{Pl} \leq 0.1 - 1$.

In the original RS framework, gravity propagates freely throughout the bulk while the Standard Model (SM) fields are constrained to the TeV-brane. The graviton KK states have non-trivial wave functions in the extra dimension due to the warp factor, and have masses given by $m_n = x_n k e^{-\pi kr_c}$, where the x_n are the unequally spaced roots of the Bessel function J_1 and n labels the KK excitation level. The first graviton excitation thus naturally has a mass of order a TeV. The $n>0$ KK states couple to fields on the TeV-brane with a strength of Λ_π^{-1}. The graviton KK states can thus be produced in colliders as TeV-scale resonances with TeV^{-1}-size couplings to matter [63].

For additional freedom in model building, the original RS model has been extended to allow various subsets of the SM fields to reside in the bulk in the limit that the back-reaction on the metric can be neglected. This possibility allows for new techniques to address gauge coupling unification, supersymmetry breaking, the neutrino mass spectrum, and the fermion mass hierarchy. Placing the gauge fields of the SM alone in the bulk is problematic [58, 61, 108, 145], as all of the gauge KK excitations then have large couplings to the remaining fields on the TeV-brane; these couplings take on the value $\sqrt{2\pi kr_c}\, g \simeq 8.4\, g$, where g is the corresponding SM gauge coupling. EW precision data then constrain the masses of the first KK gauge states to be in excess of 25-30 TeV, thus requiring Λ_π to be in excess of 100 TeV [61]. This introduces a new hierarchy between Λ_π and the EW scale, and therefore this scenario is highly disfavored. It was subsequently shown that these constraints can be softened by also placing the SM fermions in the bulk [47, 80, 96, 110, 109, 112] and giving them a common five-dimensional mass $m = k\nu$. This leads to further model building possibilities provided ν is in the range $-0.8 \leq \nu \leq -0.3$ [64]; for larger values of ν the former strong coupling regime is again entered, while for smaller values potential problems with perturbation theory can arise [62]. In the absence of fine-tuning, these scenarios require that the Higgs field which breaks the symmetry of the SM remains on the TeV brane, as when bulk Higgs fields are employed, the experimentally observed pattern of W and Z masses cannot be reproduced. In this case, the W and Z obtain a common KK mass in addition to the usual contribution from the Higgs vev. It is then impossible to simultaneously maintain the two tree-level SM relationships $M_Z \cos\theta_w = M_W$ and $e = g \sin\theta_w$ [47, 64, 110, 145].

In this chapter we re-examine the possibility of allowing the SM fermions to propagate in the RS bulk. We show that if the third generation of fermions resides in the bulk, then large mixing between the fermion zero modes and their KK tower states is induced by the SM Higgs vev and the large top Yukawa coupling. This mixing results in contributions to $\delta\rho$ or T [142] which greatly exceeds the bound set by current precision EW measurements [97]. The only way to circumvent this problem is to raise the mass of the first KK gauge state above 25 TeV for any value of ν in its viable range, which again implies a higher value of Λ_π. Unless we are willing to fine tune Λ_π, we must then require the third generation fields to remain on the TeV-brane so that they have no KK excitations. If we treat the three generations symmetrically we must localize all of the fermions on the TeV-brane, and also confine the SM gauge sector to the TeV brane as discussed in the previous paragraph. We instead propose here a 'mixed' scenario which places the first two generations of fermions in the bulk and localizes the third on the wall. We find that mixing of the KK towers of these lighter generations with their zero modes does not yield a dangerously large value of $\delta\rho$ provided that $\nu \geq -0.6$. Furthermore, we show that values of ν near -0.4 to -0.5 may help explain the mass hierarchies m_c/m_t and m_s/m_b. We explore the possible signatures of this scenario at the LHC and future linear colliders,as well as in precision measurements and flavor changing neutral currents (FCNC); we find that the same parameter space which addresses the fermion mass hierarchies also allows a Higgs boson with a mass of 500 GeV, and is otherwise invisible at the LHC.

The outline of this chapter is as follows. In Section 2 we give a brief overview of the mechanics of the RS model which we will need for subsequent calculations. In Section 3 we examine the contributions to the ρ parameter when the third generation is in the bulk and show that this scenario is highly disfavored. We examine the present bounds on the KK mass spectrum in our mixed scenario that arise from precision EW data in Section 4. We demonstrate that SM Higgs masses as large as 500 GeV are now allowed by the electroweak fit since these contributions can be partially ameliorated from those of the KK states. Section 5 explores the implications of this scenario for the LHC, while Section 6 examines the signatures at a future e^+e^- linear collider and at GigaZ. In particular, we show that the KK states in this model lie outside the kinematically limited range of the LHC but yield observable indirect effects at a linear collider. Finally, we discuss constraints from FCNC in Section 7, and present our conclusions in Section 8.

4.2 The Standard Model Off the Wall

We present here a cursory formulation of the RS model in the case where the SM gauge and fermion fields propagate in the bulk; we refer the reader to [64] for a thorough introduction.

We begin by considering a $SU(\mathrm{N})$ gauge theory defined by the action

$$S_A = -\frac{1}{4}\int d^5x\sqrt{-G}\, G^{MK}G^{NL}F_{KL}F_{MN} \ , \tag{4.3}$$

where $G^{\alpha\beta} = e^{-2\sigma}\left(\eta^{\alpha\beta} + \kappa_5 h^{\alpha\beta}\right)$, $\sqrt{-G} \equiv |det(G_{MN})|^{1/2} = e^{-4\sigma}$, with $\kappa_5 = 2M_5^{-3/2}$, $\eta_{\alpha\beta}$ being the Minkowski metric with signature -2, and $h_{\alpha\beta}$ represents the graviton fluctuations. F_{MN} is the 5-dimensional field strength tensor given by

$$F_{MN} = \partial_M A_N - \partial_N A_M + ig_5\left[A_M, A_N\right] \ , \tag{4.4}$$

and A_M is the matrix valued 5-dimensional gauge field and g_5 is the corresponding 5-dimensional gauge coupling. We impose the gauge condition $A_5 = 0$; this is consistent with 5-dimensional gauge invariance [61], and with the Z_2-odd parity assigned to A_5 to remove its zero mode from the TeV-brane action. To derive the effective 4-dimensional theory we expand A_μ as

$$A_\mu(x, \phi) = \sum_{n=0}^{\infty} A_\mu^{(n)} \frac{\chi^{(n)}(\phi)}{\sqrt{r_c}} \ , \tag{4.5}$$

and require that the bulk wavefunctions $\chi^{(n)}$ satisfy the orthonormality constraint

$$\int_{-\pi}^{\pi} d\phi \, \chi^{(m)} \chi^{(n)} = \delta^{mn} \ . \tag{4.6}$$

We obtain a tower of massive KK gauge fields $A_\mu^{(n)}$, with $n \geq 1$, and a massless zero mode $A_\mu^{(0)}$. The KK masses m_n^A are determined by the eigenvalue equation

$$-\frac{1}{r_c^2} \frac{d}{d\phi} \left(e^{-2\sigma} \frac{d}{d\phi} \chi^{(n)} \right) = \left(m_n^A \right)^2 \chi^{(n)} \ . \tag{4.7}$$

This yields $m_n^A = x_n^A k e^{-kr_c\pi}$ on the TeV-brane, where the x_n^A are given in [61], with the first few numerical values being given by $x_1^A \simeq 2.45$, $x_2^A \simeq 5.57$, $x_3^A \simeq 8.70$. Explicit expressions for the bulk wavefunctions $\chi^{(n)}$ also contain the first order Bessel functions J_1 and Y_1, and can be found in [61, 64]; we note here only that the zero mode wavefunction is ϕ independent with $\chi^{(0)} = 1/\sqrt{2\pi}$.

We now add a fermion field charged under this gauge group, and able to propagate in the bulk. The action for this field is

$$S_F = \int d^4x \int dy \sqrt{-G} \left[V_n^M \left(\frac{i}{2} \bar{\Psi} \gamma^n \overleftrightarrow{D}_M \Psi + \text{h.c.} \right) - \text{sgn}(y) \, m \bar{\Psi} \Psi \right] \ , \tag{4.8}$$

where h.c. denotes the hermitian conjugate, $V_\mu^M = e^\sigma \delta_\mu^M$, $V_5^5 = -1$, $\gamma^n = (\gamma^\mu, i\gamma_5)$, D_M is the covariant derivative, and m is the 5-dimensional Dirac mass parameter. This 5-dimensional fermion is necessarily vector-like; we wish to obtain a chiral zero mode from its KK expansion. We follow [96] and expand the chiral components of the 5-dimensional field as

$$\Psi_{L,R}(x,\phi) = \sum_{n=0}^{\infty} \psi^{(n)}_{L,R}(x) \frac{e^{2\sigma}}{\sqrt{r_c}} f^{(n)}_{L,R}(\phi) \ , \tag{4.9}$$

and require the orthonormality conditions

$$\int_{-\pi}^{\pi} e^{\sigma} f_L^{(m)*} f_L^{(n)} = \int_{-\pi}^{\pi} e^{\sigma} f_R^{(m)*} f_R^{(n)} = \delta^{mn} \ . \tag{4.10}$$

The Z_2 symmetry of the 5-dimensional mass term in the action forces $f_L^{(n)}$ and $f_R^{(n)}$ to have opposite Z_2 parity; we choose $f_L^{(n)}$ to be Z_2 even and $f_R^{(n)}$ to be Z_2 odd. As shown in [96], this removes $f_R^{(0)}$ from the TeV-brane action, and we obtain the chiral zero mode $f_L^{(0)}$ necessary for construction of the SM. The KK states form a tower of massive vector fermions. The zero mode wavefunction is

$$f_L^{(0)} = \frac{e^{\nu\sigma}}{N_0^L} \ , \tag{4.11}$$

where $\nu = m/k$ and is expected to be of order unity, and N_0^L is determined from the orthonormality constraint of Eq. 4.10. Explicit expressions for the KK fermion masses and wavefunctions are given in [64]; we note here that $m_n^F = m_n^A$ when $\nu = -0.5$, and that $m_n^F > m_n^A$ for all other values of ν.

Inserting the KK expansions of both the gauge and fermion fields into the covariant derivative term in Eq. 4.8, we find that the ratios of fermion-gauge KK couplings to the corresponding 4-dimensional coupling are

$$C^{mnq}_{f\bar{f}A} = \sqrt{2\pi} \int_{-\pi}^{\pi} d\phi \, e^{\sigma} f_L^{(m)} f_L^{(n)} \chi^{(q)} \ , \tag{4.12}$$

where m, n, q label the excitation state. The coefficients $C^{00n}_{f\bar{f}A}$ and $C^{01n}_{f\bar{f}A}$ are shown in Fig. 4.1 for $n = 1, \ldots, 4$ as functions of ν. Notice that $C^{001}_{f\bar{f}A}$ vanishes at $\nu = -0.5$ and remains small for $\nu < -0.5$; this fact will be crucial in our later analysis.

In addition, the ratios of the KK triple gauge couplings (TGCs) to the TGC of the 4-dimensional theory are given by

$$C^{mnq}_{AAA} = \frac{g^{(mnq)}}{g} = \sqrt{2\pi} \int_{-\pi}^{\pi} d\phi \, \chi^{(m)} \chi^{(n)} \chi^{(q)} \ , \tag{4.13}$$

where we have identified $g = g_5/\sqrt{2\pi r_c}$. Using the zero mode wavefunction $\chi^{(0)} = 1/\sqrt{2\pi}$ and the orthonormality constraint of Eq. 4.6, we find that $C^{n00}_{AAA} = 0$ when $n > 0$; no coupling exists between two zero mode gauge particles and a KK gauge state.

We will also require the couplings between gauge KK states and the fermion fields which are localized on the TeV-brane [61]. The relevant action is

$$S_F = \int d^4x \int d\phi \sqrt{-G} \left[V^M_n \left(\frac{i}{2} \bar{\psi} \gamma^n \overleftrightarrow{D}_M \psi + \text{h.c.} \right) \right] \delta(\phi - \pi) \ . \tag{4.14}$$

Inserting the expansion of Eq. 4.5 into this expression, letting $\psi \to e^{3\sigma/2}\psi$, and setting $g = g_5/\sqrt{2\pi r_c}$, we find that the ratio of the nth KK gauge coupling to localized fermions relative to the corresponding SM coupling is

$$C^n_{f\bar{f}A} = \frac{\chi^{(n)}(\pi)}{\chi^{(0)}(\pi)} \ . \tag{4.15}$$

Utilizing the approximate expressions for the KK gauge wavefunctions in [64], these become

$$C^n_{f\bar{f}A} \approx (-1)^{n+1} \sqrt{2\pi k r_c} \ . \tag{4.16}$$

We now consider the final ingredient required for construction of the SM, the Higgs boson. As discussed in the introduction, the Higgs field must be confined to the TeV-brane to correctly break the electroweak symmetry. Its action can therefore be expressed as

$$S_H = \int d^4x \int dy \sqrt{-G} \left\{ G^{MN} D_M H \left(D_N H\right)^\dagger - V(H) \right\} \delta(y - r_c \pi) \ , \tag{4.17}$$

where $V(H)$ is the Higgs potential and D_M the covariant derivative. To properly normalize the Higgs field kinetic term we must rescale $H \to e^{\sigma} H$; we then expand H around its vev, v, insert the expansion of Eq. 4.5 into the covariant derivative, and identify $g = g_5/\sqrt{2\pi r_c}$. We find the gauge field mass terms

$$S_{H,mass} = \frac{1}{2} \sum_{m,n=0}^{\infty} a_{mn} \int d^4x \, m^2_{A,0} \, A^{(m)}_\mu A^{(n),\mu} \ , \tag{4.18}$$

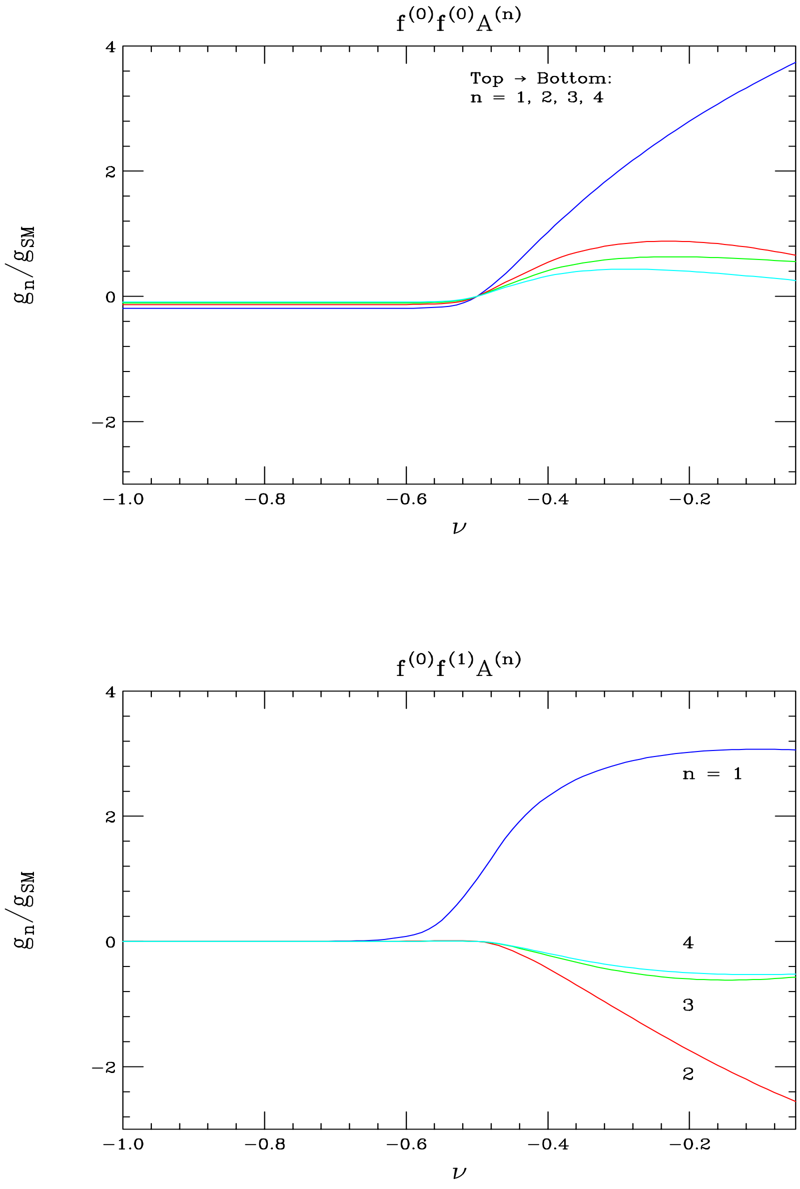

Figure 4.1: The coefficients $C^{00n}_{f\bar{f}A}$ (left) and $C^{01n}_{f\bar{f}A}$ (right) for $n = 1, \ldots, 4$ as functions of the fermion bulk mass parameter ν.

where $m_{A,0}$ is the gauge field mass of the 4-dimensional theory corresponding to the zero-mode of the gauge KK tower, and

$$a_{mn} = 2\pi \chi^{(m)}(\pi)\chi^{(n)}(\pi) \ . \tag{4.19}$$

We must diagonalize the full mass matrix, including the contributions arising from the KK reduction, to obtain the physical spectrum; we will do so for the SM gauge fields in a later section.

We now examine the mixing between fermion KK states induced by the Higgs field. When fermion fields are confined to the TeV-brane, no such mixing occurs; we therefore consider only the case where the fermions propagate in the bulk. The coupling between the Higgs and KK fermions is

$$S_{f\bar{f}H} = \frac{\lambda'}{k} \int d^4x \int dy \sqrt{-G} \left\{ H^\dagger \Psi_D \Psi_S^c + \text{h.c.} \right\} \delta\left(y - r_c\pi\right) \ , \tag{4.20}$$

where λ' is the 5-dimensional Yukawa coupling, and k has been introduced to make λ' dimensionless. Both Ψ_D and Ψ_S^c are left-handed Weyl fermions; we have introduced the subscripts D and S for these fields to indicate that in the SM, the Higgs couples $SU(2)_L$ doublets to $SU(2)_L$ singlets. After diagonalization of the mass matrix, the hermitian conjugates of the singlet fields will combine with the appropriate doublets to form Dirac fermions. Since, for our analysis, we are interested only in the contributions to the fermion masses arising from this action, we again rescale the Higgs field by e^σ, set the Higgs field equal to its vev and expand the left-handed fermion wavefunctions as in Eq. 4.9. Identifying

$$\lambda = \frac{\lambda' \left(f_L^{(0)}(\pi) \right)^2 e^{kr_c\pi}}{kr_c} \tag{4.21}$$

as the 4-dimensional Yukawa coupling, we find the fermion mass terms

$$S_{f,mass} = \sum_{m,n=0}^{\infty} b_{mn} \int d^4x \left\{ m_{f,0} \psi_D^{(m)} \psi_S^{c,(n)} + \text{h.c.} \right\} \ , \tag{4.22}$$

where $m_{f,0}$ is the zero mode mass obtained when the KK states decouple, and

$$b_{mn} = \frac{f_L^{(m)}(\pi) f_L^{(n)}(\pi)}{\left(f_L^{(0)}(\pi)\right)^2} \,. \tag{4.23}$$

Since $f_L^{(n)}(\pi)$ is approximately the same function for all $n \geq 1$, we will set $b_{0n} = \sqrt{f}$ and $b_{mn} = f$, with $m \neq n \neq 0$, in our analysis, where f is a ν dependent quantity that measures the strength of the mixing. This parameter is explicitly given by

$$f = 2\frac{1 - e^{-k\pi r_c(1+2\nu)}}{1+2\nu} \,. \tag{4.24}$$

These mass terms must be diagonalized in conjunction with the contributions from the KK reduction of Eq. 4.8; we will do so for the SM b and t quarks in the next section.

To complete our discussion of the RS model, we must briefly discuss the KK gravitons it contains. We parameterize the 5-dimensional metric as

$$G_{\alpha\beta} = e^{-2\sigma}\left(\eta_{\alpha\beta} + \kappa_5 h_{\alpha\beta}\right) \,, \tag{4.25}$$

where $\kappa_5 = 2M_5^{-3/2}$, $\eta_{\alpha\beta}$ is the Minkowski metric with signature -2, and the fluctuations of the bulk radius have been neglected. We then expand the graviton field $h_{\alpha\beta}$ as

$$h_{\alpha\beta}(x,\phi) = \sum_{n=0}^{\infty} h_{\alpha\beta}^{(n)}(x) \frac{\chi_G^n(\phi)}{\sqrt{r_c}} \,, \tag{4.26}$$

and impose the orthonormality constraint

$$\int_{-\pi}^{\pi} d\phi\, e^{-2\sigma} \chi_G^{(m)} \chi_G^{(n)} = \delta^{mn} \,. \tag{4.27}$$

The explicit forms of the KK graviton wavefunctions contain the second order Bessel functions J_2 and Y_2, and can be found in [63, 64]. Expressing the graviton masses as $m_n^G = x_n^G k e^{-kr_c\pi}$, we find the numerical values $x_1^G \simeq 3.83$, $x_2^G \simeq 7.02$, $x_3^G \simeq 10.17$ for the first few states which are given by $J_1(x_n^G) = 0$; notice that $m_n^G > m_n^A$. The couplings of the KK gravitons to fermions are given by

$$C^{mnq}_{f\bar{f}G} = \int_{-\pi}^{\pi} d\phi \frac{e^{\sigma} f^{(m)} f^{(n)} \chi^{(q)}_G}{\sqrt{kr_c}} \ . \tag{4.28}$$

The $C^{00n}_{f\bar{f}G}$ are presented in Fig. 4.2 as functions of ν. These couplings are relatively small, particularly when $\nu \leq -0.5$; this, and their large mass, render the KK gravitons unimportant in our analysis.

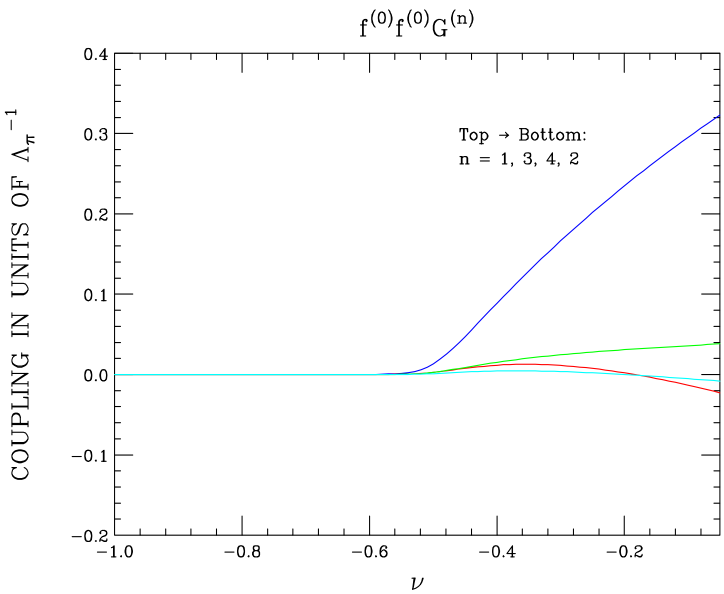

Figure 4.2: The coupling strengths $C^{00n}_{f\bar{f}G}$ for $n = 1, \ldots, 4$ as functions of the fermion bulk mass parameter ν in units of Λ_π.

We now have the tools necessary to build the SM within the RS framework. In the next section we will discuss the diagonalization of the t and b quark mass matrices, and the KK contributions to the ρ parameter. To whet the reader's appetite, we note that the off-diagonal mass matrix elements b_{mn}, with $m, n \neq 1$ and $m \neq n$, range from ≈ 10 when $\nu = -0.4$ to ≈ 700 when $\nu = -0.6$. This induces large mixing between the zero mode top quark and its KK tower, and creates couplings between the zero mode b quark and the top quark KK states. The large mass splitting between these states results in drastic alterations of ρ, and renders the placement of third generation quarks in the bulk inconsistent with EW measurements for a wide range of KK masses.

4.3 Fermion Mixing and the ρ Parameter

Since the top quark is quite heavy, with a mass $m_t \approx 175$ GeV, we expect the mixing between it and its KK tower to be stronger than that for the lighter fermions, and we focus here upon it and its isodoublet partner, the bottom quark. As mentioned previously, after performing the KK reduction of the 5-dimensional fermion field we obtain a chiral zero mode and a vector-like KK tower; this spectrum is presented pictorially for the top quark in Table 4.1.

Doublet		Singlet	
$\vdots$	$\vdots$	$\vdots$	$\vdots$
$T_L^{(2)}$	$T_R^{(2)}$	$t_L^{(2)}$	$t_R^{(2)}$
$T_L^{(1)}$	$T_R^{(1)}$	$t_L^{(1)}$	$t_R^{(1)}$
$T_L^{(0)}$	X	X	$t_R^{(0)}$

Table 4.1: Abbreviated list of the top quark KK states. The subscripts L and R denote left-handed and right-handed fields. $SU(2)_L$ doublets are denoted by capital T and singlets by lower case t. An X at a location in the table indicates that the state does not exist due to the orbifold symmetry.

We have exchanged the left-handed $SU(2)_L$ Weyl singlets introduced in the preceding section for their right-handed conjugates, but the reader should remember that these states are still described by the 5-dimensional wavefunctions $f_L^{(n)}(\phi)$. The top quark mass matrix receives two distinct contributions: the diagonal KK couplings between the doublet tower states and the singlet tower states, and off-diagonal mixings between the left-handed doublets and right-handed singlets arising from the Higgs coupling on the TeV-brane. We present below the mass matrix with only the zero modes and the first two KK levels included; the infinite-dimensional case can be obtained by a simple generalization. Working in the weak eigenstate basis defined by the vectors $\Psi_L^t = \left(T_L^{(0)}, T_L^{(1)}, t_L^{(1)}, T_L^{(2)}, t_L^{(2)}\right)$ and $\Psi_R^t = \left(t_R^{(0)}, t_R^{(1)}, T_R^{(1)}, t_R^{(2)}, T_R^{(2)}\right)$, we find

$$\mathcal{M}_t = \begin{pmatrix} m_{t,0} & \sqrt{f}m_{t,0} & 0 & -\sqrt{f}m_{t,0} & 0 \\ \sqrt{f}m_{t,0} & fm_{t,0} & m_1 & -\sqrt{f}m_{t,0} & 0 \\ 0 & m_1 & 0 & 0 & 0 \\ -\sqrt{f}m_{t,0} & -fm_{t,0} & 0 & fm_{t,0} & m_2 \\ 0 & 0 & 0 & m_2 & 0 \end{pmatrix} . \tag{4.29}$$

$m_{t,0}$ is the mass of the zero mode in the infinite KK mass limit, and m_1 and m_2 are the masses of the first two KK fermion states in the limit of vanishing Higgs couplings; f is the mixing strength introduced in the previous section. We fix $m_{t,0}$ by demanding that the lowest lying eigenvalue of this matrix reproduce the measured top quark mass, $m_t = 174.3$ GeV. Due to the large values of the off-diagonal elements, we diagonalize this mass matrix numerically, rather than analytically to $\mathcal{O}(m_{t,0}/m_1)$. We must necessarily truncate the KK expansion at some level; we have performed our analysis twice, once including only the first KK level and once keeping the first two levels, and have checked that adding more states only strengthens our conclusions. We examine the parameter region $-0.3 \geq \nu \geq -0.55$; the range $\nu > -0.3$ is strongly constrained by contact interaction searches at LEP [64], and the values $\nu \leq -0.55$ are prohibited by extrapolation of the results obtained below. This is essentially the same region studied in [67], where it was shown that the LHC will be able to probe the shift in the $Zt\bar{t}$ coupling for fermion KK mass values $m_1 \leq 15$ TeV. We will find that the region where $\nu \leq -0.3$ and $m_1 \leq 30 - 100$ TeV is already disfavoured by current measurements.

The Lagrangian containing the top quark mass terms and its interactions with the Z and $W^\pm$ gauge bosons is

$$\begin{aligned} \mathcal{L} &= \left(\bar{\Psi}^t_L \mathcal{M}_t \Psi^t_R + \text{h.c.}\right) + \bar{\Psi}^t_L \not{Z} C^Z_{t,L} \Psi^t_L + \bar{\Psi}^t_R \not{Z} C^Z_{t,R} \Psi^t_R \\ &\quad + \bar{\Psi}^t_L \not{W}^- C^W_L \Psi^b_L + \bar{\Psi}^t_R \not{W}^- C^W_R \Psi^b_R + \ldots + \text{h.c.} \, . \end{aligned} \tag{4.30}$$

We have introduced the basis Ψ^b_L and Ψ^b_R for the bottom quark in analogy with those for the top quark. The C^i_j are matrices containing the couplings of the various top quark states to the Z and $W^\pm$; letting g denote the SM electroweak coupling, c_W the cosine of the weak mixing angle, and g_L and g_R the couplings of the usual left-handed and right-handed SM fermions to the Z boson, we find

$$\begin{aligned}
C^Z_{t,L} &= \frac{g}{c_W}\,\mathrm{diag}\left(g_L, g_L, g_R, g_L, g_R\right) \ , \\
C^Z_{t,R} &= \frac{g}{c_W}\,\mathrm{diag}\left(g_R, g_R, g_L, g_R, g_L\right) \ , \\
C^W_L &= \frac{g}{\sqrt{2}}\,\mathrm{diag}\left(1,1,0,1,0\right) \ , \\
C^W_R &= \frac{g}{\sqrt{2}}\,\mathrm{diag}\left(0,0,1,0,1\right) \ .
\end{aligned} \tag{4.31}$$

In obtaining these matrices we have treated the $T_R^{(n)}$ as $SU(2)_L$ doublets and the $t_L^{(n)}$ as singlets as denoted in Table 4.1. We diagonalize $\mathcal{M}_t$ with the two unitary matrices U^t_L and U^t_R,

$$\mathcal{M}^D_t = U^t_L \mathcal{M}_t \left(U^t_R\right)^\dagger \ . \tag{4.32}$$

Diagonalization of the matrix $\mathcal{M}_t\mathcal{M}_t^\dagger$ determines U^t_L up to an overall phase matrix, while diagonalization of $\mathcal{M}_t^\dagger\mathcal{M}_t$ similarly fixes U^t_R. The mass eigenstate basis is obtained by multiplication of the weak eigenstate basis by the appropriate transformation matrix:

$$\Psi^t_L \to U^t_L \Psi^t_L \ \ , \Psi^t_R \to U^t_R \Psi^t_R \ . \tag{4.33}$$

The coupling matrices undergo a similar shift,

$$\begin{aligned}
C^Z_{t,L} &\to U^t_L C^Z_{t,L} \left(U^t_L\right)^\dagger \ , \\
C^Z_{t,R} &\to U^t_R C^Z_{t,R} \left(U^t_R\right)^\dagger \ , \\
C^W_L &\to U^t_L C^W_L \left(U^b_L\right)^\dagger \ , \\
C^W_R &\to U^t_R C^W_R \left(U^b_R\right)^\dagger \ .
\end{aligned} \tag{4.34}$$

We have also implicitly performed an identical diagonalization of the bottom quark mass matrix.

This procedure induces off-diagonal elements in both the Z and $W^\pm$ coupling matrices; consequently, fermions of widely varying masses enter the vacuum polarization graphs contributing to the Z and $W^\pm$ self energies. Such a scenario typically generates unacceptable contributions to the ρ parameter [163], defined as

$$\rho = \frac{\Pi_W\left(q^2=0\right)}{M_W^2} - \frac{\Pi_Z\left(q^2=0\right)}{M_Z^2}\ , \tag{4.35}$$

where $\Pi_X\left(q^2\right)$ is the X boson self energy function. We set $\Delta\rho = \rho - \rho_{SM}$, where ρ_{SM} is the contribution from the SM (t, b) doublet, and calculate ρ for our two cases: once including the shifted top and bottom quark zero modes and the first KK level only, and once including the zero modes and the first two KK states. $\Delta\rho$ is then a measure of the deviation from the SM prediction. The results are presented in Fig. 4.3 as functions of ν for several choices of m_1. The 95% CL exclusion limit [121] of $\Delta\rho \leq 2\times10^{-3}$ is also indicated. Notice that $\Delta\rho$ increases when we add the second KK level in our analysis; thus adding more states only increases $\Delta\rho$ further, and our neglect of these higher modes is justified. It is clear from the lower graph in Fig. 4.3 that consistency with the 95% CL exclusion limit restricts m_1 to the range $m_1 \geq 25$ TeV for all values of ν in the previously allowed range, and requires $m_1 \geq 100$ TeV when $\nu \leq -0.4$. When $\nu < -0.5$, including the range $\nu \leq -0.55$ that we have not presented, the corrections to ρ are so large that the perturbative definition of the Z and $W^\pm$ gauge bosons is no longer valid. We stress that these restrictions are lower bounds on the actual constraints as including more KK levels in our analysis will only strengthen these results. These results imply $\Lambda_\pi \geq 100$ TeV [61], with the exact choice depending on the value of ν, to avoid unacceptable contributions to $\Delta\rho$; the resulting hierarchy between the EW scale and the fundamental RS scale thus strongly disfavors allowing the third generation quarks to propagate in the bulk.

This restriction applies only to the top and bottom quarks; the first and second generations are much less massive, and the large mixing induced above by the top quark Yukawa coupling does not appear when considering these states. We have numerically checked that the contributions of bulk first and second generation quarks are consistent with the constraints on $\Delta\rho$, and hence the placement of the first two generations in the bulk is still allowed. But, is such a setup motivated? Does any interesting physics result from this construction? The answer to both questions is unequivocally yes, as we will demonstrate in the next section.

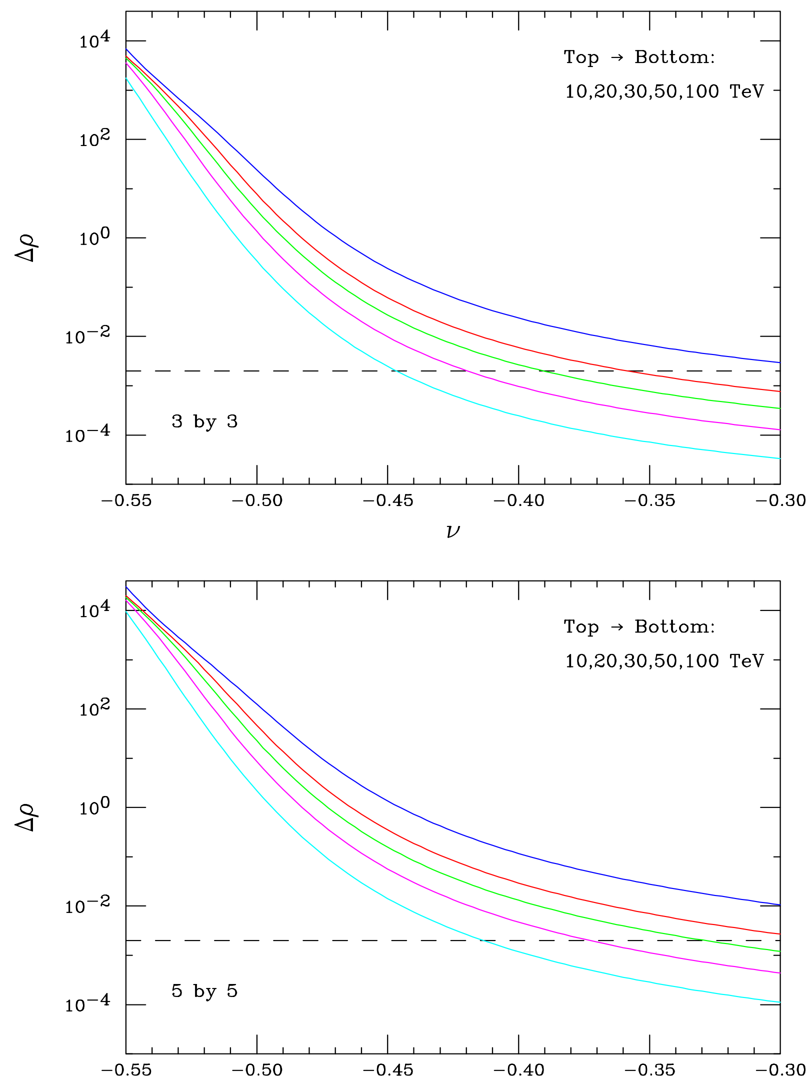

Figure 4.3: Contributions to $\Delta\rho$ from the zero modes and first KK level (top), and from the zero modes and first two KK levels (bottom). The dashed black line indicates where $\Delta\rho = 2 \times 10^{-3}$. The various curves correspond to when the masses of the first fermion KK excitation is taken to be $m_1 = 10, 20, 30, 50, 100$ TeV, from top to bottom.

4.4 The Third Generation On the Wall and the EW Precision Observables

A handful of authors have attempted to construct models explaining the quark and neutrino mass matrices within the framework of the RS model [96, 109, 112]. These ideas generically require the placement of fermions at different locations in the 5-dimensional bulk. We have already shown that the third generation quarks must lie on the TeV-brane; if we permit the first two generations to propagate in the bulk, can we explain the hierarchy between the Yukawa coupling of the top quark and those of the lighter quarks?

We consider first the coupling of the Higgs to a fermion field confined to the TeV-brane; the relevant action is

$$S^{wall}_{f\bar{f}H} = \lambda^{wall} \int d^4x \int dy \sqrt{-G} \left\{ H^\dagger \psi_D \psi^c_S + \text{h.c.} \right\} \delta\left(y - r_c\pi\right) \ , \tag{4.36}$$

where λ^{wall} is the Yukawa coupling of the localized fermion, chosen to be of $\mathcal{O}(1)$. To derive the 4-dimensional action we must rescale $\psi \to e^{3\sigma/2}\psi$ and $H \to e^\sigma H$ as before. The mass of this field is then $m^{wall} = \lambda^{wall} v/\sqrt{2}$. We have shown in Eq. 4.21 that the 4-d Yukawa coupling that determines the zero-mode mass of a bulk fermion is

$$\lambda^{bulk} = \frac{\lambda' \left(f^{(0)}_L(\pi)\right)^2 e^{kr_c\pi}}{kr_c} \ . \tag{4.37}$$

We now assume that the *fundamental* coupling that enters the 5-d bulk fermion action, λ', is also of order unity as is λ^{wall}. The factor $\left(f^{(0)}_L\right)^2 e^{kr_c\pi}/kr_c$ then suppresses λ^{bulk} with respect to λ^{wall}; we find $\lambda^{bulk} \approx \left(10^{-1} - 10^{-2}\right) \lambda^{wall}$ when $-0.55 \le \nu \le -0.35$, using the zero mode wavefunction given in Eq. 4.11. Choosing a value of ν in this region, ameliorates the hierarchy between the second and third generation quark Yukawa couplings. To be more explicit, with the top quark on the TeV brane and λ^{wall} of order unity, we expect a top mass near its experimental value. On the other hand, for the charm quark in the bulk, we expect a much smaller mass even if the bulk Yukawa coupling λ' is also of order unity. As an example, assuming $\lambda' = \lambda^{wall}$ and taking $\nu = -0.5$ one obtains $m_t/m_c \simeq 2\pi kr_c \simeq 70$ which is within a factor of 2 to 3 of the experimental value. A similar argument applies to the m_b/m_s ratio. The localization of the third generation on the TeV brane while keeping the first two in the bulk may thus help explain the fermion mass hierarchy. We do not attempt here to build a more detailed flavor model incorporating the off-diagonal CKM matrix elements, but instead examine the consequences of this simple situation. We focus on the region $-0.6 \leq \nu \leq -0.3$, extending slightly for completeness the range preferred by the quark Yukawa hierarchy. We study next the effects of KK gauge boson mixing on the EW precision observables; we will find that large mixing similar to that appearing in the top quark mass matrix relaxes the upper bound on the Higgs boson mass obtained in the standard EW fit [143].

The mass terms for the $W^{\pm}$ and Z can be obtained using Eq. 4.18 as a template; we find

$$S_{mass} = \sum_{m,n=0}^{\infty} a_{mn} \int d^4x \left(m_{W,0}^2 W_0^{+(m)} W_0^{-(n)} + \frac{1}{2} m_{Z,0}^2 Z_0^{(m)} Z_0^{(n)} \right) , \tag{4.38}$$

where the a_{mn} are given by Eq. 4.19 and we have for notational simplicity omitted the Lorentz indices of the gauge fields. The resulting $W^{\pm}$ mass matrix is

$$\mathcal{M}_W^2 = m_1^2 \begin{pmatrix} a_{11}x_W & a_{12}x_W & a_{13}x_W & \dots \\ a_{12}x_W & b_1^2 + a_{22}x_W & a_{23}x_W & \dots \\ a_{13}x_W & a_{23}x_W & b_2^2 + a_{33}x_W & \dots \\ \vdots & \vdots & \vdots & \end{pmatrix} , \tag{4.39}$$

where m_1 is the first KK gauge mass, $x_W = m_{W,0}^2/m_1^2$, and $b_i = m_i/m_1$ is the ratio of the ith KK mass to the first. The mass matrix for the Z is obtained by substituting $m_{W,0} \rightarrow m_{Z,0}$. The subscripts on the fields $W_0^{\pm}$ and Z_0, and on the masses $m_{W,0}$ and $m_{Z,0}$, indicate that these are not the physical fields and masses; they are the zero-mode fields and masses in the infinite KK limit. To obtain the physical spectrum we must diagonalize the mass matrices while respecting the appropriate constraints; these are the same as those developed for the interpretation of precision measurements at the Z-pole [7]. This prescription states that the following quantities are inputs to radiative corrections and to fits to the precision EW data: α as measured in Thomson scattering, G_F as defined by the muon lifetime, M_Z as determined from the Z line shape, m_t as measured at the Tevatron, and m_H, which is currently a free parameter. All other observables, such as the $W^{\pm}$ mass, M_W, and the width for the decay $Z \to l^+l^-$, Γ_l, are derived from these measured quantities; we must compare the RS model predictions for these parameters with the values obtained by experiment.

We examine the six relatively uncorrelated observables M_W, $\sin^2\theta_{\rm eff}$, Γ_l, R_b, R_c, and $\sin^2\theta_{\nu\rm N}$, and discuss in detail our procedure for deriving the RS model predictions for these quantities and then compare these predictions to the measured values. We consider tree level KK and loop level SM contributions to these observables, and assume that contributions from KK loops are higher order and therefore negligible. Our analysis differs slightly from those performed in models with KK gauge bosons arising from TeV^{-1}-sized extra dimensions [129, 152]. Here, the parameters a_{mn} of Eq. 4.19 which enter the mass matrices are rather large; the a_{1n}, with $n > 1$, have the approximate value $\sqrt{2\pi kr_c} \approx 8.4$, while the elements a_{mn}, with $m, n > 1$ and $m \neq n$, have the approximate value $2\pi kr_c \approx 71$. Although the ratios $x_{W(Z)} = m^2_{W,0(Z,0)}/m_1^2$ that appear in the mass matrices may be small, they are multiplied by these large coefficients, and to avoid errors we diagonalize the matrices and handle shifts of the precision observables numerically to all orders in $x_{W,Z}$, rather than performing the analysis analytically to $\mathcal{O}(x_{W,Z})$. This necessitates a truncation of the mass matrices; we work with 30×30 matrices, and have verified that increasing the size to 60×60 produces a negligible change in our results.

We first determine the parameter $m_{Z,0}$ by diagonalizing the Z mass matrix and demanding that the lowest eigenvalue reproduce the measured Z mass, M_Z . Armed with $m_{Z,0}$, we consider next the muon lifetime, through which the input parameter G_F is defined. The relevant decay is $\mu^- \to e^-\nu_e\bar{\nu}_\mu$. In the SM this proceeds at tree level through W exchange; it proceeds here through the exchange of the entire $W^{(n)}$ KK tower. G_F therefore becomes

$$\frac{G_F}{\sqrt{2}} = \frac{g^2}{8M_W^2} + \frac{g_0^2}{8}\sum_n \frac{c_n}{m_n^2} \ , \tag{4.40}$$

where the first term arises from the exchange of the zero mode and the second term from the higher KK states, and the c_n encapsulate the couplings of the KK gauge states to zero mode leptons. Some clarification of this expression is required. g is the coupling of the *physical* W obtained *after* diagonalization, whereas g_0 is the coupling that appears in the Lagrangian *before* diagonalization. To make this distinction explicit we express g as

$$g = g_0 \left\{1 - G(m_{W,0})\right\} \;, \tag{4.41}$$

where $G(m_{W,0})$ accounts for the admixture of KK states in the physical $W^{(0)}$ boson. After EW symmetry breaking, $g_0^2 = 4\pi\alpha/s_{w,0}^2$, where $s_{w,0}$ is the sine of the weak mixing angle obtained before including mixing effects: $s_{w,0}^2 = 1 - m_{W,0}^2/m_{Z,0}^2$. Substituting these relations into Eq. 4.40, we arrive at the condition

$$1 = \frac{\pi\alpha}{\sqrt{2} G_F\, M_W^2 s_{w,0}^2} \left\{1 - G(m_{W,0})\right\}^2 + \frac{\pi\alpha}{\sqrt{2} s_{w,0}^2} H(m_{W,0}) \;, \tag{4.42}$$

where we have introduced the dimensionless quantity

$$H(m_{W,0}) = \frac{1}{G_F} \sum_n \frac{c_n}{m_n^2} \;. \tag{4.43}$$

In the SM, after radiative corrections are included,

$$\frac{\pi\alpha}{\sqrt{2} G_F} \to \frac{\pi\alpha}{\sqrt{2} G_F\,(1 - \Delta r)} = m_{W,SM}^2 \left[1 - \frac{m_{W,SM}^2}{M_Z^2}\right] \;. \tag{4.44}$$

To incorporate radiative corrections in our analysis, we make this substitution in Eq. 4.42, and use the $m_{W,SM}$ calculated by ZFITTER [30] using M_Z as an input. We find the relation

$$1 = \frac{m_{W,SM}^2 \left[1 - \frac{m_{W,SM}^2}{M_Z^2}\right]}{M_W^2 \left[1 - \frac{M_W^2}{M_Z^2}\right]} \left\{1 - G(m_{W,0})\right\}^2 + \frac{\pi\alpha}{\sqrt{2}\left(1 - \frac{m_{W,0}^2}{m_{Z,0}^2}\right)} H(m_{W,0}) \;. \tag{4.45}$$

The only unknown quantity in this equation is $m_{W,0}$; the physical $W^{\pm}$ mass, M_W, is derived from $m_{W,0}$ through diagonalization of the $W^{\pm}$ mass matrix. We now scan over $m_{W,0}$ until we find a solution to this equation; the $m_{W,0}$ that furnishes this solution also predicts a M_W that can be compared with experiment.

We next compute the KK contributions to the effective coupling $\sin^2\theta_{eff}$, which appears in the dressed Zl^+l^- vertex [30]. In the SM,

$$\sin^2\theta_{eff,SM} = \kappa^Z \sin^2\theta_{w,SM} \ , \tag{4.46}$$

where θ_w is the on-shell weak mixing angle, $\sin^2\theta_{w,SM} = 1 - m^2_{W,SM}/M^2_Z$, and κ^Z contains a subset of the radiative corrections to the decay $Z \to l^+l^-$. In the RS model, the weak mixing angle that appears in the Zl^+l^- vertex is $s_{w,0}$; this is unaffected by diagonalization because $s_{w,0}$ enters the coupling of every KK excitationstate. The RS model expression for $\sin^2\theta_{eff}$ is

$$\sin^2\theta_{eff} = \kappa^Z s^2_{w,0} = \sin^2\theta_{eff,SM} \left(\frac{1 - \frac{m^2_{W,0}}{m^2_{Z,0}}}{1 - \frac{m^2_{W,SM}}{M^2_Z}} \right) \ , \tag{4.47}$$

where in the last step we have incorporated the ZFITTER predictions for $\sin^2\theta_{eff,SM}$ and $m_{W,SM}$ to correctly account for the SM radiative corrections.

The shifts of the remaining observables occur in a similar fashion as in the two examples given above, and hence we discuss them only briefly here. The width of the decay $Z \to \bar{f}f$ is

$$\Gamma_f = \frac{g^2 M_Z}{96\pi c_w^2} C_f \left\{ \left[1 - 4|Q_f|\sin^2\theta_{eff} + 8Q_f^2 \sin^4\theta_{eff} \right] \left(1 + \frac{2m_f^2}{M_Z^2} \right) - 3\frac{m_f^2}{M_Z^2} \right\} \ , \tag{4.48}$$

where C_f encapsulates kinematic factors, color sums for final state quarks, and factorizable radiative corrections [30]. This formula is valid in both the SM and the RS model, with the proviso that in the RS case g describes the coupling of the $Z^{(0)}$ obtained after diagonalization, $c_w \to c_{w,0}$ and $\sin^2\theta_{eff}$ is given by that described in the previous paragraph. Our previous results can be adapted to compute the shift in Γ_l. The change in the ratio of the $Z \to \bar{c}c$ width to the total hadronic width, $R_c = \Gamma_c/\Gamma_h$, can also be computed by following the outline presented for calculating the Γ_l shift. The derivation of the shift in $R_b = \Gamma_b/\Gamma_h$ proceeds similarly, except that the couplings of the higher gauge KK modes to the brane localized bottom quarks are those presented in Eqs. 4.15 and 4.16. Finally, $\sin^2\theta_{\nu\mathrm{N}}$ is determined experimentally through the measurement of R, which is the following ratio of neutrino-nucleon neutral and charged current scattering events:

$$R = \frac{\sigma^{\nu}_{NC} - \sigma^{\bar{\nu}}_{NC}}{\sigma^{\nu}_{CC} - \sigma^{\bar{\nu}}_{CC}} \ . \tag{4.49}$$

It becomes

$$R = \frac{1}{2} - \sin^2\theta_{\nu N} \tag{4.50}$$

at tree level in the SM, where the $W^{\pm}$ and Z coupling constants have cancelled in the ratio. When RS corrections are included, the gauge boson couplings no longer cancel because of different mixing effects in the $W^{\pm}$ and Z mass matrices, and $\sin^2\theta_{\nu N} \to s^2_{w,0}$. Again, these corrections to $\sin^2\theta_{\nu \mathrm{N}}$ can be easily obtained from our above results.

Having computed these corrections, we can now compare the RS model predictions for the precision observables with the values actually measured. We perform a χ^2 fit to the data, with the Higgs boson mass m_H and the first KK gauge mass m_1 as free parameters. The LEP Electroweak Working Group has quoted an upper limit on the Higgs mass in the SM of $m_H < 222$ GeV at the 95% confidence level [1], which we find corresponds to $\chi^2 = 23.3$. Following [152], we normalize our results by choosing this χ^2 value as our benchmark; we claim that the predictions are disfavoured at the 95% CL if $\chi^2 > 23.3$, and that the model fits the precision data otherwise. We use the input parameter values

$$\begin{aligned} M_Z &= 91.1875 \text{ GeV} \ , \\ G_F &= 1.16637 \times 10^{-5} \text{ GeV}^{-2} \ , \\ \alpha(m_e) &= 1/137.036 \ , \end{aligned} \tag{4.51}$$

and the experimental observable values and errors

$$\begin{aligned} M_W &= 80.451 \pm 0.033 \text{ GeV} \ , \\ \sin^2\theta_{eff} &= 0.23152 \pm 0.00017 \ , \\ \Gamma_l &= 83.991 \pm 0.087 \text{ MeV} \ , \\ R_b &= 0.21646 \pm 0.00065 \ , \end{aligned}$$

$$\begin{aligned} R_c &= 0.1719 \pm 0.0031 \ , \\ \sin^2\theta_{\nu\mathrm{N}} &= 0.2277 \pm 0.0016 \ , \end{aligned} \tag{4.52}$$

as presented in [1]. The results of these fits are presented in Fig. 4.4 as functions of both m_H and m_1, and for four representative values of the fermion bulk mass parameter ν. We have allowed m_H to range from 115 GeV to 1 TeV; higher Higgs masses are inconsistent with perturbative unitarity. This bound is modified slightly by KK gauge boson and graviton exchanges, but we have neglected these effects here. The six observables contribute to the fit with widely varying strengths; $\sin^2\theta_{eff}$ is very sensitive to deviations arising from RS physics throughout the entire m_H, m_1 region, while R_c does not significantly affect the χ^2 value for any choice of parameters. R_b is drastically altered when $\nu \leq -0.5$, where the light fermion couplings to KK gauge states either vanish or become small, but is less affected for larger values of ν. M_W, Γ_l, and $\sin^2\theta_{\nu\mathrm{N}}$ are somewhat less sensitive than $\sin^2\theta_{eff}$, and vary in relative importance as m_H and m_1 are changed. The allowed values of m_H vary with ν, but it is clear from Fig. 4.4 that for $\nu \geq -0.5$ Higgs masses in the range $300 - 600$ GeV are permitted for $n = 1$ KK gauge masses of $11 \sim 15$ TeV. A heavy Higgs has the effect of decreasing M_W, while the RS mixing effects increase it, and this compensation allows the predicted values of M_W, $\sin^2\theta_{eff}$, and Γ_l to be brought into good agreement with the measured values by tuning m_1. Shifts in R_b arising from the confinement of the third generation quarks to the TeV-brane prevent larger values of m_H from providing a good fit to the EW precision data. For each choice of ν and m_H there exists a range of allowed m_1 values that fits the EW precision data; the lowest allowed value of m_1 as a function of ν is presented in Fig. 4.5 for several choices of m_H. The drastic difference between the $m_H = 300$ and 400 GeV curves arises from the sharp distinction between allowed and disallowed KK masses imposed by the cut at $\chi^2 = 23.3$. The sharp rise for lower ν values and higher Higgs masses is due almost entirely to R_b. We present in Table 4.2 a summary of the allowed m_1 ranges for various choices of ν and m_H.

This relaxation of the upper bound on m_H is akin to that observed in [152]; the factors of 8.4 and 71 that appear in the off-diagonal elements of the $W^\pm$ and Z mixing

	-0.5	-0.4	-0.3
$m_H = 115$ GeV	> 13.9 TeV	> 14.8 TeV	> 15.8 TeV
300 GeV	$12.0 - 21.1$ TeV	$11.6 - 26.0$ TeV	$12.0 - 29.3$ TeV
500 GeV	X	$11.3 - 11.8$ TeV	$11.2 - 15.1$ TeV

Table 4.2: Table of m_1 ranges allowed by the EW precision data for several representative values of ν and m_H. An X denotes that the parameter choice corresponding to that location is not allowed.

matrices here allow the effect to occur for much larger KK masses. At this point the reader may wonder whether these high m_1 values can be probed at future colliders. We will show in the next section that they are indeed invisible at the LHC; however, the large KK gauge boson couplings to third generation quarks produces observable effects over most of the allowed parameter space at future e^+e^- colliders.

4.5 Searches at the LHC

We now discuss the prospects for detecting the gauge KK states which are consistent with our EW fit at the LHC. The primary discovery mode for new heavy gauge bosons at hadron colliders is high invariant mass Drell-Yan lepton pair production; at the LHC the relevant processes are $pp \to \gamma^{(1)}, Z^{(1)} \to \mu^+\mu^-,\ e^+e^-$. The contributing parton level processes are $q\bar{q} \to \mu^+\mu^-,\ e^+e^-$. We present $d\sigma/dm_{ll}$ for this process (with m_{ll} being the invariant mass of the final state lepton pair) in Fig. 4.6 for the parameter choices $\nu = -0.6, -0.5, -0.4, -0.3$ and $m_1 = 8, 10$ TeV. These values are representative of the allowed region for ν, but the gauge KK masses are lighter than those allowed by the EW fit. If the rates are unobservable at these points in parameter space, then the RS effects are undetectable for all interesting cases. The resonances are wide in this case primarily because of the large couplings of the KK gauge states to top and bottom quarks. With the $100\,\mathrm{fb}^{-1}$ of integrated luminosity envisioned for the LHC, the KK contributions to Drell-Yan production are indeed invisible. We present the expected number of excess events including both the $\mu^+\mu^-$ and e^+e^- channels for this value of integrated luminosity and for the two choices of

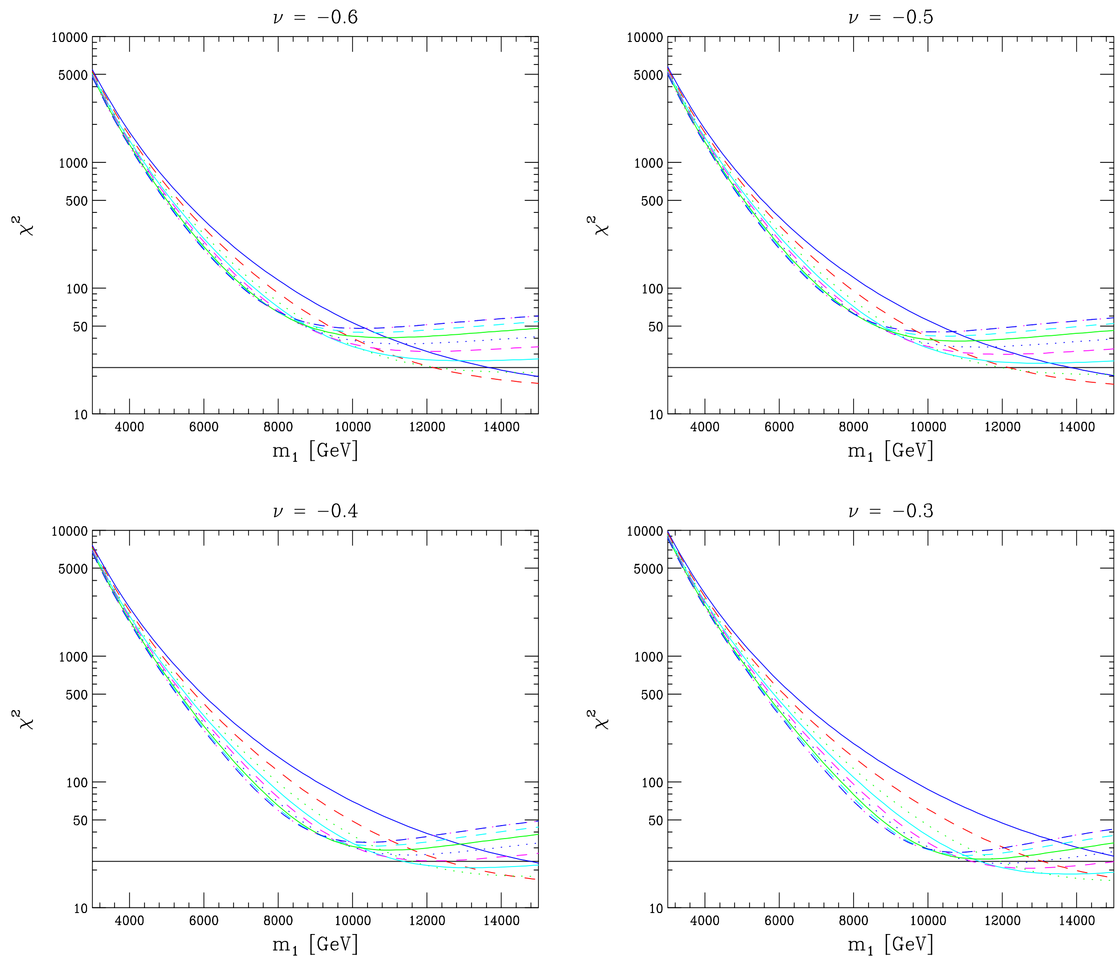

Figure 4.4: χ^2 values obtained in the fit to the EW precision data as a function of m_1 for four choices of ν, the fermion bulk mass parameter. The solid black line indicates where $\chi^2 = 23.3$, the value at which the 95% CL is reached. The colored curves are the RS model fit results for different Higgs boson masses; from top to bottom, on the left of each plot, the lines indicate $m_H = 115$, 200, 300, ..., 1000 GeV.

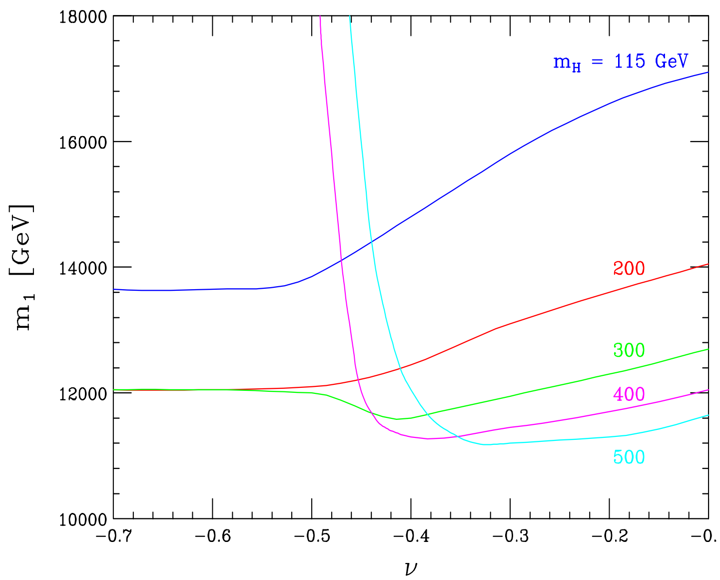

Figure 4.5: Lowest value of m_1 that fits the EW data as a function of ν, for five representative choices of m_H.

ν which produce the largest cross section in Table 4.3. Here, we have integrated over the invariant mass bins in which there is an excess of events over the SM predictions; this corresponds to the cuts $m_{ll} \geq 5$ TeV when $m_1 = 8$ TeV and $\nu = -0.3$, $m_{ll} \geq 6.5$ TeV when $m_1 = 8$ TeV and $\nu = -0.4$, $m_{ll} \geq 6$ TeV when $m_1 = 10$ TeV and $\nu = -0.3$, and $m_{ll} \geq 8$ TeV when $m_1 = 10$ TeV and $\nu = -0.4$. We have not attempted to study the depletion of events at lower m_{ll} because the event rates at the affected invariant masses are too low. Two effects are hindering the detection of the KK contributions: the small couplings of zero mode fermions to KK gauge states for $\nu \leq -0.5$, and the high KK masses which require the parton subprocesses to occur at energies where the quark distribution functions are small. Even with an order of magnitude increase in integrated luminosity, the production of the first gauge KK excitation that is consistent with the EW precision data is unobservable.

Another possible production mechanism for the KK gauge bosons at the LHC is W^+W^- fusion, $pp \to WW + 2$ jets$\to V^{(1)} + 2$ jets. The relevant triple gauge couplings, $W^{+(0)}W^{-(0)}\gamma^{(1)}$ and $W^{+(0)}W^{-(0)}Z^{(1)}$, are induced by mixing effects. We present the strengths of these vertices normalized to the SM couplings $W^+W^-\gamma$ and W^+W^-Z in Fig. 4.7. Very slight ν and m_H dependences enter these vertices; here

	$\nu = -0.4$	-0.3
$m_1 = 8$ TeV	6.4×10^{-4}	8.8×10^{-2}
10 TeV	4.9×10^{-6}	3.2×10^{-3}

Table 4.3: Table of expected Drell-Yan events at the LHC for various parameter choices $L = 100\,\mathrm{fb}^{-1}$. Both the $\mu^+\mu^-$ and e^+e^- channels have been included.

we fix $\nu = -0.3$ and $m_H = 115$ GeV, which maximizes their strength. For $m_1 \geq 11$ TeV, these couplings are a fraction, $\leq 10^{-3}$, of their SM strengths. This, and the fact that the W^+W^- fusion process is higher order in the EW coupling constant, render this a poor place in which to search for KK effects.

The only remaining possibility for detecting the KK states at the LHC is via deviations in top and bottom quark production. These processes are dominated at high energies by gluon initiated interactions; however, these do not receive any modifications from gluon KK states since $g^{(0)}g^{(0)}g^{(n)}$ couplings do not exist. We thus only examine top quark production, which receives a larger contribution from quark initiated processes, and where the large couplings of the KK gauge states to third generation quarks enter. The invariant mass distribution is presented in Fig. 4.8 for $m_1 = 10$ TeV and $\nu = -0.4$. Since the KK couplings to wall fermions do not decrease with KK level, we have checked that the contributions from including multiple states in the KK tower does not significantly enhance the effect. In fact, summing the first five KK contributions slightly decreases the cross section from that where only the first level is included due to the factor of $(-1)^n$ that enters the coupling of the nth KK level to top quarks. The expected number of excess events at the LHC is ≈ 0.14, assuming a cut on the invariant mass of the final state top quarks of $m_{tt} \geq 3.5$ TeV. As in the previous case of Drell-Yan production, this event rate is undetectable even with an order of magnitude increase in integrated luminosity. The slight depletion of events at lower invariant masses is similarly unobservable. We must therefore conclude that the KK excitations which relax the precision EW upper bound on the Higgs mass are invisible at the LHC.

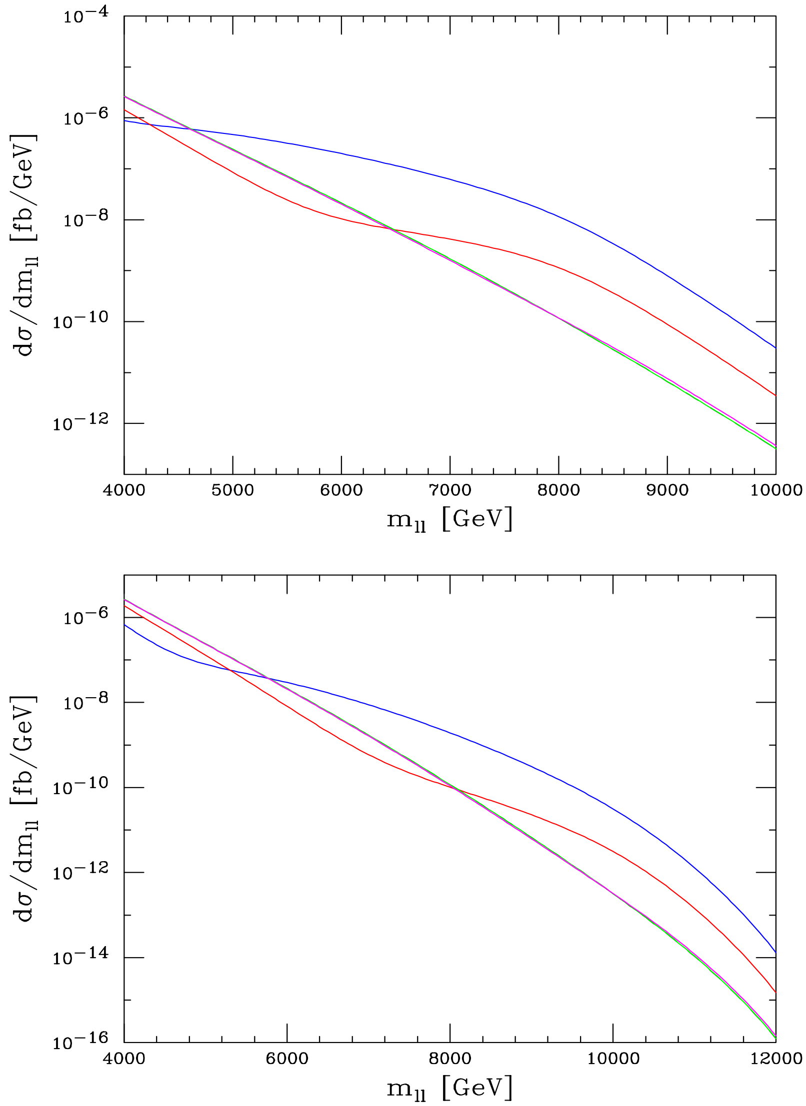

Figure 4.6: Cross sections for the process $pp \to \mu^+\mu^-$ for $m_1 = 8$ TeV (top) and $m_1 = 10$ TeV (bottom) as functions of the final state lepton pair invariant mass. The upper blue curves are for $\nu = -0.3$, the slightly lower red curves represent $\nu = -0.4$, and the three nearly degenerate straight lines correspond to $\nu = -0.5, -0.6$, and the SM. K-factors and a rapidity cut $|\eta| < 2.5$ have been included.

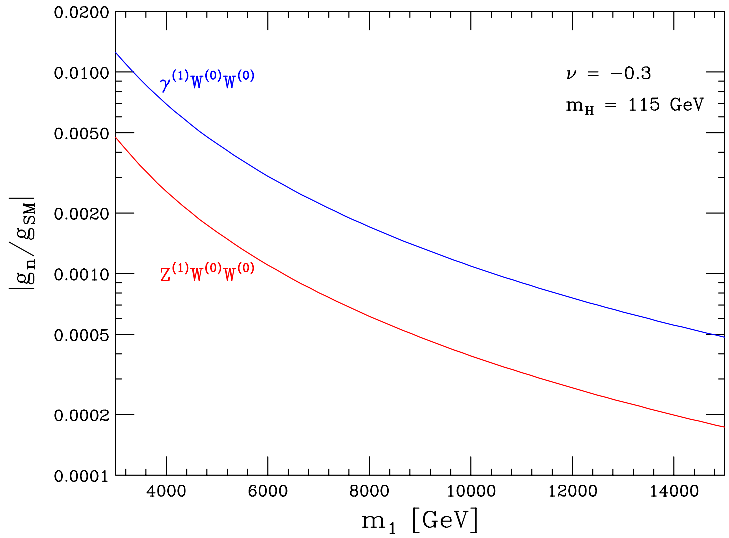

Figure 4.7: Couplings of $W^{\pm,(0)}$ to $\gamma^{(1)}$ and $Z^{(1)}$, normalized to the SM couplings of $W^{\pm}$ to γ and Z, as functions of m_1. The parameter values $\nu = -0.3$ and $m_H = 115$ GeV have been assumed.

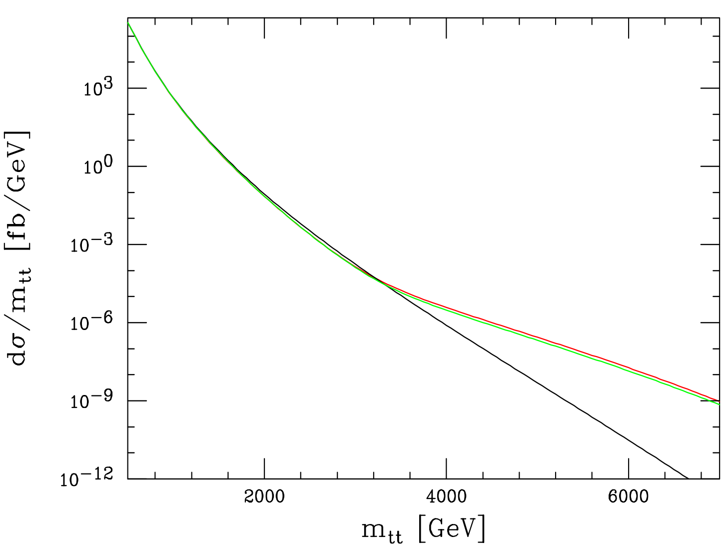

Figure 4.8: Invariant mass distributions for $pp \to t\bar{t}$ at the LHC including only the first KK state (top red line) and summing the first five KK gauge bosons (bottom green line), for $m_1 = 10$ TeV. The black line is the SM prediction.

4.6 Searches at Future TeV-scale Linear Colliders

We examine here whether KK gauge boson exchanges can be observed at a future e^+e^- collider with $\sqrt{s} = 500 - 1000$ GeV and $L = 500 - 1000\,\text{fb}^{-1}$. Since the anticipated center-of-mass energies are well below the 11 TeV KK gauge mass defining the lower edge of the allowed range from the EW fit, we study the off-resonance modification of fermion pair production, $e^+e^- \to f\bar{f}$. Z pair production receives no KK gauge contribution, while the $\gamma^{(1)}$ and $Z^{(1)}$ exchanges in $e^+e^- \to W^+W^-$ suffer from the weak triple gauge vertices displayed in Fig. 4.7. We perform a χ^2 fit to the total rate, binned angular distribution, and binned $\mathcal{A}_{LR}$ for fermion pair production to estimate the search reaches possible at TeV-scale linear colliders. We assume an 80% electron beam polarization, a 10° angular cut, statistical errors and a 0.1% luminosity error. We also use the following reconstructions efficiencies: a 100% τ efficiency, a 70% b quark efficiency, a 50% t quark efficiency, and a 40% c quark efficiency. The χ^2 values obtained in this analysis are shown in Fig. 4.9 for several choices of $\sqrt{s}$ and L.

We see from Fig. 4.9 that the effects of KK exchange exceed the 95% CL exclusion limit for all ν values in the allowed region and for $m_1 \leq 15$ TeV; the modifications when $\nu \geq -0.4$ reach the 5σ discovery limit. The parameter space $\nu \leq -0.5$ and $m_1 > 15$ TeV, part of which provides a good fit to the EW precision data, falls below the exclusion limit. It is possible that this difficulty can be alleviated with the inclusion of more observables. We note that a small hierarchy between the EW scale and Λ_π begins to develop in this region, and it is consequently not as favored as the $m_1 \leq 15$ TeV range. We note that the ordering of the $\nu = -0.6$ and -0.5 curves in the lower figure of Fig. 4.9 is correct.

We now subject this model to future high precision tests. Planned e^+e^- colliders are designed for operation on the Z-pole for a period sufficient to collect 10^9 Z events. This program, known as GigaZ, will reduce the error in $\sin^2\theta_{eff}$ to the 10^{-5} level and the error in R_b by a factor of 5 [5]. A phase of operation on the $W^\pm$ pair production threshold is also planned, which will reduce the error in the measurement of M_W to 6 MeV. We now return to our analysis of EW precision data and study the effects of

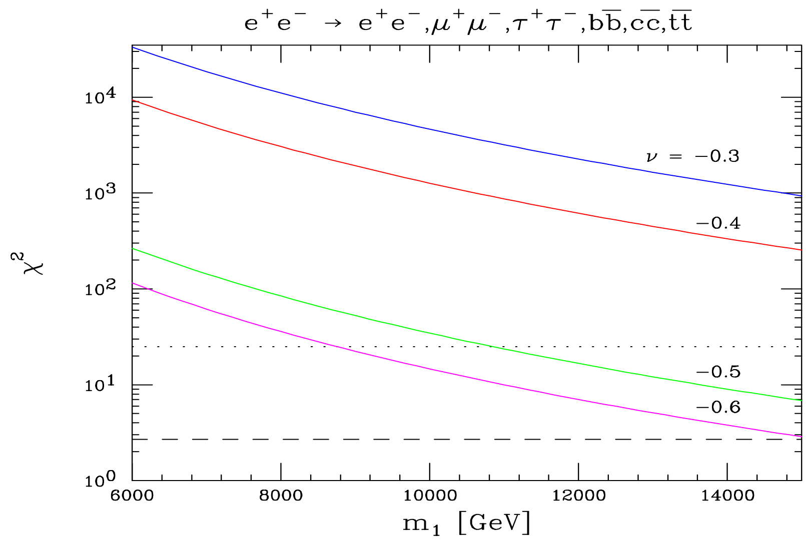

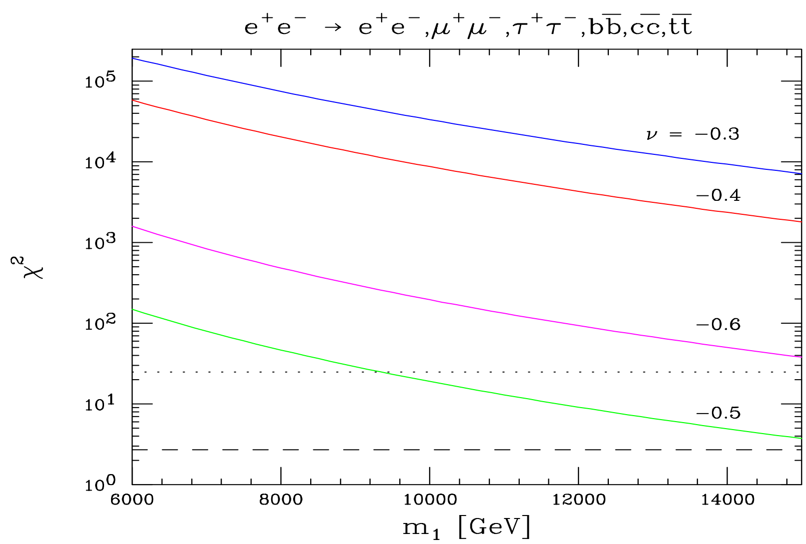

Figure 4.9: χ^2 values obtained by fitting the RS model predictions for fermion pair production to the SM for $\nu = -0.6, -0.5, -0.4, -0.3$, as functions of m_1. The upper figure assumes $\sqrt{s} = 500$ GeV and $L = 500\,\mathrm{fb}^{-1}$, while the lower assumes $\sqrt{s} = 1000$ GeV and $L = 1000\,\mathrm{fb}^{-1}$. The dashed line indicates the χ^2 necessary for exclusion of the model at the 95% CL, and the dotted line illustrates the χ^2 required for a 5σ discovery. The polarizations and reconstruction efficiencies assumed are presented in the text.

this error reduction, keeping the central values for the observables unchanged from the present and focusing on $\sin^2\theta_{eff}$, M_W, and R_b. Figures 4.10 and 4.11 display our results in the $\sin^2\theta_{eff}$ versus M_W plane and the $\sin^2\theta_{eff}$ versus R_b plane for $\nu = -0.5$ and -0.4. These figures show the current and expected experimental precisions, SM predictions, and RS model results for several different Higgs masses and m_1 choices.

It is difficult to predict what the status of fits to the EW precision data will be after the GigaZ program concludes, as a small shift in the experimental central values assisted by the small anticipated errors can drastically alter the current situation. If the central values remain unchanged, it is clear from these figures that the improved precision in the measurement of R_b will disfavor the heavier Higgs solutions, and require a large value of m_1, which reintroduces a hierarchy between Λ_π and the EW scale. However, the RS predictions for $\sin^2\theta_{eff}$ and M_W match experiment better than the SM results and can accommodate a heavy Higgs, and the global fit to the EW observables may prefer this solution. Whatever scenario is realized, it is certainly true that the entire parameter space, including the region inaccessible in off-resonance fermion pair production, can be probed at GigaZ.

4.7 Constraints from FCNCs

The placement of fermions in different locations in extra dimensions, on the TeV brane or in the bulk, leads to potentially dangerous FCNC since the Glashow-Weinberg-Paschos conditions [85, 140] for the natural absence of FCNC are no longer satisfied. These conditions are violated automatically whenever fermions of different generations are treated asymmetrically by some form of new physics and mixing occurs between the relevant states. Within the RS scenario that we have constructed, these FCNC can arise from a number of potential sources, not all of which present the same level of danger. A detailed analysis of FCNC effects is certainly beyond the scope of this paper and requires a specific flavor model as input; we simply outline the potential sources of FCNC and provide a few estimates of their size.

The most obvious sources of FCNC are from the exchanges of gauge bosons. The states in the gauge KK towers can feel the different fermion generation localities,

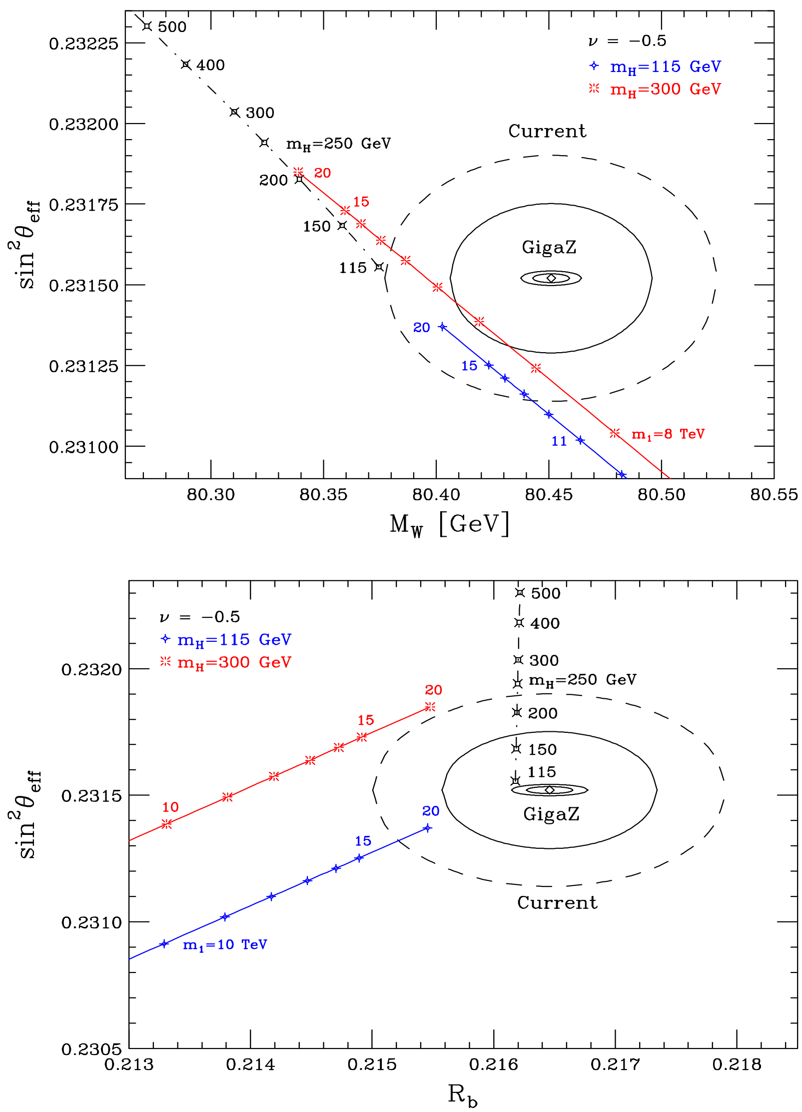

Figure 4.10: The planes $\sin^2\theta_{eff}$ versus M_W (top) and $\sin^2\theta_{eff}$ versus R_b (bottom) showing current and future sensitivities, SM predictions, and RS model predictions. The diamonds show the current measured values of the observables. The large solid and dashed ellipses represent respectively the 68% and 95% CL regions from current sensitivities, while the smaller solid ellipses anticipate the same after operation of GigaZ. The black dashdot lines show the SM predictions for different Higgs boson masses as labeled, while the solid colored lines show the RS model results for varying m_1 for two Higgs masses satisfying the current EW constraints.

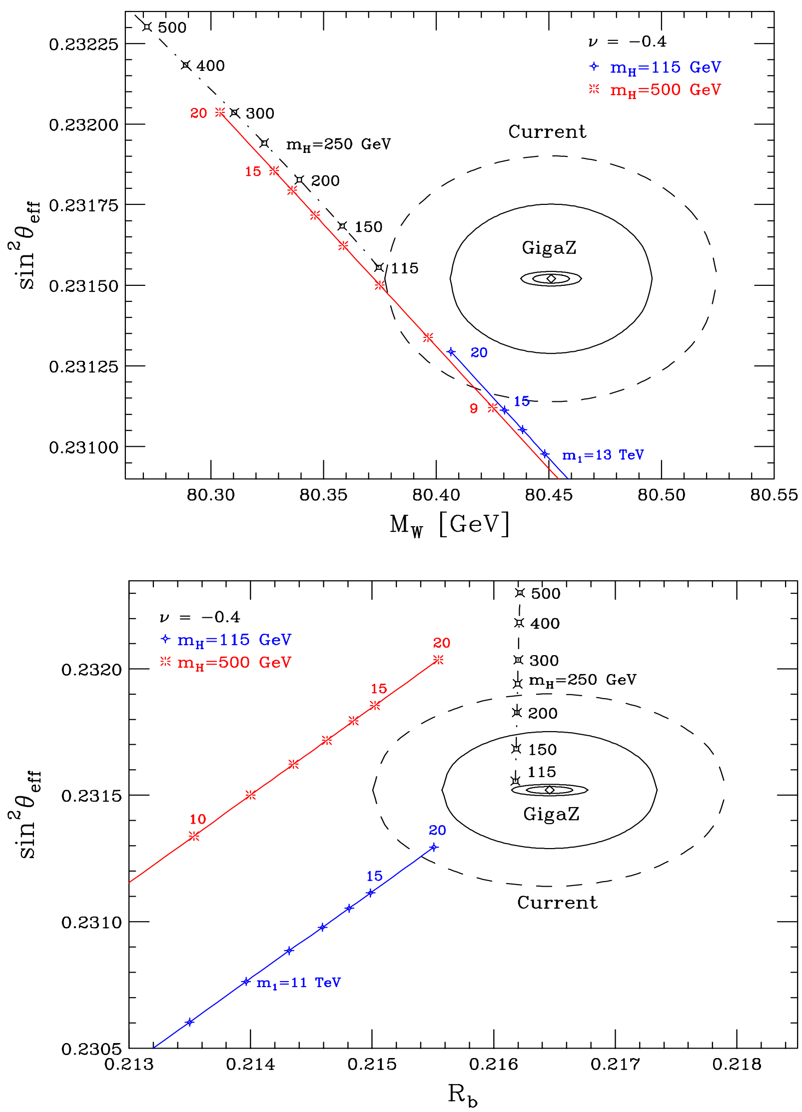

Figure 4.11: Same as the previous figure for $\nu = -0.4$, and different m_H choices.

and through intergenerational mixing can then induce FCNC. Furthermore, the couplings of the wall fields to the KK gauge states are enhanced by a factor of $\approx \sqrt{2\pi k r_c}$. Since zero mode KK gauge states in the limit of vanishing mixing are constrained by construction to have the same couplings to fermions as do the SM gauge bosons, such fields can only induce FCNC through the small admixture of KK weak eigenstates introduced by mixing. These effects are suppressed by small mixing angles, and are not as important as those arising from the KK towers themselves. We therefore expect that the KK gauge state contributions represent the greatest source of potentially dangerous FCNC.

Graviton KK towers can also probe the different locations of the SM fermion generations and induce FCNC-like couplings. However, in this case the potentially dangerous contributions are much smaller since (i) graviton-induced FCNC take the form of dimension-8 operators, in contrast to the dimension-6 KK gauge contributions, and lead to amplitudes which are suppressed by factors of order $m^2_{K,D,B}/\Lambda^2_\pi$. This is an enormous degree of suppression since we have shown that $\Lambda_\pi \geq 10$ TeV in the scenario presently under consideration. (ii) Unlike KK gauge fields, the graviton KK couplings to wall fields are not enhanced by the factor $\sqrt{2\pi k r_c}$.

How large are the KK gauge tower contributions? The answer depends upon which gauge boson we are examining. We neglect in this analysis the small mixing between the first and second generation fermions and their KK towers. Let $g^a_{L,R}$ represent the couplings of a particular fermion with electric charge Q to one of the neutral SM gauge bosons labeled by the index a. We write the fermion couplings to KK gauge states as $g^a_{L,R} c^n(\nu_i)$, where ν_i is the ith generation bulk mass parameter and n labels the gauge KK tower level. Note that the functions c^n in the present model are independent of chirality and the gauge boson under consideration. The fact that the $c^n(\nu_i)$ are different for each i generates the FCNC terms when we transform to the mass eigenstate basis. Let $U_{L,R}$ represent the matrices performing the bi-unitary transformation required to diagonalize the appropriate fermion mass matrix. The off-diagonal couplings in the mass eigenstate basis are then given by

$$(Q^n_{L,R})^a_{ij} = g^a_{L,R} \sum_k (U_{ik})_{L,R} c^n(\nu_k)(U^\dagger_{kj})_{L,R}\,. \tag{4.53}$$

For the specific model discussed in the previous sections we have $c^n(\nu_1) = c^n(\nu_2) \neq c^n(\nu_3)$, and we use the unitarity of the U's to rewrite these couplings as

$$(Q^n_{L,R})^a_{ij} = g^a_{L,R}[c^n(\nu_3) - c^n(\nu_1)](U_{i3}U^\dagger_{3j})_{L,R}\,. \tag{4.54}$$

With the third generation on the wall and the first and second in the bulk in the region $-0.6 \leq \nu_1 \leq -0.3$, it is clear that $|c^n(\nu_3) - c^n(\nu_1)| \simeq \sqrt{2\pi kr_c}$ for all n; *at worst*, the size of the off-diagonal couplings in our model is given by

$$(Q^n_{L,R})^a_{ij} = \sqrt{2\pi kr_c}\, g^a_{L,R}(U_{i3}U^\dagger_{3j})_{L,R}\,, \tag{4.55}$$

which is independent of n. The U_{ij} arise from some complete theory of flavor that must reproduce the experimentally measured CKM matrix V_{ij}. We therefore expect $U_{ij} \simeq V_{ij}$ and ee adopt this approximation in our estimates below.

The most stringent constraints on FCNC arise from low energy processes such as meson-antimeson mixing and rare decays [95]; we present here our estimate for $K-\bar{K}$ mixing. The above interaction generates a coupling which can be symbolically written as

$$\mathcal{L} = 2\pi kr_c \sum_a \sum_n (J^a_L + J^a_R)^2/m^2_n\,, \tag{4.56}$$

where $J^a_{L,R} = g^a_{L,r} V_{i3}V^\dagger_{3j}\bar{f}_i\gamma_\mu P_{L,R} f_j$, m_n is the mass of the nth KK gauge state, and we have summed all KK contributions. Recalling the lore that we can accurately approximate the matrix element of the two currents in the vacuum insertion approximation, we see that the KK gluon towers do not contribute. This is due to the fact that these states only couple to currents with non-zero color while both the meson and the vacuum are color singlets. Thus we need to consider only the Z and γ tower exchanges. Using $\sum_n m_n^{-2} \simeq 1.5 m_1^{-2}$ [61], $V_{13}V^\dagger_{32} \simeq A^2(1-\rho)^2\lambda^5$ in the Wolfenstein parameterization and

$$< K|J_L J_R|\bar{K} >= \Omega_K < K|J_L J_L|\bar{K} >= \Omega_K < K|J_R J_R|\bar{K} >\,, \tag{4.57}$$

with $\Omega_K \simeq 7$ [32] for the current-current matrix element, we arrive at

$$\frac{\Delta m_{KK}^{RS}}{\Delta m_{KK}^{SM}} \simeq 0.0098[1 + 0.73\Omega_K] \left(\frac{11TeV}{m_1}\right)^2 \simeq 0.06\,, \tag{4.58}$$

which is within the uncertainty of the SM result [36]. From this estimate we see that, at least for the $K - \bar{K}$ system, the RS FCNC contributions are rather small. We have also studied $B - \bar{B}$ mixing and obtain similar results.

Once a realistic theory of flavor within this RS model context is constructed, we can perform a more detailed and quantitative analysis of the potential impact of FCNC. It will be interesting to examine if existing bounds can provide further constraints on the RS model parameters within such a framework.

4.8 Summary

In this chapter we have re-examined the placement of SM fermions in the full 5-dimensional bulk of the Randall-Sundrum spacetime. We have found that mixing between the top quark zero mode and its KK tower, induced by the large top quark mass, yields shifts in the ρ parameter that are inconsistent with current measurements. To obviate these bounds we must take the fundamental RS scale $\Lambda_\pi \geq 100$ TeV, reintroducing the hierarchy between the Planck and EW scales and thus destroying the original motivation for the RS model. We instead proposed a mixed scenario which localizes the third generation of quarks, and presumably leptons, on the TeV-brane and allows the lighter two generations to propagate in the RS bulk. For values of the bulk mass parameter in the region $-0.55 \leq \nu \leq -0.35$, the same values allowed by both contact interaction searches and ρ parameter constraints arising from the first two generations, the fermions mass hierarchies m_c/m_t and m_s/m_b are naturally reproduced.

We next explored the consequences of this proposal for current precision EW measurements. We studied modifications of the electroweak observables caused by both mixing of the SM gauge bosons with their corresponding KK towers and the exchanges of higher KK states; we found that with KK masses $m_1 \approx 11$ TeV and bulk mass parameters $\nu \approx -0.5, -0.4$ a Higgs boson with mass $m_H \leq 500$ GeV can provide a good fit to the precision electroweak data. An analysis of the fit showed that the large couplings between the zero mode bottom quark and KK gauge bosons induced large shifts in R_b that prevented a heavier Higgs from being consistent with the precision data.

We then examined the signatures of this scenario at future high energy colliders. We found that the parameter region consistent with the precision electroweak data does not lead to any new physics signatures at the LHC; the expected event excess in both Drell-Yan and gauge boson fusion processes are statistically insignificant with the envisioned integrated luminosities, and the predicted modification of the $t\bar{t}$ production cross section is similarly unobservably small. The only new physics that the LHC would possibly observe is a Higgs boson apparently heavier than that allowed by the SM electroweak fits. By contrast, the parameter range $m_1 \leq 15$ TeV and $\nu \leq -0.3$ can be probed in fermion pair production processes at a future e^+e^- collider with center-of-mass energy of $500-1000$ GeV, while the region $m_1 \leq 25-30$ TeV and $\nu \leq -0.3$ is testable at GigaZ. For larger KK first excitation masses, we reintroduce the hierarchy between Λ_π and the electroweak scale.

Finally, we considered the possible constraints on this scenario arising from low energy FCNC. The asymmetric treatment of the three fermion generations allows KK Z-boson exchanges to mediate FCNC interactions. We estimated the contributions of such effects to meson-antimeson mixing, and found that their size is within the theoretical errors inherent to meson mixing. However, a detailed analysis of FCNC effects requires a full model of flavor, which we have not constructed.

In summary, we have found that the experimental restrictions on placing SM matter in the RS bulk lead naturally to a very interesting region of parameter space. This parameter region provides a geometrical origin for the fermion Yukawa hierarchies, and allows a heavy Higgs boson to be consistent with precision measurements while remaining otherwise invisible at the LHC. We believe that such features render this model worthy of further study.

Chapter 5

Kaluza-Klein Effects on Higgs Physics in Universal Extra Dimensions

5.1 Introduction

We studied in the previous chapter one example of an extra-dimensional theory, the Randall-Sundrum model, which embedded our 4-dimensional space-time into a curved 5-dimensional anti-de Sitter space. We examine here an alternative type of extra-dimensional theory which contains flat extra dimensions. There are many reasons for studying theories of this type. These models permit some of the qualitative features of string theory, such as the existence of extra dimensions and stringy resonances [3, 60, 78], to be tested experimentally, and predict the appearance of a wide variety of phenomenology at future high energy colliders [84, 100, 104, 135, 150]. They also furnish a slightly different solution to the hierarchy problem than the Randall-Sundrum model, by lowering the fundamental Planck scale to a TeV, rather than generating this hierarchy through a warp factor arising from the curved geometry. The string theoretic motivation for extra dimensions also allows new dimensions in which Standard Model (SM) or other non-gravitational fields can propagate [12]; for consistency with experimental constraints they must have a size of order an TeV^{-1}. Models utilizing this idea have been shown to yield a host of interesting phenomena, including TeV-scale unification [69, 70], explanations of fermion Yukawa hierarchies [21, 25], mechanisms for generating neutrino masses [24, 71], and methods of rendering axions invisible [72].

One proposed scenario, referred to as the Universal Extra Dimensions (UED) model [15], allows all the SM fields to propagate in TeV^{-1} extra dimensions. At tree level, the momentum in the extra dimensions is conserved, requiring pair production of the associated Kaluza-Klein (KK) modes at colliders and preventing tree level mixing effects from altering precision electroweak measurements. The compactification scale of the UED can therefore be as low as 300 GeV for one extra dimension, and remains less than 1 TeV for two UED. The phenomenological implications of UED for collider experiments [125, 151], $b \to s\gamma$ [4], and the muon anomalous magnetic moment [16] have been studied, and new mechanisms for generating neutrino masses [18] and suppressing proton decay [17] have been developed.

The detection of direct production of UED KK states at future colliders is expected to be difficult, for the following two reasons: (i) a remnant of extra-dimensional momentum conservation when loop effects are included implies the existence of a neutral, stable KK mode, leading to the necessity of interpreting missing energy signatures; (ii) the near degeneracy of the KK excitations within each level renders the mass shifts due to radiative corrections important in determining the pattern of decays [49, 50]. It is therefore interesting to determine whether there are other, indirect ways in which the effects of UED can be detected. One such possibility is through the modification of Higgs production and decay processes at future colliders; determining whether such deviations can significantly modify Higgs properties is also important considering the necessity of establishing the mechanism of electroweak symmetry-breaking. We study here the processes $gg \to h$, $h \to \gamma\gamma$, and $h \to \gamma Z$; the first interaction is the dominant Higgs production mechanism at the LHC, while the second is the primary discovery mode for $m_H \leq 150$ GeV. All three processes occur at one loop in the SM, the same order at which the KK excitations first contribute; we expect, and find, that these effects are quite large for the low compactification scales allowed for UED. Furthermore, graviton exchanges do not contribute to these processes at one loop, as can be seen from the unitary gauge Feynman rules in [84, 100]. We can therefore with some sense of security neglect the gravitational effects which presumably also appear in the complete theory in which the UED are embedded [98]. We concentrate here on modifications arising from physics in UED, rather than from other extra-dimensional models, for two reasons: (i) in the Randall-Sundrum model, in which SM fields can propagate in the full 5-dimensional spacetime, Higgs physics is already modified at tree-level by the mixing between the Higgs and the radion field which stabilizes the extra dimension [103]; (ii) in TeV^{-1} models where only gauge fields propagate in the bulk, we expect the effects to be unobservable, because the bound on the compactification scale from electroweak precision fits is quite high [129, 152] and the top quark KK excitations which induce the majority of the effects found here are absent.

This chapter is organized as follows. In Section 2 we review the formulation of the SM in one additional UED, focusing on the appropriate gauge-fixing and the mixing within the top quark KK tower. We study the modifications of the processes $gg \to h$, $h \to \gamma\gamma$, and $h \to \gamma Z$ in Section 3; we find that the heavy KK modes decouple, yielding finite, unambiguous results for one UED. For more than one UED the sums over KK modes diverge, and only qualitative statements can be made. We find that observable modifications to Higgs production and decay processes occur for compactification masses $m_1 \leq 1.5$ TeV; the $gg \to h$ production rate is increased by $\approx 10\% - 85\%$ for $1500 \geq m_1 \geq 500$ GeV, respectively, while the decay widths are shifted by $\leq 20\%$ in the same interval. We summarize our results in Section 4.

5.2 Kaluza-Klein Reduction of the 5-dimensional Standard Model

We review here the formulation of the UED model, in which all the SM fields can propagate in the extra dimensions. We restrict our attention to the 5-dimensional scenario, and focus on the issues most pertinent to our calculation: the appropriate choice of gauge-fixing and the effects of mixing within the top quark KK tower. A detailed construction of the SM in UED is given in [15], while a discussion of generalized R_ξ gauges in a variety of extra-dimensional models is presented in [138].

We begin with the action

$$
\begin{aligned}
S \;=\; & \int_{-\pi R}^{\pi R} dy \int d^4x \Big\{ -\frac{1}{2}\sum_{i=1}^{3} \mathrm{Tr}\left[F_{iMN}F_i^{MN}\right] + (D_M H)^\dagger D^M H + \mu^2|H|^2 - \frac{\lambda_5}{4}|H|^4 \\
& + i\,\bar{Q}\,\not{D}Q + i\,\bar{t}\,\not{D}\,t + \left[\lambda_5^t \bar{Q}\,i\,\sigma_2\,H^*\,t + \text{h.c.}\right] \Big\} \,. \qquad (5.1)
\end{aligned}
$$

Here (M, N) are the 5-dimensional Lorentz indices, and R is the radius of the fifth dimension, which we have anticipated compactifying on S^1/Z_2. H is the Higgs doublet, and the F_i^{MN} are the field strengths for the SM gauge groups. Q is the third generation quark doublet and t is the top quark singlet; we will not need the remaining SM fermions in our analysis, and they have consequently not been included. The covariant derivative D_M can be expressed as

$$
D_M = \partial_M - i\sum_{i=1}^{3} g_5^i\, T_i^a A_{iM}^a \;, \qquad (5.2)
$$

where the g_5^i are the 5-dimensional coupling constants for $U(1)_Y$, $SU(2)_L$, and $SU(3)_c$, and the T_i^a are the generators of these groups. The 5-dimensional Dirac matrices are $\gamma^M = (\gamma^\mu, i\,\gamma^5)$. μ^2, λ_5, and λ_5^t are the 5-dimensional versions of the usual Higgs couplings and top quark Yukawa coupling. The parameters λ_5, λ_5^t, and g_5^i are dimensionful, and must be rescaled to obtain the correct dimensionless SM couplings; no rescaling is necessary for the the Higgs mass parameter μ^2.

To derive the 4-dimensional effective action we must expand the 5-dimensional fields into their KK modes; we must also remove several extra massless particles from the resulting theory. Five-dimensional fermions are necessarily vector-like, and we wish to obtain the chiral zero modes necessary for construction of the SM; this necessitates the removal of the extra zero modes appearing in the top quark KK tower. We also must eliminate the zero modes of the scalars A_i^5 that arise in the reduction of the gauge fields. To do this we follow the standard recipe of compactifying the fifth dimension on an S^1/Z_2 orbifold and requiring that the fields whose zero modes we wish to remove are odd under the orbifold projection $y \to -y$. The appropriate

KK expansions of the 5-dimensional fields are:

$$\begin{aligned}
H(x^\mu, y) &= \frac{1}{\sqrt{2\pi R}}\left\{H^{(0)}(x^\mu) + \sqrt{2}\sum_{n=1}^{\infty} H^{(n)}(x^\mu)\cos\left(\frac{ny}{R}\right)\right\} , \\
A_{i\,\mu}(x^\nu, y) &= \frac{1}{\sqrt{2\pi R}}\left\{A_{i\,\mu}^{(0)}(x^\nu) + \sqrt{2}\sum_{n=1}^{\infty} A_{i\,\mu}^{(n)}(x^\nu)\cos\left(\frac{ny}{R}\right)\right\} , \\
A_i^5(x^\nu, y) &= \frac{1}{\sqrt{\pi R}}\sum_{n=1}^{\infty} A_i^{5(n)}(x^\nu)\sin\left(\frac{ny}{R}\right) , \\
Q(x^\nu, y) &= \frac{1}{\sqrt{2\pi R}}\Big\{Q_L^{(0)}(x^\nu) + \sqrt{2}\sum_{n=1}^{\infty}\Big[P_L Q_L^{(n)}(x^\nu)\cos\left(\frac{ny}{R}\right) \\
&\quad + P_R Q_R^{(n)}(x^\nu)\sin\left(\frac{ny}{R}\right)\Big]\Big\} , \\
t(x^\nu, y) &= \frac{1}{\sqrt{2\pi R}}\Big\{t_R^{(0)}(x^\nu) + \sqrt{2}\sum_{n=1}^{\infty}\Big[P_R t_R^{(n)}(x^\nu)\cos\left(\frac{ny}{R}\right) \\
&\quad + P_L t_L^{(n)}(x^\nu)\sin\left(\frac{ny}{R}\right)\Big]\Big\} , \qquad (5.3)
\end{aligned}$$

where we have introduced the projection operators $P_{R,L} = (1 \pm \gamma^5)/2$. We thus obtain the desired zero modes $A_{i\,\mu}^{(0)}$, $Q_L^{(0)}$, and $t_R^{(0)}$, corresponding to the SM fields. These expansions should be inserted into the action of Eq. 5.1. We must also expand the zero mode Higgs doublet around its vev, and express the KK Higgs doublets in terms of their component fields:

$$H^{(0)} = \begin{pmatrix} \phi^{(0)+} \\ \frac{1}{\sqrt{2}}\left(\nu + h^{(0)} + i\,\chi^{(0)}\right) \end{pmatrix} , \quad H^{(n)} = \begin{pmatrix} \phi^{(n)+} \\ \frac{1}{\sqrt{2}}\left(h^{(n)} + i\,\chi^{(n)}\right) \end{pmatrix} . \qquad (5.4)$$

Here ν is the usual 4-dimensional Higgs vev, $h^{(0)}$ is the physical zero mode Higgs, and $\chi^{(0)}$, $\phi^{\pm(0)}$ are the zero mode Goldstone bosons. The $h^{(n)}$ are the CP-even Higgs KK excitations, the $\chi^{(n)}$ are CP-odd scalars that will combine with the $Z^{5(n)}$ to form a tower of CP-odd Higgs bosons and generate the longitudinal components for the $Z_\mu^{(n)}$, and the $\phi^{\pm(n)}$ are charged scalars that together with the $W^{\pm 5(n)}$ will form a tower of charged Higgs scalars and longitudinal components for the $W_\mu^{\pm(n)}$. Inserting the expansions of Eqs. 5.3 and 5.4 into the action in Eq. 5.1 leads to a slew of mass terms, mixings, and couplings. We focus first on the masses and mixings in the gauge sector, introducing the appropriate gauge-fixing terms and deriving the spectrum of physical states and Goldstone fields.

We first examine the photon KK tower; the relevant mass terms and mixings are

$$S^A = \int d^4x \sum_{n=1}^{\infty} \left\{ \frac{1}{2} m_n^2 A_\mu^{(n)} A^{\mu(n)} - m_n A_\mu^{(n)} \partial^\mu A^{5(n)} \right\} \ , \tag{5.5}$$

where $m_n = n/R$ is the KK mass of the nth level arising from the derivative ∂_5 acting on the 5-dimensional wavefunctions of Eq. 5.3. The most natural choice of gauge-fixing is the five-dimensional analog of the Feynman gauge,

$$S_{gf}^A = -\frac{1}{2} \int_{-\pi R}^{\pi R} dy \int d^4x \left(\partial_M A^M \right)^2 \ . \tag{5.6}$$

Utilizing the KK expansion of A^M, and summing Eqs. 5.5 and 5.6, we find that the mixing between $A_\mu^{(n)}$ and $A^{5(n)}$ cancels, and that we are left with the mass terms

$$S^A + S_{gf}^A = \frac{1}{2} \int d^4x \sum_{n=1}^{\infty} \left\{ m_n^2 A_\mu^{(n)} A^{\mu(n)} - m_n^2 \left(A^{5(n)} \right)^2 \right\} \ ; \tag{5.7}$$

the spectrum then consists of a massless zero mode $A_\mu^{(0)}$, a tower of KK modes $A_\mu^{(n)}$ with masses m_n, and a tower of Goldstone particles $A^{5(n)}$ also with mass m_n. The treatment of the gluon KK tower proceeds identically, and we will not present it explicitly.

We next study the Z boson KK tower, together with the KK excitations of the zero mode Goldstone particle, χ. The corresponding masses and mixing terms are

$$\begin{aligned} S^Z \ = \ & \frac{1}{2} \int d^4x \Big\{ M_Z^2 \left(Z^{(0)} \right)^2 + 2 M_Z Z_\mu^{(0)} \partial^\mu \chi^{(0)} + \sum_{n=1}^{\infty} \Big[- m_n^2 \left(\chi^{(n)} \right)^2 + m_{Z,n}^2 Z_\mu^{(n)} Z^{\mu(n)} \\ & - M_Z^2 \left(Z^{5(n)} \right)^2 - 2 m_n M_Z Z^{5(n)} \chi^{(n)} + 2 Z_\mu^{(n)} \partial^\mu \left(M_Z \chi^{(n)} - m_n Z^{5(n)} \right) \Big] \Big\} \ , \end{aligned} \tag{5.8}$$

where we have introduced the abbreviation $m_{Z,n}^2 = M_Z^2 + m_n^2$. We choose the straightforward 5-dimensional generalization of the usual SM Feynman gauge,

$$S_{gf}^Z = -\frac{1}{2} \int_{-\pi R}^{\pi R} dy \int d^4x \left(\partial_M Z^M - M_Z \chi \right)^2 \ ; \tag{5.9}$$

utilizing the KK expansion of Eq. 5.3 and combining this with Eq. 5.8, we derive the following mass terms:

$$\begin{aligned} S^Z + S^Z_{gf} &= \frac{1}{2}\int d^4x \left\{ M_Z^2 Z_\mu^{(0)} Z^{\mu(0)} - M_Z^2 \left(\chi^{(0)}\right)^2 + \sum_{n=1}^{\infty}\left[m_{Z,n}^2 Z_\mu^{(n)} Z^{\mu(n)} \right.\right. \\ & \left.\left. -m_{Z,n}^2 \left(\chi^{(n)}\right)^2 - m_{Z,n}^2 \left(Z^{5(n)}\right)^2 \right]\right\} ; \qquad (5.10) \end{aligned}$$

the mixing between $Z_\mu^{(n)}$ and $Z^{5(n)}$ cancels. It is clear from Eq. 5.8 that the linear combinations of fields that serve as Goldstone modes for the Z boson KK tower are

$$G_Z^{(n)} = \frac{M_Z \chi^{(n)} - m_n Z^{5(n)}}{\sqrt{M_Z^2 + m_n^2}} , \qquad (5.11)$$

while the physical CP-odd scalars are

$$\chi_Z^{(n)} = \frac{m_n \chi^{(n)} + M_Z Z^{5(n)}}{\sqrt{M_Z^2 + m_n^2}} . \qquad (5.12)$$

With the gauge choice we have made, the states $G_Z^{(n)}$, $\chi_Z^{(n)}$, and $Z_\mu^{(n)}$ all possess the mass $m_{Z,n}$.

Finally, we consider the masses and mixing terms involving the $W^\pm$ KK tower and the KK excitations of the zero mode Goldstone fields $\phi^\pm$:

$$\begin{aligned} S^W &= \int d^4x \left\{ M_W^2 W_\mu^{+(0)} W^{-\mu(0)} + iM_W \left(W_\mu^{-(0)} \partial^\mu \phi^{+(0)} - W_\mu^{+(0)} \partial^\mu \phi^{-(0)} \right) \right. \\ & + \sum_{n=1}^{\infty} \left[- m_n^2 \phi^{+(n)} \phi^{-(n)} + m_{W,n}^2 W_\mu^{+(n)} W^{-\mu(n)} - M_W^2 W^{+5(n)} W^{-5(n)} \right. \\ & -i m_n M_W \left(W^{-5(n)} \phi^{+(n)} - W^{+5(n)} \phi^{-(n)} \right) - W_\mu^{-(n)} \partial^\mu \left(m_n W^{+5(n)} \right. \\ & \left.\left. \left. -iM_W \phi^{+(n)} \right) - W_\mu^{+(n)} \partial^\mu \left(m_n W^{-5(n)} + iM_W \phi^{-(n)} \right) \right] \right\} , \qquad (5.13) \end{aligned}$$

where we have abbreviated $m_{W,n}^2 = M_W^2 + m_n^2$. The appropriate choice of gauge-fixing term is again the obvious 5-dimensional extension of the SM Feynman gauge:

$$S^W_{gf} = -\int_{-\pi R}^{\pi R} dy \int d^4x \left(\partial_M W^{+M} - iM_W \phi^+ \right) \left(\partial_M W^{-M} + iM_W \phi^- \right) . \qquad (5.14)$$

Inserting the KK expansions of Eq. 5.3 into this expression, and adding it to Eq. 5.13, we find that the mixing between $W_\mu^{\pm(n)}$ and $W^{\pm 5(n)}$ cancels, and we obtain the mass terms

$$\begin{aligned} S^W + S^W_{gf} &= \int d^4x \Big\{ M_W^2 W_\mu^{+(0)} W^{-\mu(0)} - M_W^2 \phi^{+(0)}\phi^{-(0)} \\ &+ \sum_{n=1}^{\infty} \Big[m_{W,n}^2 W_\mu^{+(n)} W^{-\mu(n)} - m_{W,n}^2 W^{+5(n)} W^{-5(n)} \\ &- m_{W,n}^2 \phi^{+(n)}\phi^{-(n)} \Big] \Big\} \ . \end{aligned} \tag{5.15}$$

Again, the Goldstone modes are linear combinations of the 5-dimensional components of the gauge fields, $W^{\pm 5(n)}$, and the KK excitations of the zero mode Goldstone, $\phi^{\pm(n)}$:

$$G^{\pm(n)} = \frac{m_n W^{\pm 5(n)} \mp i M_W \phi^{\pm(n)}}{\sqrt{m_n^2 + M_W^2}} \ . \tag{5.16}$$

The physical charged Higgs pair is the orthogonal combination:

$$H^{\pm(n)} = \frac{m_n \phi^{\pm(n)} \mp i M_W W^{\pm 5(n)}}{\sqrt{m_n^2 + M_W^2}} \ . \tag{5.17}$$

In the 5-dimensional generalization of the SM Feynman gauge we employ, the fields $W^{\pm\mu(n)}$, $G^{\pm(n)}$, and $H^{\pm(n)}$ share the common mass $m_{W,n}$.

Having computed the spectrum of states in the gauge sector, we can now derive the interactions of the gauge and scalar particles; we identify the 4-dimensional couplings as $\lambda = \lambda_5/2\pi R$, $\lambda^t = \lambda_5^t/\sqrt{2\pi R}$, and $g^i = g_5^i/\sqrt{2\pi R}$ so that the zero mode interactions match those of the SM. Letting $\phi_i^{(n)}$ denote a KK excitation of an arbitrary SM field, the contributing KK interactions take the form

$$\phi_i^{(0)}\phi_j^{(n)}\phi_k^{(n)} \ , \quad \phi_i^{(0)}\phi_j^{(0)}\phi_k^{(n)}\phi_l^{(n)} \ . \tag{5.18}$$

The explicit expressions for these vertices are simple to obtain; for every SM vertex $\phi_i^{(0)}\phi_j^{(0)}\phi_k^{(0)}$ or $\phi_i^{(0)}\phi_j^{(0)}\phi_k^{(0)}\phi_l^{(0)}$, there is a corresponding KK vertex with exactly the same coupling strength. We note explicitly that the $h^{(0)}W^{+(n)}W^{-(n)}$ and $h^{(0)}Z^{(n)}Z^{(n)}$ vertices are identical to the $h^{(0)}W^{+(0)}W^{-(0)}$ and $h^{(0)}Z^{(0)}Z^{(0)}$ vertices; the masses that appear in the KK interactions are M_W and M_Z, not $m_{W,n}$ and $m_{Z,n}$. The heavy

KK states decouple from the processes considered here, allowing us to obtain finite results in five dimensions when the sum over KK modes is performed. The only other interactions needed for our calculation are those involving $W^{\pm 5(n)}$, which are simple to obtain. For a complete list of the SM vertices we refer the reader to [68].

We now derive the interactions of the top quark KK states required in our analysis. Although there is no mixing between different levels of the top quark KK tower, the doublet and singlet states within each level mix. The mass matrix for the nth KK level arising from the reduction of Eq. 5.1 is

$$\left(\bar{Q}_L^{(n)}\,,\ \bar{t}_L^{(n)}\right)\begin{pmatrix} m_n & m_t \\ m_t & -m_n \end{pmatrix}\begin{pmatrix} Q_R^{(n)} \\ t_R^{(n)} \end{pmatrix} + \text{h.c.}\ , \tag{5.19}$$

where m_t is the zero mode top quark mass. This can be diagonalized with the following unitary matrices for the left and right-handed fields:

$$U_L^{(n)} = \begin{pmatrix} \cos(\alpha^{(n)}/2) & \sin(\alpha^{(n)}/2) \\ \sin(\alpha^{(n)}/2) & -\cos(\alpha^{(n)}/2) \end{pmatrix}\ ,\quad U_R^{(n)} = \begin{pmatrix} \cos(\alpha^{(n)}/2) & \sin(\alpha^{(n)}/2) \\ -\sin(\alpha_{(n)}/2) & \cos(\alpha^{(n)}/2) \end{pmatrix}\ , \tag{5.20}$$

where both states in the physical basis have mass $m_{t,n} = \sqrt{m_n^2 + m_t^2}$, and $\cos(\alpha^{(n)}) = m_n/m_{t,n}$, $\sin(\alpha^{(n)}) = m_t/m_{t,n}$. We must derive the couplings of these states to $h^{(0)}$, $A_\mu^{(0)}$, $Z_\mu^{(0)}$, and $g_\mu^{(0)}$ for our analysis. Denoting the mass eigenbasis of the nth level by the vector $T^{(n)}$, we find the following KK interactions:

$$\begin{aligned} S^t \;=\; & \int d^4x \sum_{n=1}^{\infty} \Big\{ \bar{T}^{(n)} \not{A}^{(0)} C_A^{(n)} T^{(n)} + \bar{T}^{(n)} \not{Z}^{(0)} C_{Z,V}^{(n)} T^{(n)} + \bar{T}^{(n)} \not{g}^{(0)} C_g^{(n)} T^{(n)} \\ & + \Big[h^{(0)} \bar{T}^{(n)} C_h^{(n)} T^{(n)} + \text{h.c.} \Big] \Big\}\ . \end{aligned} \tag{5.21}$$

The coupling matrices appearing in this expression are

$$\begin{aligned} C_A^{(n)} &= eQ_t \begin{pmatrix} 1 & 0 \\ 0 & 1 \end{pmatrix}\ ,\quad C_{Z,V}^{(n)} = \frac{g}{c_W} \begin{pmatrix} g_v - g_a\cos(\alpha^{(n)}) & 0 \\ 0 & g_v + g_a\cos(\alpha^{(n)}) \end{pmatrix} \\ C_h^{(n)} &= m_t \begin{pmatrix} \sin(\alpha^{(n)}) & \cos(\alpha^{(n)}) \\ -\cos(\alpha^{(n)}) & \sin(\alpha^{(n)}) \end{pmatrix}\ ,\quad C_g^{(n)} = g_3 \begin{pmatrix} 1 & 0 \\ 0 & 1 \end{pmatrix}\ , \end{aligned} \tag{5.22}$$

where Q_t is the top quark charge in units of e, c_W is the cosine of the weak mixing angle, g and g_3 are respectively the coupling constants of $SU(2)_L$ and $SU(3)_c$, and g_v, g_a are the top quark vector and axial couplings to the SM Z. The γ^5 component of the Z interaction does not contribute to the studied processes, and has consequently not been included. We note that the coupling of top quark KK states to the Higgs is proportional to m_t, not $m_{t,n}$; the heavy KK top quarks decouple as do the $W^{\pm(n)}$ and $Z^{(n)}$ towers. This is in contrast to the behavior of a heavy fourth generation quark, whose coupling to the Higgs is proportional to its mass, and which does not decouple.

We now possess the tools required to study corrections to Higgs boson production and decay processes arising from one loop KK exchanges. We will concentrate on the processes $gg \to h$, $h \to \gamma\gamma$, and $h \to \gamma Z$, which occur at one loop in the SM; the KK contributions to these interactions are therefore of the same order as the SM contributions. The decoupling of the higher KK modes allows us to obtain finite predictions when only one extra dimension is considered; furthermore, at one loop graviton exchanges do not contribute to these processes, rendering our neglect of the gravity sector of the theory justifiable. These features allow us to obtain unambiguous and testable predictions.

5.3 KK Effects in One Loop Higgs Processes

We now study the effects of virtual KK exchanges in $gg \to h$, $h \to \gamma\gamma$, and $h \to \gamma Z$, processes relevant for Higgs production and decay at the LHC. Both the SM and KK contributions to these interactions occur at one loop, and we therefore expect the modifications arising from KK exchanges to be significant. This is indeed the case; we will find that KK effects are visible for the compactification mass m_1 in the range $400\,\mathrm{GeV} \leq m_1 \leq 1500\,\mathrm{GeV}$, a region consistent with the constraints arising from both direct searches and precision measurements [15].

5.3.1 $gg \to h$

The process $gg \to h$ proceeds in the SM through diagrams containing fermion triangle loops. We consider only contributions arising from the top quark and its KK tower;

the couplings of other fermions to the Higgs are much smaller than that of the top quark, and are negligible in our analysis. The production cross section, which is proportional to the $h \to gg$ width, can be written in the form

$$\sigma_{gg\to h} = \frac{G_F\left[\alpha_s(m_H)\right]^2}{32\sqrt{2}\pi m_H^4}|F_t|^2 \ , \tag{5.23}$$

where G_F is the Fermi constant, $\alpha_s(m_H)$ is the QCD coupling strength evaluated at the Higgs mass scale, and F_t is the contribution of the loop integrals over the top quark KK tower contributions. Introducing the abbreviation

$$C_0(m^2) = C_0(m_H^2, 0, 0; m^2, m^2, m^2) \tag{5.24}$$

for the three-point scalar Passarino-Veltman function [68, 141], the SM result becomes

$$F_t^{SM} = -2m_t^2 + m_t^2\left(m_H^2 - 4m_t^2\right)C_0(m_t^2) \ . \tag{5.25}$$

The scalar three-point function of Eq. 5.24 can be evaluated in terms of elementary functions, yielding

$$C_0(m^2) = \begin{cases} -\frac{2}{m_H^2}\left[\arcsin\left(\frac{1}{\sqrt{\tau}}\right)\right]^2 & \tau \geq 1 \\ \\ \frac{1}{2m_H^2}\left[\ln\left(\frac{1+\sqrt{1-\tau}}{1-\sqrt{1-\tau}}\right) - i\pi\right]^2 & \tau < 1 \end{cases} \ , \tag{5.26}$$

where $\tau = 4m^2/m_H^2$. The couplings of the top quark KK excitations to both zero mode Higgs bosons and photons are given in Eq. 5.22; utilizing these expressions, we can write $F_t = F_t^{SM} + F_t^{KK}$, where

$$F_t^{KK} = 2\,m_t \sum_{n=1}^{\infty} m_{t,n}\sin(\alpha^{(n)})\left\{-2 + \left(m_H^2 - 4m_{t,n}^2\right)C_0(m_{t,n}^2)\right\} \ . \tag{5.27}$$

In obtaining this formula, and other formulae presented in this paper, we used QGRAF [139] to check that we included all the appropriate diagrams and FORM [164] to verify our algebraic manipulations. In the limit $m^2 \to \infty$, $C_0(m^2) \approx -1/2m^2 -$

$m_H^2/24m^4$. Applying this result to F_t^{KK}, we find that

$$F_t^{KK} \approx -\frac{2m_H^2 m_t^2}{3}\sum_{n=1}^{\infty}\frac{1}{m_n^2} \tag{5.28}$$

in the limit that the KK mass parameters m_n are much larger than either m_t or m_H. In five dimensions this sum is over a single index n, and we obtain a convergent result. In greater than five dimensions we must sum over an array of indices n_i, where i ranges over the number of extra dimensions, and F_t^{KK} diverges (in more than five dimensions there is also a greater multiplicity of states arising from the KK reduction [48], which affects both the finite piece and the coefficient of the divergent part of the sum). These divergent sums can be evaluated by introducing a cutoff Λ; in six dimensions, for example, this leads to the result $F_t^{KK} \propto \ln(\Lambda R)$. We will not study scenarios with $D > 5$ here; we expect, however, that the results we obtain in the 5-dimensional case will be qualitatively similar to those found in the complete $D > 5$ theory in which these UED are embedded, and in which this arbitrariness is removed.

Since the lower bound on the KK mass parameter m_1 in UED models is quite low, $m_1 \geq 300 - 400$ GeV, we expect the deviations due to the virtual KK exchanges to be large. We present in Fig. 5.1 the fractional deviation of the production cross section from that of the SM for the following choices of compactification mass: $m_1 = 500, 750, 1000, 1250, 1500$ GeV. It was argued in [15] that the 4-dimensional effective theory remains valid until $m_n \approx 10$ TeV. A negligible fraction of the effects found here are induced by KK modes with masses above this value, and we can therefore trust our results for the compactification masses $m_1 \leq 1.5$ TeV considered. Fits to the electroweak precision data within the framework of extra-dimensional models typically allow Higgs masses larger than the 95% CL upper bound obtained in the SM [152]; we therefore present results for the range $m_H \leq 500$ GeV. For $m_1 = 500$ GeV and $m_H \approx 120$ GeV, the production rate is $\approx 85\%$ larger than in the SM; this decreases to 40% for a 500 GeV Higgs. For $m_1 = 1500$ GeV and $m_H \approx 120$ GeV the increase is $\approx 10\%$. A more complete analysis would take into account the next-to-leading order QCD corrections, which significantly increase $\sigma_{gg\to h}$ [66, 75], and the next-to-next-to-leading order QCD corrections in the $m_t \to \infty$ limit, which have recently been computed [10, 101]. However, the KK contributions will receive the same QCD corrections, and we expect that for $m_1 \leq 1.5$ TeV and a light Higgs boson, deviations arising from physics in UED should be observable. Future e^+e^- linear colliders will determine the $h \to gg$ decay width with a $10\% - 12.5\%$ precision for Higgs masses in the range $120 - 140$ GeV [2], indicating that compactification masses $m_1 \leq 1500$ GeV are indeed testable.

We will examine the observability of UED contributions at future colliders in more detail in the following subsections, where we compute the corresponding deviations arising from KK exchanges in the decays $h \to \gamma\gamma$ and $h \to \gamma Z$. This will allow us to estimate the total shift in production rates for the processes $gg \to \gamma\gamma, \gamma Z$, which are relevant for Higgs searches at the LHC.

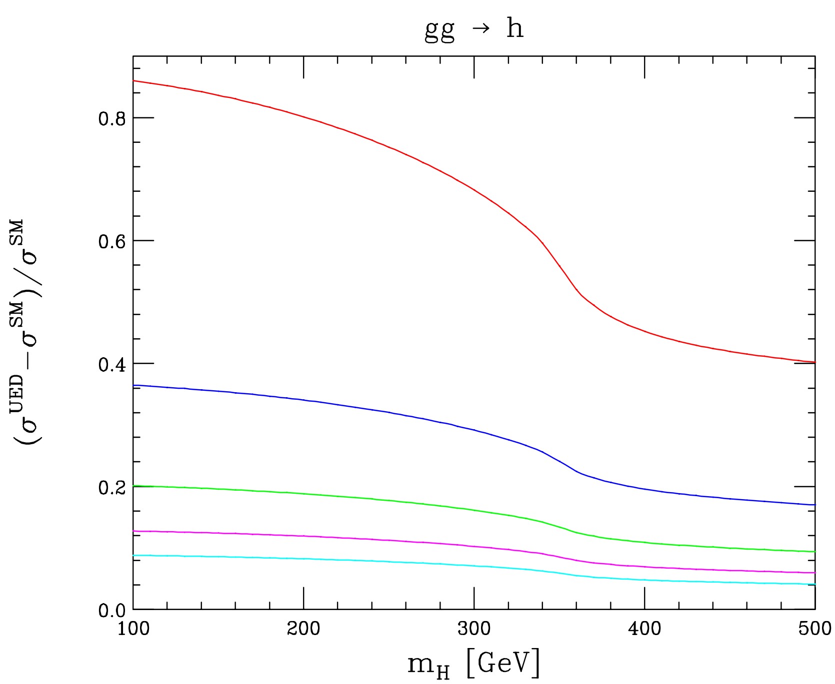

Figure 5.1: The fractional deviation of the $gg \to h$ production rate in the UED model as a function of m_H; from top to bottom, the results are for $m_1 = 500, 750, 1000, 1250, 1500$ GeV.

5.3.2 $h \to \gamma\gamma$

We now study the decay $h \to \gamma\gamma$, which is the primary discovery mode at the LHC for a Higgs with mass $m_H \leq 150$ GeV. At one loop, this process proceeds through both top quark and gauge sector loops, with the latter involving the $W^{\pm}$ tower and its associated Goldstone modes and ghosts. The decay width can be written as

$$\Gamma_{h\to\gamma\gamma} = \frac{G_F \alpha^2}{8\sqrt{2}\pi^3 m_H} |F|^2 \ , \tag{5.29}$$

where α is the electromagnetic coupling, and $F = F_W + 3Q_t^2 F_t$. The SM result for F_t^{SM} is given in Eq. 5.25, and

$$F_W^{SM} = \frac{1}{2} m_H^2 + 3M_W^2 - 3M_W^2 \left(m_H^2 - 2M_W^2 \right) C_0(M_W^2) \ . \tag{5.30}$$

In the UED model there are additional contributions from the top quark KK tower, the $W^{\pm}$ tower and its associated Goldstone modes, ghost KK states, and the $H^{\pm}$ tower defined in Eq. 5.17. We set $F_t = F_t^{SM} + F_t^{KK}$ and $F_W = F_W^{SM} + F_G^{KK}$, with F_t^{KK} denoting the top quark KK tower contribution and F_G^{KK} including the contributions of the KK excitations in the gauge and Higgs sectors. F_t^{KK} is then given by the expression in Eq. 5.27, and

$$F_G^{KK} = \sum_{n=1}^{\infty} \left\{ \frac{1}{2} m_H^2 + 4M_W^2 - \left[4M_W^2 \left(m_H^2 - 2m_{W,n}^2 \right) - m_H^2 m_{W,n}^2 \right] C_0(m_{W,n}^2) \right\} \ . \tag{5.31}$$

Using the expansion $C_0(m^2) \approx -1/2m^2 - m_H^2/24m^4$, it is simple to check that this sum converges in five dimensions. However, it diverges for $D > 5$, as does the $gg \to h$ production cross section. We again expect that the results we obtain will be qualitatively similar for $D > 5$ when the cutoff dependence is fixed by a more complete theory.

The interference between the SM and KK contributions is more intricate in $h \to \gamma\gamma$ than in $gg \to h$, as thresholds exist at both $2M_W$ and $2m_t$ where the relative importance of the various contributions can change. The fractional deviation of the $h \to \gamma\gamma$ decay width is shown in Fig. 5.2 for five choices of m_1, and the fractional deviations due to the top quark KK tower and the gauge and Higgs tower contributions are presented separately for $m_1 = 500$ GeV in Fig. 5.3. The $\gamma\gamma$ decay width in the UED model is $\approx 12\%$ smaller than in the SM for $m_H \leq 2M_W$ and $m_1 = 500$ GeV, the Higgs mass region in which this decay is expected to be the discovery mode at the LHC; this result drops to $\approx 4\%$ for $m_1 = 1000$ GeV. However, at $m_H \approx 2m_t$ the decay width in the UED scenario becomes larger than in the SM. The relevant contributions of the top quark and gauge sector KK towers are shown in Fig. 5.3. The contribution of the top quark KK tower, the dominant UED term, interferes destructively with the SM result below the $2m_t$ threshold; this behavior reverses above threshold.

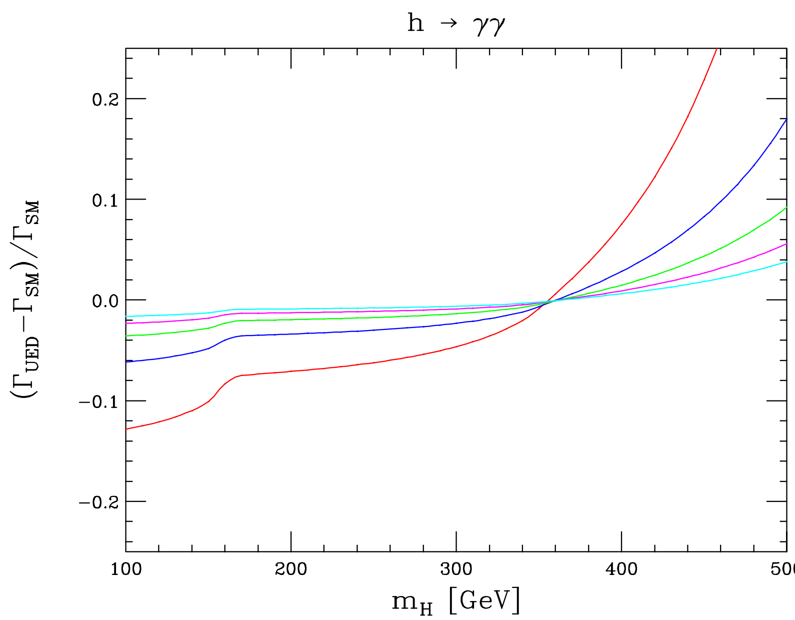

Figure 5.2: The fractional deviation of the $h \to \gamma\gamma$ decay width in the UED model as a function of m_H; from top to bottom on the right, the results are for $m_1 = 500, 750, 1000, 1250, 1500$ GeV.

To determine the sensitivity of the LHC to these effects, we must compute the net shift in the $\gamma\gamma$ production rate resulting from the deviations in both $gg \to h$ and $h \to \gamma\gamma$. For resonant production of the Higgs, the $\gamma\gamma$ signal is well approximated by taking $\sigma_{gg\to h} \times \Gamma_{h\to\gamma\gamma}$, including the parton density functions evaluated at the relevant scale, and multiplying by the appropriate prefactors. The fractional deviation in the

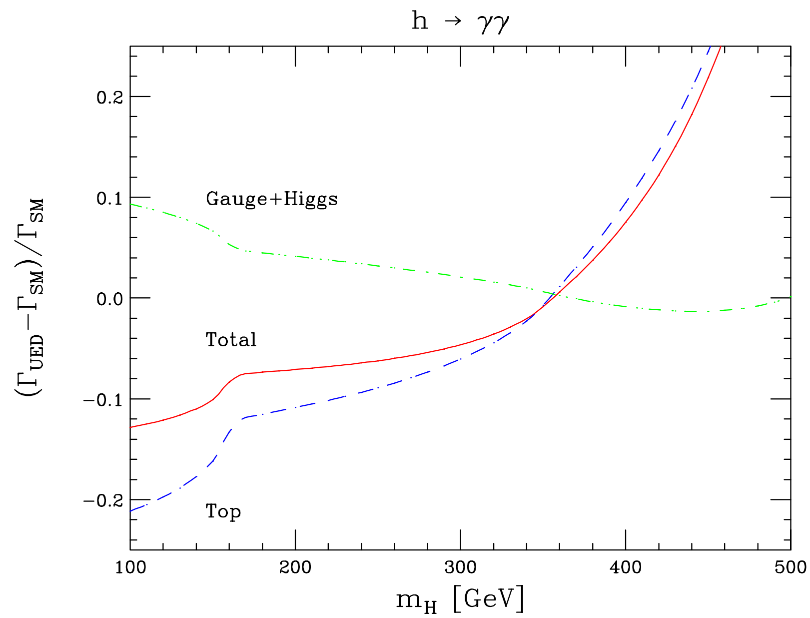

Figure 5.3: The fractional deviation of the $h \to \gamma\gamma$ decay width for $m_1 = 500$ GeV as a function of m_H, with the contributions of the top quark sector and the gauge and Higgs sectors shown separately.

$\gamma\gamma$ production rate is presented in Fig. 5.4 for five choices of m_1. For $m_H \leq 150$ GeV, the region of interest at the LHC, the increase in $\sigma_{gg\to h}$ and the decrease in $\Gamma_{h\to\gamma\gamma}$ yield a total $\approx 10\% - 65\%$ increase in the total rate as m_1 is varied from 1250 GeV to 500 GeV, respectively. The LHC is expected to be sensitive to this rate at the $10\% - 15\%$ level [167]; consequently, we expect signals from UED to be visible if $m_1 \leq 1000 - 1250$ GeV. An independent measurement of the $h \to \gamma\gamma$ decay width will be achievable at future linear colliders; for $m_h \leq 150$ GeV, a measurement of the $h\gamma\gamma$ coupling at the $7\% - 10\%$ level will be possible [2]. This will provide a test of UED models with $m_1 \leq 800$ GeV. A measurement of the $h \to \gamma\gamma$ width with an accuracy of $\approx 2\%$ is possible with the proposed photon collider option of future e^+e^- colliders [28]; this would allow probes of the UED model with KK mass parameter $m_1 \leq 1500$ GeV.

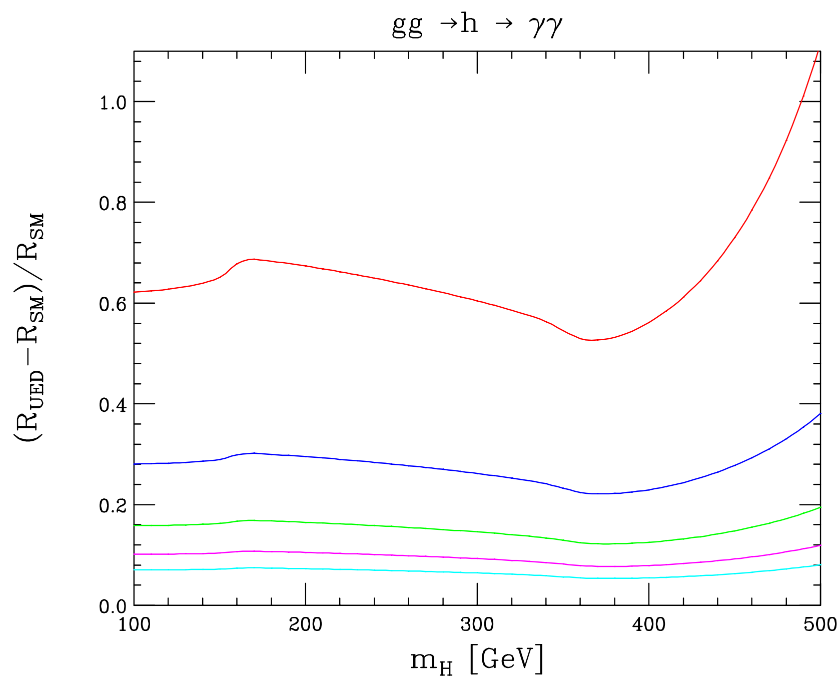

Figure 5.4: The fractional deviation of $R = \sigma_{gg\to h} \times \Gamma_{h\to\gamma\gamma}$, the $\gamma\gamma$ production rate, in the UED model as a function of m_H; from top to bottom, the results are for $m_1 = 500, 750, 1000, 1250, 1500$ GeV.

5.3.3 $h \to \gamma Z$

We examine here the decay $h \to \gamma Z$, which proceeds in the SM through top quark and gauge sector loops. Although the width of this process exceeds the $h \to \gamma\gamma$ width for Higgs masses in the range $m_H \geq 130$ GeV, the single photon and need to demand a leptonic Z decay for reconstruction purposes render it less interesting at the LHC. However, since it potentially provides another test of the detailed properties of the Higgs boson, we study modifications of this decay arising from physics in UED.

The decay width can be expressed as

$$\Gamma_{h\to\gamma Z} = \frac{\alpha G_F^2 M_W^2 m_H^3 s_W^2}{64\pi^4}\left(1 - \frac{M_Z^2}{m_H^2}\right)^3 |F|^2 \ , \tag{5.32}$$

where s_W is the sine of the weak mixing angle. We introduce the abbreviation

$$\begin{aligned} C_2(m^2) &= C_1(m_H^2, M_Z^2, 0; m^2, m^2, m^2) + C_{11}(m_H^2, M_Z^2, 0; m^2, m^2, m^2) \\ &\quad + C_{12}\left(m_H^2, M_Z^2, 0; m^2, m^2, m^2\right) \ , \end{aligned} \tag{5.33}$$

where C_1, C_{11}, and C_{12} are the Passarino-Veltman tensor coefficients defined in [68], and change slightly our shorthand notation for the scalar three-point function:

$$C_0(m^2) = C_0(m_H^2, M_Z^2, 0; m^2, m^2, m^2) \ . \tag{5.34}$$

These can be evaluated in terms of elementary functions [74]; setting $\tau_Z = 4m^2/M_Z^2$ and $\tau_H = 4m^2/m_H^2$, we have

$$\begin{aligned} 4m^2 C_2(m^2) &= \frac{\tau_Z \tau_H}{2(\tau_Z - \tau_H)} + \frac{\tau_Z \tau_H^2}{2(\tau_Z - \tau_H)^2}\left\{\tau_Z\left[f(\tau_Z) - f(\tau_H)\right]\right. \\ &\quad \left. + 2\left[g(\tau_Z) - g(\tau_H)\right]\right\} \ , \\ 4m^2 C_0(m^2) &= \frac{2\tau_Z\tau_H}{\tau_Z - \tau_H}\left[f(\tau_Z) - f(\tau_H)\right] \ , \end{aligned} \tag{5.35}$$

where

$$f(\tau) = \begin{cases} \left[\arcsin\left(\frac{1}{\sqrt{\tau}}\right)\right]^2 & \tau \geq 1 \\ -\frac{1}{4}\left[\ln\left(\frac{1+\sqrt{1-\tau}}{1-\sqrt{1-\tau}}\right) - i\pi\right]^2 & \tau < 1 \end{cases} \ , \tag{5.36}$$

and

$$g(\tau) = \begin{cases} \sqrt{\tau - 1}\,\arcsin\left(\frac{1}{\sqrt{\tau}}\right) & \tau \geq 1 \\ \\ \frac{1}{2}\sqrt{1-\tau}\left[\ln\left(\frac{1+\sqrt{1-\tau}}{1-\sqrt{1-\tau}}\right) - i\pi\right] & \tau < 1 \end{cases} . \tag{5.37}$$

Writing

$$F = \cot(\theta_W) F_W + 3\frac{g_v Q_t}{s_W c_W} F_t \ , \tag{5.38}$$

where θ_W is the weak mixing angle, the SM result becomes

$$\begin{aligned} F_t^{SM} &= 4\, m_t^2 \left\{ 4C_2(m_t^2) + C_0(m_t^2) \right\} \\ F_W^{SM} &= 4 \Big\{ -M_W^2 \left(3C_0(M_W^2) + 5C_2(M_W^2)\right) - \frac{1}{2} m_H^2 C_0(M_W^2) \\ &\quad + s_W^2 \left[M_W^2 \left(6C_2(M_W^2) + 4C_0(M_W^2)\right) + m_H^2 C_2(M_W^2) \right] \Big\} . \end{aligned} \tag{5.39}$$

In our notation, $g_v = I_3/2 - s_W^2 Q_t$, where I_3 is the third component of the top quark weak isospin. In the UED model, there are additional contributions from both the top quark KK tower and the gauge sector KK excitations; partitioning these pieces as in the $h \to \gamma\gamma$ case, $F_t = F_t^{SM} + F_t^{KK}$ and $F_W = F_W^{SM} + F_G^{KK}$, we find

$$\begin{aligned} F_t^{KK} &= 8 \sum_{n=1}^{\infty} \left\{ m_t\, m_{t,n} \sin(\alpha^{(n)}) \left[4C_2(m_{t,n}^2) + C_0(m_{t,n}^2) \right] \right\} \\ F_G^{KK} &= 4 \sum_{n=1}^{\infty} \Big\{ -M_W^2 \left(3C_0(M_W^2) + 7C_2(M_W^2)\right) - \frac{1}{2} m_H^2 C_0(M_W^2) \\ &\quad + s_W^2 \left[M_W^2 \left(8C_2(M_W^2) + 4C_0(M_W^2)\right) + m_H^2 C_2(M_W^2) \right] \Big\} . \end{aligned} \tag{5.40}$$

We have used the couplings given in Eq. 5.22 in deriving these results. It can be checked that these sums converge in $D = 5$, but diverge for $D > 5$; again, we concentrate on the $D = 5$ scenario.

We present the fractional deviation of $\Gamma_{h\to\gamma Z}$ in the UED model in Fig. 5.5 for five choices of the KK mass parameter m_1, and show the relative contributions of the top quark and gauge sectors in Fig. 5.6. The decay width in the UED model is slightly larger than the SM width for $m_H \leq 275$ GeV, and slightly smaller for higher values of m_H. The top quark and gauge sector KK towers have contributions with approximately equal magnitude but opposite sign, as seen in Fig. 5.6, and their effects tend to cancel. For all m_H and m_1 considered the deviation is $\leq 10\%$, and is hence smaller than the modifications to the gg and $\gamma\gamma$ widths. An effect of this magnitude is possibly observable at future linear colliders, although a detailed analysis of this decay mode has not been performed; it is also possible that such an effect could be observed in the $\gamma\gamma$ collision option of future colliders.

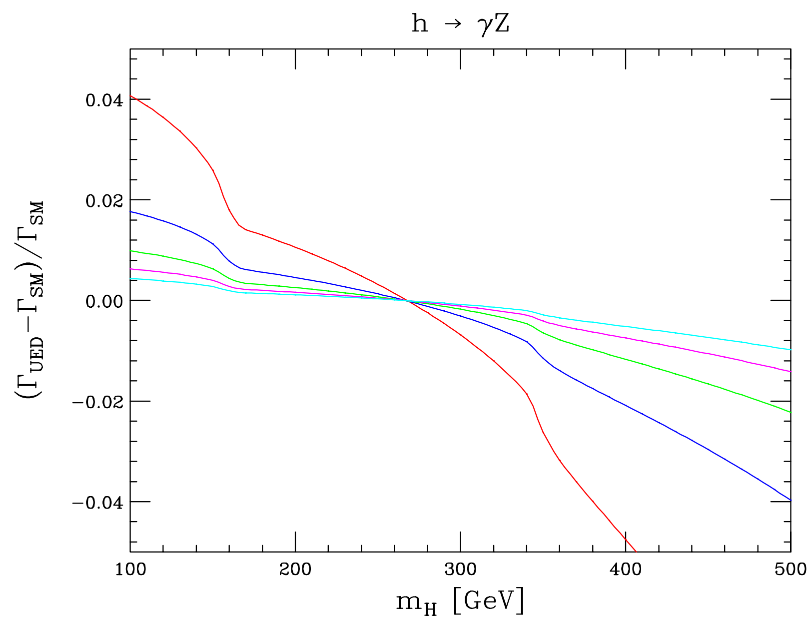

Figure 5.5: The fractional deviation of the $h \to \gamma Z$ decay width in the UED model as a function of m_H; from top to bottom on the left, the results are for $m_1 = 500, 750, 1000, 1250, 1500$ GeV.

The fractional deviation of the γZ production rate at the LHC via $gg \to h \to \gamma Z$ is shown in Fig. 5.7 for five choices of m_H. The production increase is $\approx 95\%$ for $m_H \leq 150$ GeV and $m_1 = 500$ GeV, and $\approx 20\%$ for $m_1 = 1000$ GeV. This shift is caused primarily by the $gg \to h$ deviation; however, it may render this decay mode visible above the background at the LHC. Again, a detailed analysis of this decay at the LHC has not been performed.

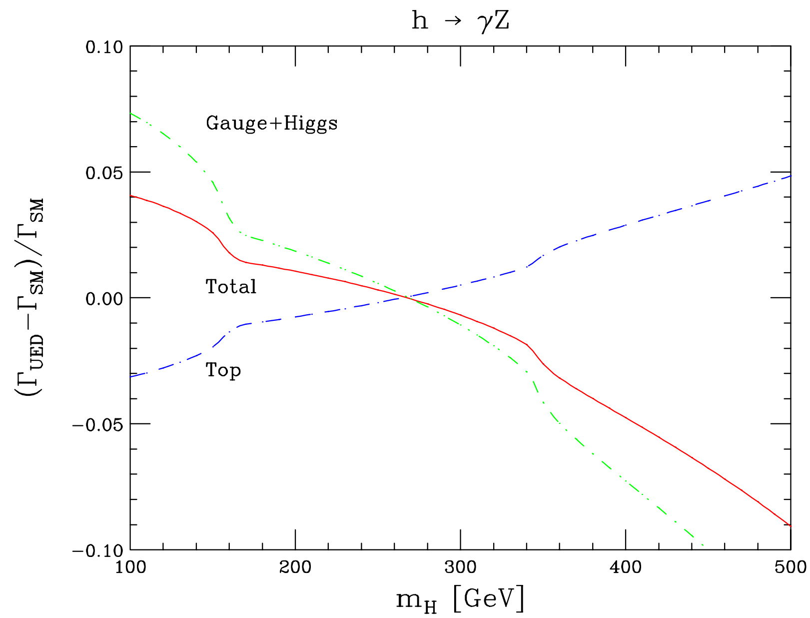

Figure 5.6: The fractional deviation of the $h \to \gamma Z$ decay width for $m_1 = 500$ GeV as a function of m_H, with the contributions of the top quark sector and the gauge and Higgs sectors shown separately.

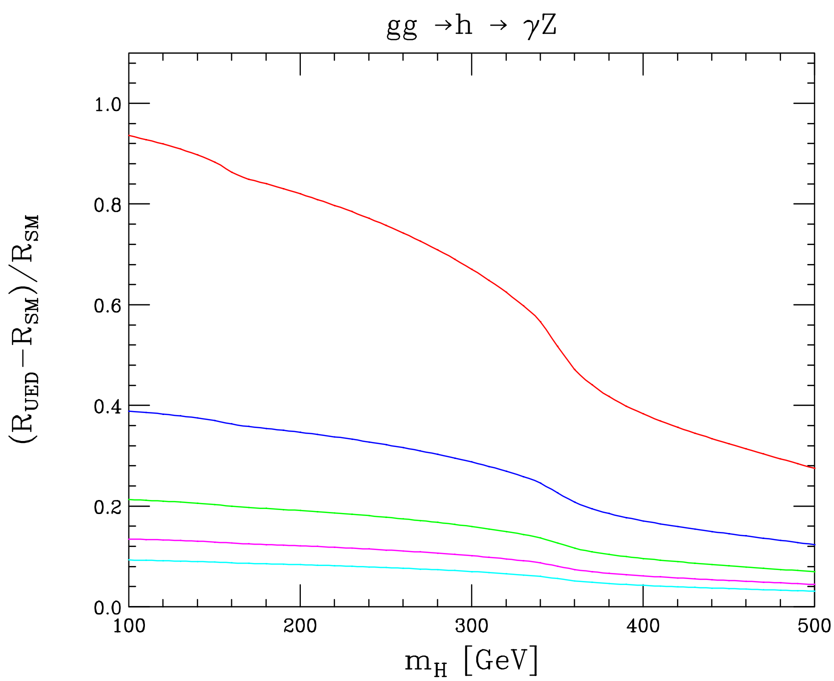

Figure 5.7: The fractional deviation of $R = \sigma_{gg\to h} \times \Gamma_{h\to\gamma Z}$, the γZ production rate, in the UED model as a function of m_H; from top to bottom, the results are for $m_1 = 500, 750, 1000, 1250, 1500$ GeV.

5.4 Summary

We have studied the virtual effects of KK excitations in UED on Higgs production and decay processes relevant for high energy experiments at the LHC and at future linear colliders. The heavy KK modes decouple, allowing us to obtain unambiguous predictions for one extra dimension. For two or more extra dimensions the KK mode sums diverge, and while we expect our results in these scenarios to be qualitatively similar to those obtained here, we cannot make precise predictions. We have found that the KK excitation contributions can be quite significant; the $gg \to h$ production rate can be $\approx 85\%$ larger than the SM result for $m_H \leq 150$ GeV and KK mass parameter $m_1 = 500$ GeV, a value allowed by current constraints. For $m_1 \approx 1500$ GeV, the rate increase is $\approx 10\%$; assuming the SM theoretical prediction is under control by the time the LHC turns on, this should be an observable shift. The corresponding deviations in the $h \to gg$ decay width can be probed at future e^+e^- colliders, allowing compactification masses in the range $m_1 \leq 1500$ GeV to be tested. The width of the decay $h \to \gamma\gamma$, the primary discovery mode for a Higgs with mass $m_H \leq 150$ GeV at the LHC, is decreased relative to the SM prediction by $\approx 12\%$. The total $\gamma\gamma$ production rate is increased by $\approx 10\% - 65\%$ for $1250 \geq m_1 \geq 500$ GeV when the reaction $gg \to h \to \gamma\gamma$ relevant at the LHC is considered. With the $10\% - 15\%$ accuracy expected in the determination of this rate at the LHC, compactification masses $m_1 \leq 1250$ GeV can be probed. The $h \to \gamma\gamma$ width can be independently measured at future e^+e^- and $\gamma\gamma$ colliders; we expect the effects from compactification masses $m_1 \leq 800$ GeV to be observable with the $7\% - 10\%$ precision expected at e^+e^- colliders, and from masses $m_1 \leq 1500$ GeV to be testable with the 2% precision expected at $\gamma\gamma$ colliders. Finally, we have examined the deviations in the decay $h \to \gamma Z$ predicted by UED models. We have found that the deviations from the SM result are less than $\approx 10\%$ throughout the m_H, m_1 region studied. However, the process $gg \to h \to \gamma Z$ is expected to increase by $\approx 20\% - 95\%$ for compactification masses in the range $1000 \geq m_1 \geq 500$ GeV. No detailed study of this process has been performed for either the LHC or future linear colliders; however, the production increase at the LHC is possibly visible above background.

How do these results compare with the deviations induced in other new physics models? In the Randall-Sundrum model studied in [103], where the Higgs and radion fields mix, both $\Gamma_{h\to gg}$ and $\Gamma_{h\to\gamma\gamma}$ are decreased throughout the allowed parameter space; the total Higgs production rate can be decreased to $\leq 1\%$ of the SM value for a large range of Higgs-radion mixing strengths. These results for $\Gamma_{h\to gg}$ are the opposite of those found here, in which the width is increased throughout the allowed parameter space. The situation is murkier in the Minimal Supersymmetric Standard Model (MSSM), as a large number of parameters enter calculations at the one loop level. A detailed study of Higgs physics in the MSSM was performed in [41]. Typically, $\Gamma_{h\to gg}$ is decreased by $\leq 15\%$ throughout the allowed parameter space, while $\Gamma_{h\to\gamma\gamma}$ is shifted by $\leq 5\%$, with the direction of the shift parameter dependent. Again, the deviation in $\Gamma_{h\to gg}$ is opposite that found here. $\Gamma_{h\to gg}$ was also studied in [37] within a supersymmetric extra-dimensional scenario [29]. In this model, $\Gamma_{h\to gg}$ receives contributions from loops of both top and stop KK excitations; the localization of fermion Yukawa couplings at orbifold fixed points induces mixing within these KK towers. The width is decreased relative to its SM value throughout the entire parameter space; for a Higgs with $m_H \approx 120$ GeV the width is $\leq 25\%$ of the SM result. This is again opposite the shift found here. The effects of any of these scenarios on Higgs physics should therefore be distinguishable from the shifts found in the UED model studied here; the direct production of the various new states associated with each model should also assist in distinguishing them.

In summary, the virtual effects of KK excitations in UED can significantly alter Higgs properties which will be measured at future colliders. The implications of radiative corrections in extra-dimensional models have not been studied extensively, primarily because of the resulting divergences. We have shown that in certain scenarios such effects are both calculable and important, and we believe that further investigations along these lines should be undertaken.

Chapter 6

The Drell-Yan Rapidity Distribution at Next-to-next-to Leading Order in QCD

6.1 Introduction

In the previous chapters we discussed various forms of new physics which might be uncovered in future collider experiments, and detailed the most promising signatures for their discovery. The success of these searches will require a precise knowledge of the Standard Model backgrounds that can mask the presence of new physics. Predictions for Standard Model rates and differential distributions beyond leading order in perturbation theory are required. In this chapter we discuss the next-to-next-to leading order QCD corrections to the dilepton rapidity distribution in the Drell-Yan process, one of the most important discovery channels for new physics at hadron colliders.

The production of lepton pairs in hadronic collisions, known as the Drell-Yan (DY) process [77], was the first application of parton model ideas beyond deep inelastic scattering. Due to its clean theoretical interpretation and large rates, the DY process has been studied extensively, and will continue to be investigated at both the Tevatron and the LHC. The DY process provides valuable information about partonic structure functions, enables measurements of the masses and decay rates of the W and Z bosons, and furnishes a sensitive test for many varieties of new physics, such as the additional gauge bosons that appear in almost any extension of the Standard Model. It will also be used for the more prosaic purpose of monitoring partonic luminosities at the LHC.

Despite its importance and the significant amount of work devoted to its description, the calculation of higher order QCD corrections to the DY process has proceeded slowly. The next-to-leading order (NLO) QCD corrections to the total cross-section, and the x_F and rapidity distributions, were calculated nearly 25 years ago in Ref. [8]. The NNLO corrections to the total cross-section were obtained eleven years later in [99]. No complete calculation of the NNLO QCD corrections to any differential distribution has ever been performed, although partial results exist in the literature [149].

Recently, the NNLO virtual corrections to several interesting hard scattering processes in QCD have been computed (see, for example, [86] and the references within). The calculation of real emission amplitudes, required for complete NNLO predictions, is still in progress. In their most general form, these computations entail a careful analysis of perturbative multiparticle final states in generic hard scattering events. While it is certainly useful to solve this problem in complete generality, it is also useful to study specific examples, especially those most urgently needed in experimental analyses. It is possible to develop alternative methods of calculation which can be used to compute basic differential distributions. In [9, 10, 11] it was shown how a simple generalization of the optical theorem can be combined with multi-loop computational technology to produce a powerful method for the evaluation of phase-space integrals. In this chapter we present a non-trivial application of these ideas; we analyze the rapidity distribution of the virtual photon produced in the DY process through NNLO in perturbative QCD.

We consider the production of low invariant mass lepton pairs in proton-proton (pp) collisions at relatively small center of mass energies. Such kinematic configurations are being investigated in fixed target experiments. The most recent measurements come from the E866/Nusea collaboration at Fermilab where the dimuon production cross-section in pp and proton-deuteron collisions has been measured at

$\sqrt{s} \approx 40$ GeV for muon invariant masses in the interval $4 - 16$ GeV. These experiments are sensitive to both the $x \to 1$ components of the valence quark distribution functions and to the moderate x components of the sea quark distribution functions of the proton. Both of these kinematic configurations are not very well constrained by other data, and therefore the recent measurements of E866 provide a valuable constraint. The precision of their measurement is approximately 10% per bin; given significant ($\sim 40\%$) NLO corrections at such energies, the complete NNLO computation is required. Although in principle both photon and Z boson exchanges contribute to this process, the Z exchange component is suppressed by M^2/M_Z^2, where M is the invariant mass of the lepton pair. This is an approximately 1% effect for the relevant invariant masses, and will be neglected in our analysis.

This calculation is quite challenging technically. Existing techniques used for computing phase-space integrals are not capable of handling problems of this complexity. We introduce here a powerful new method for performing these calculations. We extend the optical theorem in such a way that the calculation of differential distributions becomes possible using the techniques developed for multi-loop calculations. To achieve this, we represent the rapidity constraint by an effective "propagator". This propagator is constructed so that when the imaginary part of the forward scattering amplitude is computed using the optical theorem, the mass-shell constraint for the "particle" described by this propagator is equivalent to the rapidity constraint in the phase space integration. We then use the methods described in Ref. [10] for the calculation of inclusive cross sections, keeping the fake particle propagator in the loop integrals, and deriving the rapidity distribution as the imaginary part of the forward scattering amplitude.

6.2 Description of the Calculation

The production of lepton pairs in high-energy hadronic collision occurs in two distinct steps; the quarks and gluons from the colliding hadrons first annihilate to create a highly virtual time-like photon, which then decays into a pair of leptons. In the center of mass frame, the two colliding hadrons have the momenta $P_{1,2} = \sqrt{S/2}\,(1, \mathbf{0}_\perp, \pm 1)$. A virtual photon of invariant mass M, produced in the collision, has the momentum

$P_\gamma = (E, \mathbf{p}_\perp, p_z)$. The energy and the momentum of the virtual photon are related by the "mass-shell" condition $E^2 - \mathbf{p}^2 = M^2$. The rapidity of the virtual photon is defined as $Y = \frac{1}{2}\ln\left(\frac{E+p_z}{E-p_z}\right)$.

We first compute the partonic hard scattering cross-sections, and then convolute them with the parton distribution functions of the colliding hadrons. The partonic rapidity distributions for the hard scattering of partons i, j, with momentum $p_1 = x_1 P_1$ and $p_2 = x_2 P_2$ respectively, are obtained by integrating the hard scattering matrix elements over the phase-space of the final state particles with the rapidity and the mass of the virtual photon kept fixed:

$$\frac{\mathrm{d}\sigma_{ij}}{2e^{2Y}\mathrm{dY}} = \int \mathrm{d}\Pi_f |\mathcal{M}_{ij}|^2 \delta\left(e^{2Y} - \frac{E+p_z}{E-p_z}\right). \tag{6.1}$$

We consider the collision of the two partons in the center of mass frame. The rapidity constraint can then be written as

$$\delta\left(e^{2Y} - \frac{E+p_z}{E-p_z}\right) = e^{-2Y}\delta\left(\frac{P_\gamma[p_1 - up_2]}{P_\gamma p_1}\right), \tag{6.2}$$

where we have set $u = \frac{x_1}{x_2}e^{-2Y}$. At leading order in α_s, the production of the virtual photon occurs through the annihilation of a quark anti-quark pair. Only the virtual photon is produced in the collision, rendering the phase-space integrations trivial. At higher orders in α_s, inelastic channels contribute; at $\mathcal{O}(\alpha_s)$, for example, we must also consider both $q\bar{q} \to \gamma^* g$ and $qg \to q\gamma^*$. It is still relatively simple to perform these phase space integrations; however, this approach becomes impractical at higher orders. We adopt instead the alternative method first suggested in Ref. [9], which can be efficiently applied at NNLO.

We first represent the δ-function in Eq. 6.2 as the imaginary part of an effective propagator:

$$\delta(x) \to \frac{1}{2\pi i}\left[\frac{1}{x - i0} - \frac{1}{x + i0}\right]. \tag{6.3}$$

Following the discussion in [10], we then map the constrained phase-space integrals onto forward scattering loop integrals. We denote the difference of propagators with opposite $i0$ prescription, such as that shown in Eq. 6.3, by a cut propagator; final state particles on mass-shell are also represented by cut propagators. The rapidity δ-function constraint becomes, as indicated above, an unconventional propagator linear in the loop momentum.

At NLO, we must consider integrals of the following general form:

$$I(\nu_1, \nu_2, ...\nu_5) = \int \frac{\mathrm{d}^d k}{(2\pi)^d} \frac{1}{A_1^{\nu} ... A^{\nu_5}}, \tag{6.4}$$

where $A_1 = k^2 - M^2 \pm i0$, $\quad A_2 = (k + p_2)^2$, $\quad A_3 = (k + p_1 + p_2)^2 \pm i0, A_4 = (k + p_2)^2$, and $A_5 = k \cdot p_1 - uk \cdot p_2 \pm i0$. The propagators A_1, A_3 and A_5 should be "cut" according to Eq. 6.3, indicating that the corresponding particles are on-shell. The propagators $A_{1..5}$ are linearly dependent; we can therefore eliminate both A_2 and A_4 from the integrand in Eq. 6.4 by partial fractioning. This partial fractioning produces integrals with either ν_1, ν_3 or ν_5 equal to zero. When the cutting rule of Eq. 6.3 is applied, these integral vanish. We find that we can reduce all phase-space integrals of the form of Eq.(6.4) to a single "master" integral, $I(1, 0, 1, 0, 1)$, using only partial fractioning identities. The need to use only partial fractioning relations to perform this reduction is specific to the NLO calculation; we will discuss a more general reduction technique when we consider the NNLO corrections.

We compute the virtual corrections to the leading order production process $q\bar{q} \to \gamma^*$ in the standard fashion, since the rapidity constraint leaves this calculation unaffected. After combining the real and virtual corrections and performing the collinear factorization, we arrive at the LO and NLO results for the partonic rapidity distributions, which we present here for completeness.

We write the partonic differential cross section for the process $i + j \to \gamma^* X$, renormalized in the $\overline{\mathrm{MS}}$ scheme, as

$$(1 - z)\frac{\mathrm{d}\sigma_{ij}}{\mathrm{dY}} = \eta_{ij}^{(0)} + \left(\frac{\alpha}{\pi}\right) \eta_{ij}^{(1)} + \left(\frac{\alpha}{\pi}\right)^2 \eta_{ij}^{(2)} + \mathcal{O}(\alpha_s^3), \tag{6.5}$$

where $\alpha_s = \alpha_s(M)$ is the strong coupling constant assuming n_f massless quark flavors, renormalized at the scale M. The factorization scale is also set equal to M; the dependence on both the renormalization and the factorization scales can be restored by using the renormalization group invariance of the hadronic cross-section.

At the lowest order in α_s, the virtual photon can be produced only in the collision of a quark and antiquark of the same flavor. Therefore,

$$\eta_{ij}^{(0)} = Q_q^2 \left(\delta_{iq}\delta_{\bar{q}j} + \delta_{i\bar{q}}\delta_{qj}\right) \delta(1-z) \left(\delta(y) + \delta(1-y)\right), \tag{6.6}$$

where $z = M^2/s_{\rm part}$, $s_{\rm part}$ is the partonic Mandelstam invariant and $y = (u-z)/(1-z)/(1+u)$.

At NLO, the $q\bar{q}$ channel receives $\mathcal{O}(\alpha_s)$ corrections, and the $q(\bar{q})g$ channel contributes. We find

$$\begin{aligned}
\frac{\eta_{q\bar{q}}^{(1)}}{Q_q^2} &= \Delta(y) \left[\delta(1-z)\left(-\frac{16}{3} + \frac{8\zeta_2}{3}\right)\right. \\
&\left. + \frac{8z^2(1+z^2)}{3(1+z)}\left[2D_1(1-z) - \frac{\ln z}{1-z} + \frac{1-z}{1+z^2}\right]\right] \\
&+ \frac{8}{3}D_0(1-z)T_{00}(y) + \frac{8z(1-z)^3(2y^2+1-2y)}{3(z+1)} \\
&- \frac{8(z^2+1+z^3+2z)}{3(z+1)}T_0(y),
\end{aligned} \tag{6.7}$$

$$\begin{aligned}
\frac{\eta_{qg}^{(1)}}{Q_q^2} &= \delta(y)\left[\frac{z^2(1-2z+2z^2)}{1+z}\ln\frac{(1-z)^2}{z} + \frac{2z^3(1-z)}{1+z}\right] \\
&+ \frac{z^2(-2z+2z^2+1)}{(z+1)}D_0(y) - \frac{(1-z)^4 z y^3}{(z+1)} \\
&+ \frac{z(3z-1)(-1+z)^3 y^2}{(z+1)} - \frac{z(4z-1)(-1+z)^3 y}{(z+1)} \\
&+ \frac{z(-1+z)(2z^3-6z^2+3z-1)}{(z+1)}.
\end{aligned} \tag{6.8}$$

In the above formulae, $D_i(y)$ denotes the standard plus-distribution $[\ln^i(y)/y]_+$, $\Delta(y) = \delta(y(1-y))$, $T_i(y) = D_i(y) + D_i(1-y)$, and $T_{ij}(y) = D_i(y)D_j(1-y)$. NLO results for the other channels can be obtained by permuting partonic labels and changing $y \to 1-y$ in Eqs. 6.7, 6.8.

We now discuss the calculation of the NNLO contributions. The completely virtual correction to the rapidity distribution is the same as the virtual correction to the total cross section, and is straightforward to compute using standard techniques. We compute both the real-virtual and the real-real corrections using the method proposed above. However, at NNLO we must supplement the partial fractioning identities to achieve a complete reduction to master integrals. Our substitution of the rapidity constraint with an effective propagator facilitates the use of integration-by-parts techniques [52, 161], typically used in the reduction of loop integrals. Approximately thirty master integrals are needed in the calculation of the rapidity distribution. The integration-by-parts technology can be also used to construct differential equations satisfied by the master integrals, as demonstrated in [10]. Since we keep the rapidity of the produced photon fixed, the master integrals are functions of both the invariant mass and the rapidity; two first order inhomogeneous partial differential equations can be derived for each integral. These equations can then be solved, and the boundary conditions can be obtained by considering simple kinematic limits.

At NNLO, the following partonic channels contribute: $q\bar{q}$, the scattering of a quark and anti-quark of the same flavor; $q(\bar{q})g$; gg; $q_iq_j(\bar{q}_j)$, the scattering of quarks (anti-quarks) of arbitrary flavor. The complete analytic results for the partonic cross sections are quite lengthy and not illuminating, and will not be presented here.

Integrating the partonic cross-sections over the virtual photon rapidity, we reproduce the $\mathcal{O}(\alpha_s^2)$ correction to the total cross-section computed in Ref. [99]. This provides a strong check on our result.

Finally, we must convolute the renormalized partonic cross-sections with the partonic structure functions to obtain the experimentally measured cross section. We consider the doubly differential cross-section $\mathrm{d}\sigma/\mathrm{d}M\mathrm{d}Y$:

$$\frac{\mathrm{d}\sigma}{\mathrm{d}M\mathrm{d}Y} = \frac{4\pi\alpha^2}{9M^3}\sum_{i,j}\int \mathrm{d}x_1\mathrm{d}x_2 f_i(x_1)f_j(x_2)\frac{\mathrm{d}\sigma_{ij}(z_p,u_p)}{\mathrm{d}Y},$$

where $z_px_1x_2 = x$, $x = M^2/s$, and $u_p = ux_1/x_2$, and α is theelectromagnetic coupling evaluated at the scale M; numerically, $\alpha^{-1} \approx 132$. It is convenient to express the integration over x_1 and x_2 through the partonic variables z and y; doing so, we obtain a representation of the above integral suitable for numerical evaluation. We use the approximate set of NNLO splitting functions described in Ref. [126].

6.3 Numerical Results

In Fig. 6.1, we present the center-of-mass system (CMS) rapidity distribution of an 8 GeV virtual photon produced in pp collisions at $\sqrt{s} \approx 40$ GeV; these parameter values are among those studied in low energy fixed-target experiments. We present the LO, NLO, and NNLO results, with the renormalization and factorization scales both set equal to μ. The bands in the figure indicate the variation of the cross sections between the scale choices $\mu = M/2$ and $\mu = 2M$. It is apparent that the NLO and NNLO distributions become more sharply peaked at central rapidities; this is due primariliy to the evolution of the parton distribution functions beyond leading order. The significant scale dependence of the NLO cross section, which reaches nearly 25% over the interval $M/2 \leq \mu \leq 2M$, is reduced to approximately 10% at NNLO, indicating a reasonable convergence of the perturbative expansion. The magnitude of the NNLO corrections depends upon the choice of μ; typically, they increase the NLO result by approximately 5-15%. We note that the NNLO corrections are drastically reduced for the scale choice $\mu = M/2$. The NNLO corrections computed in the so-called "soft" approximation, which retains only those terms that are singular in the limit $z \to 1$, lead to σ_{NNLO} which is lower than the result of the full calculation by approximately 20%.

We now separate our result into its partonic components. The $q\bar{q}$ and qg pieces contribute the majority of the result; the remaining channels are a factor of 50-100 smaller. The magnitude of the NNLO result is determined by a significant cancellation between the $q\bar{q}$ and qg channels. We illustrate this cancellation by plotting the NNLO contributions of these channels, together with their sum, normalized to the complete NNLO differential cross section in Fig. 6.2. The sum of these channels also contributes a much flatter correction to the rapidity distribution than either piece individually. The qg channel contributes a significant fraction of the complete differential cross-section; combining both the NLO and NNLO qg pieces, we find that they account for about 15% of the complete NNLO result for central rapidities, and nearly 40% for larger ($Y \geq 1$) rapidities. This indicates that the NNLO rapidity distribution is quite sensitive to the gluon content of the colliding protons.

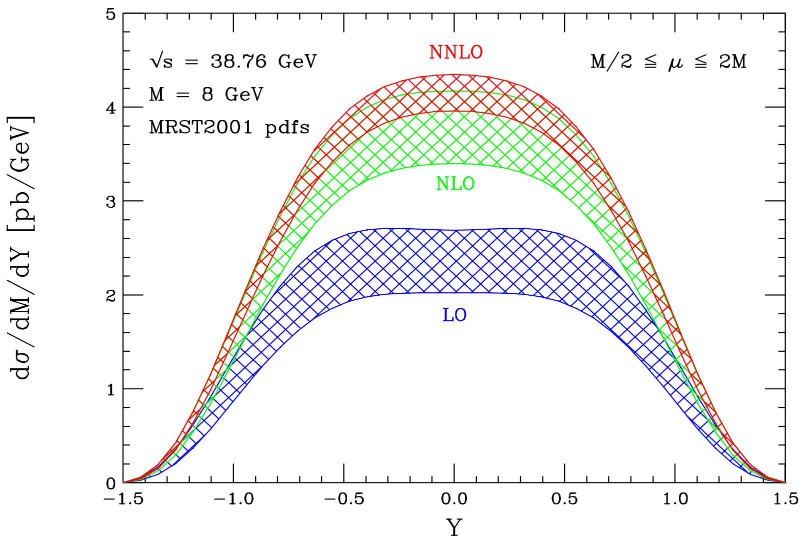

Figure 6.1: The CMS rapidity distribution of the virtual photon produced in proton-proton collisions at LO (lower band), NLO (middle band), and NNLO (upper band), for parameter choices relevent for fixed target experiments. The bands represent the scale dependence of the cross sections; the upper edge of each band denotes the scale choice $\mu = M/2$, while the lower edges indicate the choice $\mu = 2M$.

Finally, we discuss the dependence of the perturbative K-factors upon rapidity. We define the K-factors as follows: $K^{\mathrm{(N)NLO}}(Y) = \sigma^{\mathrm{(N)NLO}}/\sigma^{\mathrm{LO}}$, and $K^{(2)}(Y) = \sigma^{\mathrm{NNLO}}/\sigma^{\mathrm{NLO}}$. We present them in Fig. 6.3. The significant variation of both $K^{\mathrm{NLO}}(Y)$ and $K^{\mathrm{NNLO}}(Y)$ with rapidity, a nearly 25% change from $Y = 0$ to $Y = 1$, illustrates that the LO result provides a poor approximation to the shape of the rapidity distribution, as does the LO result weighted by the NNLO K-factor computed from the inclusive cross section. However, the relative flatness of $K^{(2)}$ indicates that the NLO result does accurately predict the shape of the distribution; the NLO differential cross section weighted by $\sigma^{\mathrm{NNLO}}/\sigma^{\mathrm{NLO}}$, the ratio of NNLO and NLO inclusive cross sections, is valid at these energies to approximately 3-5%. This result appears rather promising, since it suggests a simple and fairly accurate way of incorporating NNLO corrections into NLO Monte Carlo event generators by renormalizing with constant K-factors. It remains to be seen, however, if the same conclusion is valid for other processes or even for the DY process at higher energies.

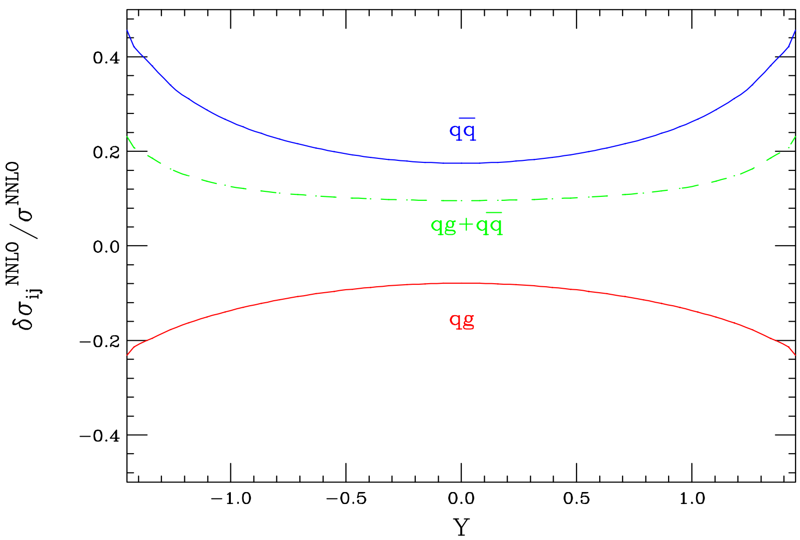

Figure 6.2: The NNLO corrections for the partonic channels $q\bar{q}$ and qg, normalized to the complete NNLO differential cross section. We have again chosen $\sqrt{s} = 38.76$ GeV, $M = 8$ GeV, and $\mu = M$.

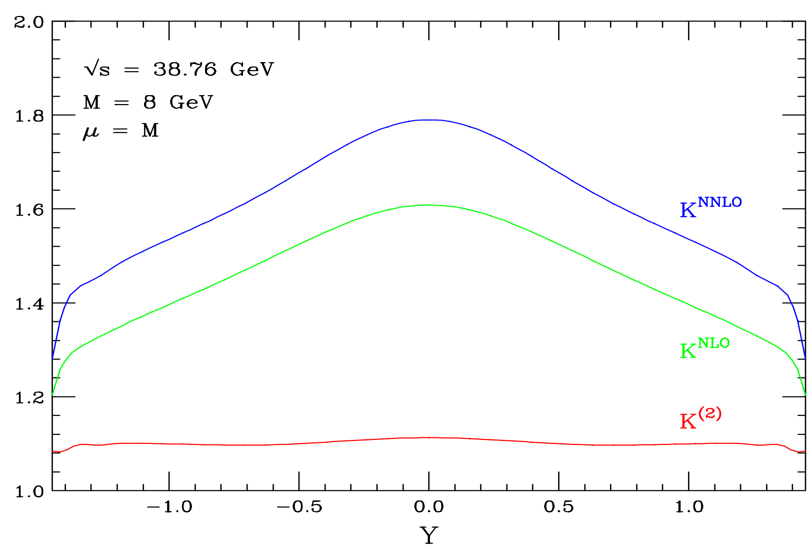

Figure 6.3: The K-factors $K^{\rm NLO}(Y) = \sigma^{\rm NLO}/\sigma^{\rm LO}$, $K^{\rm NNLO}(Y) = \sigma^{\rm NNLO}/\sigma^{\rm LO}$, and $K^{(2)}(Y) = \sigma^{\rm NNLO}/\sigma^{\rm NLO}$. The scale is set equal to the photon invariant mass: $\mu = M$.

6.4 Summary

In conclusion, we have described a calculation of the NNLO QCD corrections to the rapidity distribution in the Drell-Yan process. We have introduced a powerful new method for the calculation of differential quantities in perturbation theory. Although we have presented only a specific example of this technique, it is clear that this method is of more general applicability; the relation between differential distributions and forward scattering amplitudes described above enables the use of multi-loop technology for the calculation of a large class of phase space integrals. We are confident that this technique will be succesfully applied to compute other quantites of phenomenological interest.

Chapter 7

Conclusions

We have discussed several exciting possibilities for TeV-scale physics. Both non-commutativity and extra dimensions are well-motivated ideas that could conceivably be discovered in future experiments. Most importantly, they are *falsifiable* ideas; we have developed definite signatures that can be searched for at upcoming colliders, and have shown that the parameter spaces of these models can be severly restricted, if not completely ruled out. Detailed phenomenological studies of theoretical ideas, such as those performed in this thesis, are vital to the success of the high energy experimental program.

An equally important theoretical task is the precise evaluation of Standard Model predictions for quantities which play a central role in searches for new physics. We have presented here a calculation of the next-to-next-to leading order QCD corrections to the dilepton rapidity distribution in the Drell-Yan process. This production channel is used for several purposes at hadron colliders: (i) as a discovery mode for the new gauge bosons which appear in many extensions of the Standard Model; (ii) as a strong constraint on the parton distribution functions of the proton; (iii) as a partonic luminosity monitor. Our results provide Standard Model predictions at the percent level for this process; this should assist in achieving the percent level accuracy desired for partonic luminosity determinations at the LHC [73, 81], and should improve the next-to-next-to leading order global analysis used to extract parton distribution functions [126].

We are approaching a new frontier in particle physics. Surprising discoveries at the TeV-scale almost certainly await us. New ideas must be explored and old ones refined before we can fully utilize the discovery potential of both existing and planned experiments. Hopefully, the work described in this thesis will contribute to all aspects of meeting the challenge set by our experimental colleagues.

Appendix A

Formulae for $\gamma\gamma$ Collisions

In this appendix we present the SM amplitudes and photon distribution functions relevant for the process $\gamma\gamma \to \gamma\gamma$. For a more detailed discussion the reader is referred to [82, 83, 93, 94].

As discussed in the text, the one loop contributions to $\gamma\gamma \to \gamma\gamma$ arise from W boson and fermion loops. At high energies, which we are considering, there is only one non-negligible independent helicity amplitude. The approximate amplitudes for the W contribution is

$$\frac{\mathcal{M}^{(W)}_{++++}(s,t,u)}{\alpha^2} \approx 12 + 12\left(\frac{u-t}{s}\right)\left[\ln\left(\frac{-u-i\varepsilon}{m_W^2}\right) - \ln\left(\frac{-t-i\varepsilon}{m_W^2}\right)\right]$$
$$+16\left(1-\frac{3tu}{4s^2}\right)\left(\left[\ln\left(\frac{-u-i\varepsilon}{m_W^2}\right) - \ln\left(\frac{-t-i\varepsilon}{m_W^2}\right)\right]^2 + \pi^2\right)$$
$$+16s^2\left[\frac{1}{st}\ln\left(\frac{-s-i\varepsilon}{m_W^2}\right)\ln\left(\frac{-t-i\varepsilon}{m_W^2}\right) + \frac{1}{su}\ln\left(\frac{-s-i\varepsilon}{m_W^2}\right)\ln\left(\frac{-u-i\varepsilon}{m_W^2}\right)\right.$$
$$\left. + \frac{1}{tu}\ln\left(\frac{-t-i\varepsilon}{m_W^2}\right)\ln\left(\frac{-u-i\varepsilon}{m_W^2}\right)\right], \tag{A.1}$$

where $\alpha \approx 1/137$, m_W represents the mass of the W boson and ε is a small positive quantity defining the branch cut prescription. The fermion contribution gives rise to the approximate amplitude

$$\frac{\mathcal{M}^{(f)}_{++++}(s,t,u)}{\alpha^2 Q_f^4} \approx -8 - 8\left(\frac{u-t}{s}\right)\left[\ln\left(\frac{-u-i\varepsilon}{m_f^2}\right) - \ln\left(\frac{-t-i\varepsilon}{m_f^2}\right)\right]$$
$$-4\left(\frac{t^2+u^2}{s^2}\right)\left(\left[\ln\left(\frac{-u-i\varepsilon}{m_f^2}\right) - \ln\left(\frac{-t-i\varepsilon}{m_f^2}\right)\right]^2 + \pi^2\right), \qquad (A.2)$$

where Q_f is the fermion charge in units of the positron charge, and m_f is the mass of the fermion in the loop. The other amplitudes are related to these by

$$\mathcal{M}_{+-+-}(s,t,u) = \mathcal{M}_{+--+}(s,u,t) = \mathcal{M}_{++++}(u,t,s). \qquad (A.3)$$

We now present the expressions for the photon distributions. We define the auxiliary functions

$$C(x) \equiv \frac{1}{1-x} + (1-x) - 4r(1-r) - P_e\, P_l\, r\, z(2r-1)(2-x), \qquad (A.4)$$

where $r = x/[z(1-x)]$, and

$$\sigma_C = \left(\frac{2\pi\alpha^2}{m_e^2 z}\right)\left[\left(1 - \frac{4}{z} - \frac{8}{z^2}\right)\ln(z+1) + \frac{1}{2} + \frac{8}{z} - \frac{1}{2(z+1)^2}\right]$$
$$+P_e\, P_l\left(\frac{2\pi\alpha^2}{m_e^2 z}\right)\left[\left(1+\frac{2}{z}\right)\ln(z+1) - \frac{5}{2} + \frac{1}{z+1} - \frac{1}{2(z+1)^2}\right]. \qquad (A.5)$$

Here z is a variable describing the laser photon energy; varying z affects the value of x_{max}, the maximum value of the fermion beam energy that the backscattered photons can acquire. We set $z = 2(1+\sqrt{2})$ in our analysis, which maximizes x_{max}. In terms of these functions the photon number and helicity distribution functions take the form

$$f(x, P_e, P_l; z) = \left(\frac{2\pi\alpha^2}{m_e^2 z \sigma_C}\right) C(x) \qquad (A.6)$$
$$\xi(x, P_e, P_l; z) = \frac{1}{C(x)}\left\{P_e\left[\frac{x}{1-x} + x(2r-1)^2\right] - P_l\,(2r-1)\left(1 - x + \frac{1}{1-x}\right)\right\}.$$

Bibliography

[1] D. Abbaneo et al. A combination of preliminary electroweak measurements and constraints on the standard model. hep-ex/0112021.

[2] T. Abe et al. Linear collider physics resource book for Snowmass 2001. Resource book for Snowmass 2001, 30 Jun - 21 Jul 2001, Snowmass, Colorado.

[3] E. Accomando, Ignatios Antoniadis, and K. Benakli. Looking for TeV-scale strings and extra-dimensions. *Nucl. Phys.*, B579:3–16, 2000.

[4] K. Agashe, N. G. Deshpande, and G. H. Wu. Universal extra dimensions and $b \to s\gamma$. *Phys. Lett.*, B514:309–314, 2001.

[5] J. A. Aguilar-Saavedra et al. TESLA technical design report part III: Physics at an e^+e^- linear collider. 2001.

[6] Ofer Aharony, Jaume Gomis, and Thomas Mehen. On theories with light-like noncommutativity. *JHEP*, 09:023, 2000.

[7] (Ed.) Altarelli, G., (Ed.) Kleiss, R., and (Ed.) Verzegnassi, C. Z physics at LEP 1. Proceedings, Workshop, Geneva, Switzerland, September 4-5, 1989. Vol. 1: Standard physics. Geneva, Switzerland: CERN (1989) 453 p. CERN Geneva - CERN 89-08 (89,rec.Dec.) 453 p.

[8] Guido Altarelli, R. K. Ellis, and G. Martinelli. Large perturbative corrections to the Drell-Yan process in QCD. *Nucl. Phys.*, B157:461, 1979.

[9] Charalampos Anastasiou, Lance Dixon, and Kirill Melnikov. NLO Higgs boson rapidity distribution at hadron colliders. *Nucl. Phys. Proc. Suppl.*, 116:193–197, 2003.

[10] Charalampos Anastasiou and Kirill Melnikov. Higgs boson production at hadron colliders in NNLO QCD. *Nucl. Phys.*, B646:220–256, 2002.

[11] Charalampos Anastasiou and Kirill Melnikov. Pseudoscalar Higgs boson production at hadron colliders in NNLO QCD. *Phys. Rev.*, D67:037501, 2003.

[12] Ignatios Antoniadis. A possible new dimension at a few TeV. *Phys. Lett.*, B246:377–384, 1990.

[13] Ignatios Antoniadis, Nima Arkani-Hamed, Savas Dimopoulos, and G. R. Dvali. New dimensions at a millimeter to a fermi and superstrings at a TeV. *Phys. Lett.*, B436:257–263, 1998.

[14] T. Appelquist, J. Carazzone, T. Goldman, and Helen R. Quinn. Renormalization and gauge independence in spontaneously broken gauge theories. *Phys. Rev.*, D6:1747–1756, 1973.

[15] Thomas Appelquist, Hsin-Chia Cheng, and Bogdan A. Dobrescu. Bounds on universal extra dimensions. *Phys. Rev.*, D64:035002, 2001.

[16] Thomas Appelquist and Bogdan A. Dobrescu. Universal extra dimensions and the muon magnetic moment. *Phys. Lett.*, B516:85–91, 2001.

[17] Thomas Appelquist, Bogdan A. Dobrescu, Eduardo Ponton, and Ho-Ung Yee. Proton stability in six dimensions. *Phys. Rev. Lett.*, 87:181802, 2001.

[18] Thomas Appelquist, Bogdan A. Dobrescu, Eduardo Ponton, and Ho-Ung Yee. Neutrinos vis-a-vis the six-dimensional Standard Model. *Phys. Rev.*, D65:105019, 2002.

[19] I. Ya. Aref'eva, D. M. Belov, and A. S. Koshelev. Two-loop diagrams in noncommutative $\phi^4(4)$ theory. *Phys. Lett.*, B476:431–436, 2000.

[20] I. Ya. Aref'eva, D. M. Belov, A. S. Koshelev, and O. A. Rytchkov. UV/IR mixing for noncommutative complex scalar field theory. II: Interaction with gauge fields. *Nucl. Phys. Proc. Suppl.*, 102:11–17, 2001.

[21] Nima Arkani-Hamed and Savas Dimopoulos. New origin for approximate symmetries from distant breaking in extra dimensions. *Phys. Rev.*, D65:052003, 2002.

[22] Nima Arkani-Hamed, Savas Dimopoulos, and G. R. Dvali. The hierarchy problem and new dimensions at a millimeter. *Phys. Lett.*, B429:263–272, 1998.

[23] Nima Arkani-Hamed, Savas Dimopoulos, and G. R. Dvali. Phenomenology, astrophysics and cosmology of theories with sub-millimeter dimensions and TeV scale quantum gravity. *Phys. Rev.*, D59:086004, 1999.

[24] Nima Arkani-Hamed, Savas Dimopoulos, G. R. Dvali, and John March-Russell. Neutrino masses from large extra dimensions. *Phys. Rev.*, D65:024032, 2002.

[25] Nima Arkani-Hamed and Martin Schmaltz. Hierarchies without symmetries from extra dimensions. *Phys. Rev.*, D61:033005, 2000.

[26] Adi Armoni. Comments on perturbative dynamics of non-commutative Yang-Mills theory. *Nucl. Phys.*, B593:229–242, 2001.

[27] Paolo Aschieri, Branislav Jurco, Peter Schupp, and Julius Wess. Non-commutative GUTs, standard model and C, P, T. *Nucl. Phys.*, B651:45–70, 2003.

[28] B. Badelek et al. TESLA technical design report, part VI, Chapter 1: Photon collider at TESLA. 2001.

[29] Riccardo Barbieri, Lawrence J. Hall, and Yasunori Nomura. A constrained Standard Model from a compact extra dimension. *Phys. Rev.*, D63:105007, 2001.

[30] Dmitri Yu. Bardin et al. Zfitter v.6.21: A semi-analytical program for fermion pair production in e^+e^- annihilation. *Comput. Phys. Commun.*, 133:229–395, 2001.

[31] U. Baur. Measuring the W boson mass at hadron colliders. hep-ph/0304266.

[32] G. Beall, Myron Bander, and A. Soni. Constraint on the mass scale of a left-right symmetric electroweak theory from the $K(L) - K(S)$ mass difference. *Phys. Rev. Lett.*, 48:848, 1982.

[33] Daniela Bigatti and Leonard Susskind. Magnetic fields, branes and noncommutative geometry. *Phys. Rev.*, D62:066004, 2000.

[34] L. Bonora and M. Salizzoni. Renormalization of noncommutative U(N) gauge theories. *Phys. Lett.*, B504:80–88, 2001.

[35] L. Bonora, M. Schnabl, M. M. Sheikh-Jabbari, and A. Tomasiello. Noncommutative SO(N) and Sp(N) gauge theories. *Nucl. Phys.*, B589:461–474, 2000.

[36] Andrzej J. Buras. Flavor dynamics: CP violation and rare decays. hep-ph/0101336.

[37] Giacomo Cacciapaglia, Marco Cirelli, and Giampaolo Cristadoro. Gluon fusion production of the Higgs boson in a calculable model with one extra dimension. *Phys. Lett.*, B531:105–111, 2002.

[38] Rong-Gen Cai and Nobuyoshi Ohta. Lorentz transformation and light-like noncommutative SYM. *JHEP*, 10:036, 2000.

[39] Xavier Calmet and Michael Wohlgenannt. Effective field theories on non-commutative space-time. hep-ph/0305027.

[40] Bruce A. Campbell and Kirk Kaminsky. Noncommutative field theory and spontaneous symmetry breaking. *Nucl. Phys.*, B581:240–256, 2000.

[41] Marcela Carena, Howard E. Haber, Heather E. Logan, and Stephen Mrenna. Distinguishing a MSSM Higgs boson from the SM Higgs boson at a linear collider. *Phys. Rev.*, D65:055005, 2002.

[42] M. Chaichian, A. Demichev, P. Presnajder, M. M. Sheikh-Jabbari, and A. Tureanu. Aharonov-Bohm effect in noncommutative spaces. *Phys. Lett.*, B527:149–154, 2002.

[43] M. Chaichian, A. Demichev, P. Presnajder, and A. Tureanu. Space-time noncommutativity, discreteness of time and unitarity. *Eur. Phys. J.*, C20:767–772, 2001.

[44] M. Chaichian, P. Presnajder, M. M. Sheikh-Jabbari, and A. Tureanu. Noncommutative Standard Model: Model building. hep-th/0107055.

[45] M. Chaichian, P. Presnajder, M. M. Sheikh-Jabbari, and A. Tureanu. Noncommutative gauge field theories: A no-go theorem. *Phys. Lett.*, B526:132–136, 2002.

[46] M. Chaichian, M. M. Sheikh-Jabbari, and A. Tureanu. Hydrogen atom spectrum and the Lamb shift in noncommutative QED. *Phys. Rev. Lett.*, 86:2716, 2001.

[47] Sanghyeon Chang, Junji Hisano, Hiroaki Nakano, Nobuchika Okada, and Masahiro Yamaguchi. Bulk Standard Model in the Randall-Sundrum background. *Phys. Rev.*, D62:084025, 2000.

[48] Hsin-Chia Cheng, Bogdan A. Dobrescu, and Christopher T. Hill. Gauge coupling unification with extra dimensions and gravitational scale effects. *Nucl. Phys.*, B573:597–616, 2000.

[49] Hsin-Chia Cheng, Konstantin T. Matchev, and Martin Schmaltz. Bosonic supersymmetry? Getting fooled at the LHC. *Phys. Rev.*, D66:056006, 2002.

[50] Hsin-Chia Cheng, Konstantin T. Matchev, and Martin Schmaltz. Radiative corrections to Kaluza-Klein masses. *Phys. Rev.*, D66:036005, 2002.

[51] Iouri Chepelev and Radu Roiban. Renormalization of quantum field theories on noncommutative R^d. I: Scalars. *JHEP*, 05:037, 2000.

[52] K. G. Chetyrkin and F. V. Tkachov. Integration by parts: The algorithm to calculate beta functions in 4 loops. *Nucl. Phys.*, B192:159–204, 1981.

[53] Chong-Sun Chu, Brian R. Greene, and Gary Shiu. Remarks on inflation and noncommutative geometry. *Mod. Phys. Lett.*, A16:2231–2240, 2001.

[54] Sidney R. Coleman and Sheldon L. Glashow. High-energy tests of Lorentz invariance. *Phys. Rev.*, D59:116008, 1999.

[55] Sidney R. Coleman and E. Weinberg. Radiative corrections as the origin of spontaneous symmetry breaking. *Phys. Rev.*, D7:1888–1910, 1973.

[56] J. Collins. *Renormalization.* Cambridge University Press, 1984.

[57] Alain Connes, Michael R. Douglas, and Albert Schwarz. Noncommutative geometry and matrix theory: Compactification on tori. *JHEP*, 02:003, 1998.

[58] Csaba Csaki, Joshua Erlich, and John Terning. The effective Lagrangian in the Randall-Sundrum model and electroweak physics. *Phys. Rev.*, D66:064021, 2002.

[59] Csaba Csaki, Michael Graesser, Lisa Randall, and John Terning. Cosmology of brane models with radion stabilization. *Phys. Rev.*, D62:045015, 2000.

[60] Schuyler Cullen, Maxim Perelstein, and Michael E. Peskin. TeV strings and collider probes of large extra dimensions. *Phys. Rev.*, D62:055012, 2000.

[61] H. Davoudiasl, J. L. Hewett, and T. G. Rizzo. Bulk gauge fields in the Randall-Sundrum model. *Phys. Lett.*, B473:43–49, 2000.

[62] H. Davoudiasl, J. L. Hewett, and T. G. Rizzo. The $(g-2)$ of the muon in localized gravity models. *Phys. Lett.*, B493:135–141, 2000.

[63] H. Davoudiasl, J. L. Hewett, and T. G. Rizzo. Phenomenology of the Randall-Sundrum gauge hierarchy model. *Phys. Rev. Lett.*, 84:2080, 2000.

[64] H. Davoudiasl, J. L. Hewett, and T. G. Rizzo. Experimental probes of localized gravity: On and off the wall. *Phys. Rev.*, D63:075004, 2001.

[65] Hooman Davoudiasl. $\gamma\gamma \to \gamma\gamma$ as a test of weak scale quantum gravity at the NLC. *Phys. Rev.*, D60:084022, 1999.

[66] S. Dawson. Radiative corrections to Higgs boson production. *Nucl. Phys.*, B359:283–300, 1991.

[67] F. del Aguila and J. Santiago. Universality limits on bulk fermions. *Phys. Lett.*, B493:175–181, 2000.

[68] A. Denner. Techniques for calculation of electroweak radiative corrections at the one loop level and results for W physics at LEP-200. *Fortschr. Phys.*, 41:307–420, 1993.

[69] Keith R. Dienes, Emilian Dudas, and Tony Gherghetta. Extra spacetime dimensions and unification. *Phys. Lett.*, B436:55–65, 1998.

[70] Keith R. Dienes, Emilian Dudas, and Tony Gherghetta. Grand unification at intermediate mass scales through extra dimensions. *Nucl. Phys.*, B537:47–108, 1999.

[71] Keith R. Dienes, Emilian Dudas, and Tony Gherghetta. Light neutrinos without heavy mass scales: A higher- dimensional seesaw mechanism. *Nucl. Phys.*, B557:25, 1999.

[72] Keith R. Dienes, Emilian Dudas, and Tony Gherghetta. Invisible axions and large-radius compactifications. *Phys. Rev.*, D62:105023, 2000.

[73] M. Dittmar, F. Pauss, and D. Zurcher. Towards a precise parton luminosity determination at the CERN LHC. *Phys. Rev.*, D56:7284–7290, 1997.

[74] A. Djouadi, V. Driesen, W. Hollik, and A. Kraft. The Higgs photon Z boson coupling revisited. *Eur. Phys. J.*, C1:163–175, 1998.

[75] A. Djouadi, M. Spira, and P. M. Zerwas. Production of Higgs bosons in proton colliders: QCD corrections. *Phys. Lett.*, B264:440–446, 1991.

[76] Michael R. Douglas and Christopher M. Hull. D-branes and the noncommutative torus. *JHEP*, 02:008, 1998.

[77] S. D. Drell and Tung-Mow Yan. Massive lepton pair production in hadron - hadron collisions at high-energies. *Phys. Rev. Lett.*, 25:316–320, 1970.

[78] E. Dudas and J. Mourad. String theory predictions for future accelerators. *Nucl. Phys.*, B575:3–34, 2000.

[79] T. Filk. Divergencies in a field theory on quantum space. *Phys. Lett.*, B376:53–58, 1996.

[80] Tony Gherghetta and Alex Pomarol. Bulk fields and supersymmetry in a slice of AdS. *Nucl. Phys.*, B586:141–162, 2000.

[81] Fabiola Gianotti and Monica Pepe-Altarelli. Precision physics at the LHC. *Nucl. Phys. Proc. Suppl.*, 89:177–189, 2000.

[82] I. F. Ginzburg, G. L. Kotkin, S. L. Panfil, V. G. Serbo, and V. I. Telnov. Colliding γe and $\gamma\gamma$ beams based on the single pass e^+e^- accelerators. 2: Polarization effects. monochromatization improvement. *Nucl. Instr. Meth.*, A219:5–24, 1984.

[83] I. F. Ginzburg, G. L. Kotkin, V. G. Serbo, and V. I. Telnov. Colliding γe and $\gamma\gamma$ beams based on the single pass accelerators (of VLEPP type). *Nucl. Instr. Meth.*, 205:47, 1983.

[84] Gian F. Giudice, Riccardo Rattazzi, and James D. Wells. Quantum gravity and extra dimensions at high-energy colliders. *Nucl. Phys.*, B544:3–38, 1999.

[85] Sheldon L. Glashow and Steven Weinberg. Natural conservation laws for neutral currents. *Phys. Rev.*, D15:1958, 1977.

[86] E. W. N. Glover. Progress in NNLO calculations for scattering processes. *Nucl. Phys. Proc. Suppl.*, 116:3–7, 2003.

[87] Walter D. Goldberger and Mark B. Wise. Modulus stabilization with bulk fields. *Phys. Rev. Lett.*, 83:4922–4925, 1999.

[88] Walter D. Goldberger and Mark B. Wise. Phenomenology of a stabilized modulus. *Phys. Lett.*, B475:275–279, 2000.

[89] Jaume Gomis, Matthew Kleban, Thomas Mehen, Mukund Rangamani, and Stephen H. Shenker. Noncommutative gauge dynamics from the string worldsheet. *JHEP*, 08:011, 2000.

[90] Jaume Gomis and Thomas Mehen. Space-time noncommutative field theories and unitarity. *Nucl. Phys.*, B591:265–276, 2000.

[91] Jaume Gomis, Thomas Mehen, and Mark B. Wise. Quantum field theories with compact noncommutative extra dimensions. *JHEP*, 08:029, 2000.

[92] Rajesh Gopakumar, Juan M. Maldacena, Shiraz Minwalla, and Andrew Strominger. S-duality and noncommutative gauge theory. *JHEP*, 06:036, 2000.

[93] G. J. Gounaris, P. I. Porfyriadis, and F. M. Renard. The $\gamma\gamma \to \gamma\gamma$ process in the Standard and SUSY models at high energies. *Eur. Phys. J.*, C9:673–686, 1999.

[94] G. J. Gounaris, P. I. Porfyriadis, and F. M. Renard. Light by light scattering at high energy: A tool to reveal new particles. *Phys. Lett.*, B452:76–82, 1999.

[95] D. E. Groom et al. Review of particle physics. *Eur. Phys. J.*, C15:1–878, 2000.

[96] Yuval Grossman and Matthias Neubert. Neutrino masses and mixings in non-factorizable geometry. *Phys. Lett.*, B474:361–371, 2000.

[97] Martin W. Grunewald. Electroweak physics. *Nucl. Phys. Proc. Suppl.*, 117:280–297, 2003.

[98] Lawrence J. Hall and Christopher F. Kolda. Electroweak symmetry breaking and large extra dimensions. *Phys. Lett.*, B459:213–223, 1999.

[99] R. Hamberg, W. L. van Neerven, and T. Matsuura. A complete calculation of the order α_s^2 correction to the Drell-Yan K factor. *Nucl. Phys.*, B359:343–405, 1991.

[100] Tao Han, Joseph D. Lykken, and Ren-Jie Zhang. On Kaluza-Klein states from large extra dimensions. *Phys. Rev.*, D59:105006, 1999.

[101] Robert V. Harlander and William B. Kilgore. Next-to-next-to-leading order Higgs production at hadron colliders. *Phys. Rev. Lett.*, 88:201801, 2002.

[102] M. Hayakawa. Perturbative analysis on infrared aspects of noncommutative QED on R^4. *Phys. Lett.*, B478:394–400, 2000.

[103] J. L. Hewett and T. G. Rizzo. Radion mixing effects on the properties of the Standard Model Higgs boson. *eConf*, C010630:P338, 2001.

[104] JoAnne L. Hewett. Indirect collider signals for extra dimensions. *Phys. Rev. Lett.*, 82:4765–4768, 1999.

[105] JoAnne L. Hewett, Frank J. Petriello, and Thomas G. Rizzo. Signals for noncommutative interactions at linear colliders. *Phys. Rev.*, D64:075012, 2001.

[106] JoAnne L. Hewett and Thomas G. Rizzo. Low-energy phenomenology of superstring inspired E(6) models. *Phys. Rept.*, 183:193, 1989.

[107] I. Hinchliffe and N. Kersting. CP violation from noncommutative geometry. *Phys. Rev.*, D64:116007, 2001.

[108] Stephan J. Huber, Chin-Aik Lee, and Qaisar Shafi. Kaluza-Klein excitations of W and Z at the LHC? *Phys. Lett.*, B531:112–118, 2002.

[109] Stephan J. Huber and Qaisar Shafi. Fermion masses, mixings and proton decay in a Randall- Sundrum model. *Phys. Lett.*, B498:256–262, 2001.

[110] Stephan J. Huber and Qaisar Shafi. Higgs mechanism and bulk gauge boson masses in the Randall- Sundrum model. *Phys. Rev.*, D63:045010, 2001.

[111] G. Jikia and A. Tkabladze. Photon-photon scattering at the photon linear collider. *Phys. Lett.*, B323:453–458, 1994.

[112] Ryuichiro Kitano. Lepton flavor violation in the Randall-Sundrum model with bulk neutrinos. *Phys. Lett.*, B481:39–44, 2000.

[113] V. Alan Kostelecky and R. Potting. Expectation values, Lorentz invariance, and CPT in the open bosonic string. *Phys. Lett.*, B381:89–96, 1996.

[114] V. Alan Kostelecky and Robertus Potting. CPT and strings. *Nucl. Phys.*, B359:545–570, 1991.

[115] V. Alan Kostelecky and Stuart Samuel. Gravitational phenomenology in higher dimensional theories and strings. *Phys. Rev.*, D40:1886–1903, 1989.

[116] V. Alan Kostelecky and Stuart Samuel. Phenomenological gravitational constraints on strings and higher dimensional theories. *Phys. Rev. Lett.*, 63:224, 1989.

[117] V. Alan Kostelecky and Stuart Samuel. Spontaneous breaking of Lorentz symmetry in string theory. *Phys. Rev.*, D39:683, 1989.

[118] V. Alan Kostelecky and Stuart Samuel. Photon and graviton masses in string theories. *Phys. Rev. Lett.*, 66:1811–1814, 1991.

[119] Thomas Krajewski and Raimar Wulkenhaar. Perturbative quantum gauge fields on the noncommutative torus. *Int. J. Mod. Phys.*, A15:1011–1030, 2000.

[120] H. L. Lai et al. Global QCD analysis of parton structure of the nucleon: CTEQ5 parton distributions. *Eur. Phys. J.*, C12:375–392, 2000.

[121] Paul Langacker. Precision electroweak data: Phenomenological analysis. *eConf*, C010630:P107, 2001.

[122] Yi Liao. Validity of Goldstone theorem at two loops in noncommutative U(N) linear sigma model. *Nucl. Phys.*, B635:505–524, 2002.

[123] Fedele Lizzi, Gianpiero Mangano, and Gennaro Miele. Another alternative to compactification: Noncommutative geometry and Randall-Sundrum models. *Mod. Phys. Lett.*, A16:1–8, 2001.

[124] Joseph D. Lykken. Weak scale superstrings. *Phys. Rev.*, D54:3693–3697, 1996.

[125] C. Macesanu, C. D. McMullen, and S. Nandi. Collider implications of universal extra dimensions. *Phys. Rev.*, D66:015009, 2002.

[126] A. D. Martin, R. G. Roberts, W. J. Stirling, and R. S. Thorne. NNLO global parton analysis. *Phys. Lett.*, B531:216–224, 2002.

[127] Alan D. Martin, R. G. Roberts, W. James Stirling, and R. S. Thorne. Parton distributions: A new global analysis. *Eur. Phys. J.*, C4:463–496, 1998.

[128] C. P. Martin and D. Sanchez-Ruiz. The one-loop UV divergent structure of U(1) Yang-Mills theory on noncommutative R^4. *Phys. Rev. Lett.*, 83:476–479, 1999.

[129] Manuel Masip and Alex Pomarol. Effects of SM Kaluza-Klein excitations on electroweak observables. *Phys. Rev.*, D60:096005, 1999.

[130] Keizo Matsubara. Restrictions on gauge groups in noncommutative gauge theory. *Phys. Lett.*, B482:417–419, 2000.

[131] Alec Matusis, Leonard Susskind, and Nicolaos Toumbas. The IR/UV connection in the non-commutative gauge theories. *JHEP*, 12:002, 2000.

[132] Anupam Mazumdar and Mohammad M. Sheikh-Jabbari. Noncommutativity in space and primordial magnetic field. *Phys. Rev. Lett.*, 87:011301, 2001.

[133] Andrei Micu and M. M. Sheikh Jabbari. Noncommutative ϕ^4 theory at two loops. *JHEP*, 01:025, 2001.

[134] Shiraz Minwalla, Mark Van Raamsdonk, and Nathan Seiberg. Noncommutative perturbative dynamics. *JHEP*, 02:020, 2000.

[135] Eugene A. Mirabelli, Maxim Perelstein, and Michael E. Peskin. Collider signatures of new large space dimensions. *Phys. Rev. Lett.*, 82:2236–2239, 1999.

[136] Irina Mocioiu, Maxim Pospelov, and Radu Roiban. Low-energy limits on the antisymmetric tensor field background on the brane and on the noncommutative scale. *Phys. Lett.*, B489:390–396, 2000.

[137] J. W. Moffat. Noncommutative quantum gravity. *Phys. Lett.*, B491:345–352, 2000.

[138] Alexander Muck, Apostolos Pilaftsis, and Reinhold Ruckl. Minimal higher-dimensional extensions of the standard model and electroweak observables. *Phys. Rev.*, D65:085037, 2002.

[139] P. Nogueira. Automatic Feynman graph generation. *J. Comput. Phys.*, 105:279–289, 1993.

[140] E. A. Paschos. Diagonal neutral currents. *Phys. Rev.*, D15:1966, 1977.

[141] G. Passarino and M. J. G. Veltman. One loop corrections for e^+e^- annihilation into $\mu^+\mu^-$ in the Weinberg model. *Nucl. Phys.*, B160:151, 1979.

[142] Michael E. Peskin and Tatsu Takeuchi. A new constraint on a strongly interacting Higgs sector. *Phys. Rev. Lett.*, 65:964–967, 1990.

[143] Michael E. Peskin and James D. Wells. How can a heavy Higgs boson be consistent with the precision electroweak measurements? *Phys. Rev.*, D64:093003, 2001.

[144] Frank J. Petriello. The Higgs mechanism in non-commutative gauge theories. *Nucl. Phys.*, B601:169–190, 2001.

[145] Alex Pomarol. Gauge bosons in a five-dimensional theory with localized gravity. *Phys. Lett.*, B486:153–157, 2000.

[146] Lisa Randall and Raman Sundrum. An alternative to compactification. *Phys. Rev. Lett.*, 83:4690–4693, 1999.

[147] Lisa Randall and Raman Sundrum. A large mass hierarchy from a small extra dimension. *Phys. Rev. Lett.*, 83:3370–3373, 1999.

[148] Ihab. F. Riad and M. M. Sheikh-Jabbari. Noncommutative QED and anomalous dipole moments. *JHEP*, 08:045, 2000.

[149] P. J. Rijken and W. L. van Neerven. Order α_s^2 contributions to the Drell-Yan cross- section at fixed target energies. *Phys. Rev.*, D51:44–63, 1995.

[150] Thomas G. Rizzo. More and more indirect signals for extra dimensions at more and more colliders. *Phys. Rev.*, D59:115010, 1999.

[151] Thomas G. Rizzo. Probes of universal extra dimensions at colliders. *Phys. Rev.*, D64:095010, 2001.

[152] Thomas G. Rizzo and James D. Wells. Electroweak precision measurements and collider probes of the standard model with large extra dimensions. *Phys. Rev.*, D61:016007, 2000.

[153] F. Ruiz Ruiz. UV/IR mixing and the Goldstone theorem in noncommutative field theory. *Nucl. Phys.*, B637:143–167, 2002.

[154] S. Sarkar and B. Sathiapalan. Comments on the renormalizability of the broken symmetry phase in noncommutative scalar field theory. *JHEP*, 05:049, 2001.

[155] N. Seiberg, Leonard Susskind, and N. Toumbas. Strings in background electric field, space/time noncommutativity and a new noncritical string theory. *JHEP*, 06:021, 2000.

[156] Nathan Seiberg and Edward Witten. String theory and noncommutative geometry. *JHEP*, 09:032, 1999.

[157] M. M. Sheikh-Jabbari. Open strings in a B-field background as electric dipoles. *Phys. Lett.*, B455:129–134, 1999.

[158] M. M. Sheikh-Jabbari. Renormalizability of the supersymmetric Yang-Mills theories on the noncommutative torus. *JHEP*, 06:015, 1999.

[159] M. M. Sheikh-Jabbari. Discrete symmetries (C,P,T) in noncommutative field theories. *Phys. Rev. Lett.*, 84:5265–5268, 2000.

[160] Takahiro Tanaka and Xavier Montes. Gravity in the brane-world for two-branes model with stabilized modulus. *Nucl. Phys.*, B582:259–276, 2000.

[161] F. V. Tkachov. A theorem on analytical calculability of four loop renormalization group functions. *Phys. Lett.*, B100:65–68, 1981.

[162] R. S. Towell et al. Improved measurement of the $\bar{d}/\bar{u}$ asymmetry in the nucleon sea. *Phys. Rev.*, D64:052002, 2001.

[163] M. J. G. Veltman. Limit on mass differences in the Weinberg model. *Nucl. Phys.*, B123:89, 1977.

[164] J. A. M. Vermaseren. New features of FORM. math-ph/0010025.

[165] J. C. Webb et al. Absolute Drell-Yan dimuon cross sections in 800-GeV/c *pp* and *pd* collisions. hep-ex/0302019.

[166] Edward Witten. Strong coupling expansion of calabi-yau compactification. *Nucl. Phys.*, B471:135–158, 1996.

[167] Dieter Zeppenfeld. Higgs couplings at the LHC. *eConf*, C010630:P123, 2001.